UNIVERSITE D'AIX-MARSEILLE
ECOLE DOCTORALE 353
IUSTI UMR-CNRS 7343

Thèse sera présentée pour obtenir le grade universitaire de docteur

Discipline : Sciences pour l'ingénieur

Spécialité : Énergétique

Jorge Omar CONTRERAS RODRIGUEZ

Numerical Study of Soot Formation/Oxidation Mechanisms and Radiative Heat Transfer in Closed- and Open-Tip Laminar Diffusion Flames

Sera soutenue le 20/11/2015 devant le jury :

Alexis COPPALLE	INSA de Rouen	Rapporteur
Guillaume LEGROS	Université Pierre et Marie Curie	Rapporteur
Pascal BOULET	Université de Lorraine	Examinateur
Denis LEMONNIER	Institut Pprime	Examinateur
Jean-Louis CONSALVI	Aix-Marseille Université	Directeur de thèse

Résumé

Cette thèse s'inscrit dans une collaboration de long terme entre le laboratoire IUSTI UMR CNRS 7343 de l'Université d'Aix-Marseille et le laboratoire EC^2G de l'Universidad Federico Santa Maria située à Valparaiso au Chili. Cette collaboration a pour but de mieux appréhender les phénomènes de production et d'émission de particules de suie. Elle s'inscrit dans les contextes actuels de demande en énergie croissante et les craintes liées aux effets des polluants produits par la combustion sur la santé et les changements climatiques. Il a notamment été démontré que la suie est le second contributeur au changement climatique après le dioxyde de carbone.

Dans le cadre des flammes de diffusion, l'émission de particules de suie dans l'atmosphère est liée aux phénomènes d'extinction de flamme. Deux mécanismes d'extinction existent : le premier est l'extinction cinétique. Il a lieu quand le temps de mélange (ou temps de résidence) devient significativement plus faible que le temps caractéristique des réactions chimiques, conduisant à des faibles nombres de Damkhöler. Le second mode d'extinction est l'extinction radiative. Il existe seulement en présence de perte radiative et a lieu pour des temps de résidence longs. Il est caractérisé par de larges nombres de Damkhöler. L'extinction a lieu lorsque les pertes radiatives sont suffisamment importantes pour réduire significativement les vitesses de réaction. Le lien entre la production de la suie et l'extinction radiative peut être mieux appréhendé en considérant le phénomène de «smoke-point» d'une flamme de bougie. Tant que le débit de combustible est suffisamment faible le combustible est complètement consommé au sommet de la flamme. Si on augmente le débit de combustible, la longueur de la flamme va augmenter conduisant à une augmentation de la production en suie. Cela induit une augmentation des pertes radiatives, dans la mesure où les particules de suie émettent fortement dans l'infrarouge, ce qui contribue à diminuer la température au sommet de la flamme. Lorsque cette température n'est plus suffisante pour oxyder les particules de suie, ces dernières ainsi que d'autres hydrocarbures imbrûlés sont émis par la flamme. On parle alors de « flammes ouvertes ». L'étude des phénomènes d'extinction radiative dans des flammes à gravité terrestre est assez compliquée dans la mesure où les forces de flottabilité accélèrent l'écoulement et réduisent les temps de résidence. Les flammes laminaires de diffusion en microgravité présentent des temps de résidence plus longs ce qui tend à augmenter la production de suie et les pertes radiatives. Elles présentent donc un cadre idéal pour étudier ces phénomènes.

La configuration considérée est une flamme de diffusion laminaire de type couche limite en microgravité. Cette configuration a été largement étudiée expérimentalement par le groupe de

recherche autour de Torero et de l'institut Pprime à Poitiers. De nombreux résultats expérimentaux concernant la géométrie de la flamme et la production de suie sont disponibles. En outre, ces flammes, qui présentent des phénomènes d'extinction radiatives en queue de flamme, n'ont jamais été simulées numériquement avec un modèle numérique incluant des sous-modèles de production de suie et transfert radiatif élaborés.

L'objectif premier de cette thèse est de développer un outil numérique avancé en vue de simuler la production de la suie, le transfert radiatif et les processus d'extinction au sommet des flammes de diffusion laminaires. Un modèle de production de la suie exhaustif basé sur les PAH est considéré. L'extinction en queue de flamme a lieu lorsque les réactions chimiques deviennent « gelées » laissant place à un mélange non-réactif entre l'oxygène et le combustible. Une description de cette situation nécessite un couplage direct entre l'écoulement et la chimie. Ce modèle sera appliqué pour fournir une meilleure compréhension des mécanismes de production de la suie et des phénomènes d'extinction radiative dans les flammes de diffusion laminaires de type couche limite en microgravité. Il sera également appliqué au problème de production de la suie en oxy-combustion. Pour ce faire, les expériences effectuées à l'Université Federico Santa Maria (Chili) et mettant en jeu des flammes axisymétriques de diffusion laminaires brûlant dans des conditions sous- et suroxygénées seront simulées.

Le premier chapitre de la thèse présente le contexte, les phénomènes physiques mis en jeu, ainsi qu'une revue bibliographique sur les modèles de production de la suie, sur les modèles de propriétés radiatives des gaz, sur les résultats obtenus par le groupe autour de Torero dans le cadre des flammes de diffusion laminaires de type couche limite en microgravité et sur les principaux travaux réalisés dans le cadre de la production de la suie en condition d'oxy-combustion.

Le second chapitre décrit la modèle numérique mis en place. Il est basé sur une formulation à bas nombre de Mach des équations de Navier-Stokes. Il nécessite la résolution des équations de transport pour les espèces chimiques, l'énergie, la fraction massique et le nombre densité de la suie. Des mécanismes cinétiques complets capable de prédire la production des PAH jusqu'au pyrène (A_4) ont été utilisés. Un modèle de production de la suie basé sur les PAH et prenant en compte la nucléation à travers la collision de deux molécules de pyrène, la croissance de surface à travers le processus d'abstraction de l'hydrogène et d'ajout d'acétylène (HACA), la croissance de surface à travers la condensation des PAH, l'oxydation par les radicaux OH et l'oxygène et la coagulation ont été implémentés. Les phénomènes d'extinction en queue de flamme représentent une situation où un couplage direct entre l'écoulement et la chimie doit être considéré. Les équations de transport des

espèces sont fortement couplées à travers les termes de production/destruction des espèces chimiques et doivent ainsi être résolue en bloc à chaque volume de contrôle pour assurer le processus de convergence. Cela nécessite des ressources informatiques significatives ce qui limite l'utilisation du modèle à des configurations bidimensionnelles. Le modèle radiatif est basé sur un modèle de type k-corrélé à larges bandes et sur la méthode des ordonnées discrètes.

Dans le troisième chapitre le modèle numérique est appliqué pour simuler des flammes de diffusion laminaires axisymétriques brûlant dans des conditions sous- et suroxygénées. Les données expérimentales ont été prises de travaux développés à l'Université Federico Santa Maria à Valparaiso (Chili). Les prédictions du modèle sont en bon accord avec les expériences et les principaux effets de l'indice d'oxygène sur la production de suie sont bien capturés.

Le quatrième chapitre traite des flammes de diffusion de type couche limite en microgravité. Une première partie de cette section est destinée à l'analyse des données expérimentales obtenues durant la thèse d'Andrés Fuentes à l'ENSMA à Poitiers (France). Cette analyse est focalisée sur l'influence de la vitesse de combustible, de la vitesse de l'oxydant, et de l'indice d'oxygène, définie comme la fraction molaire d'oxygène dans l'oxydant, sur la 'stand-off distance', la longueur de flamme et la production de la suie. L'analyse de la 'stand-off distance' a révélé que la flamme peut divisée en trois partie : une région dominée par l'inertie ou la stand-of distance croit avec x, une région dominée par la convection ou la stand-off distance croit avec $x^{1/2}$ et une région située après le brûleur ou les effets 3D apparaissent. It a été démontré que ces flammes se comportent différemment par rapport à des flammes de diffusion 'fermées' pour lesquelles le combustible est complètement consommé en queue de flamme. En particulier, la longueur de flamme augmente avec la vitesse d'oxydant, la tendance inverse étant attendue dans le cas de flammes 'fermées'. Ce comportement a lieu parce que la longueur de flamme est contrôlée par l'extinction radiative de la flamme en queue de flamme. Dans ces conditions, la longueur de flamme n'est plus une quantité pertinente pour définir le temps de résidence pour les processus de formation de la suie. Le temps de résidence pour la formation de la suie a été redéfini en considérant la distance entre le brûleur et la position du pic de fraction volumique de suie. Cela a permis d'interpréter les effets de l'indice d'oxygène sur le temps caractéristique de formation de la suie. Des simulations numériques ont été effectuées dans le cas d'un indice d'oxygène de 21% et pour trois vitesses de fuel et deux vitesses d'oxydant. Les résultats numériques présentent un accord raisonnable avec les données expérimentales en termes de stand-off distances et de production de la suie. Les résultats numériques ont été utilisés en premier lieu pour compléter les données expérimentales. En particulier, une meilleure compréhension de la structure de flamme a été fournie :

les radicaux H et OH, responsables de la déshydrogénation des sites dans le processus HACA, et le pyrène, à l'origine de la nucléation des particules de suie et du processus de condensation des PAH, sont localisés dans une région mince qui suit la stand-off distance dans la partie riche en combustible de flamme. Les particules de suie sont produites et croissent dans cette région et sont transportées dans la région de couche limite par les lignes de courant. De plus, les résultats numériques ont confirmé que ces flammes appartiennent à la catégorie des flammes ouvertes et que les pertes radiatives sont responsables de l'extinction de flamme observée en queue de flamme. Elles sont caractérisées par des fractions rayonnées significativement plus élevées que celles observées dans les flammes de diffusion axisymétriques à gravité normale du fait de temps de résidence plus longs. Finalement, la capacité de modèles radiatifs approchés tels que l'approximation de milieu optiquement mince ou des modèles basés sur l'hypothèse de milieux gris a été évaluée. Il a été démontré qu'aucune de ces approximations n'est capable de prédire précisément la structure de flamme, la production en suie et le phénomène d'extinction de flamme en queue de flamme.

Le cinquième chapitre reprend les conclusions de ce travail de thèse et présentent quelques perspectives. De manière générale, cette thèse a permis de mettre au point un modèle numérique capable de prédire la production de suie et les phénomènes d'extinction. Les perspectives à ce travail sont diverses. Il apparait que notamment un effort doit être effectué pour réduire le temps des simulations. La prise en compte d'une distribution en taille pour les particules de suie est également un point intéressant pour améliorer les capacités prédictives du modèle.

Mots-clés : analyse non-dimensionnel, flammes de diffusion de type couche limite, production de suie, indice d'oxygène, microgravité, apesanteur, radiation.

Abstract

This thesis has been developed under long-term collaboration work between the IUSTI UMR CNRS 7343 laboratory of Aix-Marseille University and the EC^2G of UTFSM University of Valparaiso, Chile. The objective of this collaboration is to provide a better understanding of the soot production mechanisms. It is important in today context where energy demand and the effects on human health and global warming of pollutants production from combustion processes increase. Soot has been identified as the second larger contributor to the global warming after CO_2.

In the context of diffusion flames, soot emission is linked to flame quenching phenomena. Two quenching mechanisms exist: first is kinetic extinction. This mode of extinction occurs at low Damköhler numbers, which can be induced by high strain rates, high scalar dissipation rates, low reactant concentrations or low mass flow rates for which the residence times are low. Here the residence time is considered as the time allowed for the flow to pass through the reaction region, which is inversely proportional to the flow velocity in the reaction region. The second extinction mechanism is radiative extinction and only exists in the presence of radiative heat loss, and occurs at long residence times (large Da). While the increase of Da enhances reaction, the energy loss through radiation causes a decrease in flame temperature and renders a reduction of the reaction rate. Extinction takes place when excess heat loss significantly lowers the reaction rate such that the flame can no longer sustain itself. Relation between soot production and radiative extinction can be better understood by considering the "smoke point" phenomena of a candle flame. As fuel flow rate increases, flame length increases then soot production also increases. Higher concentrations of soot increases radiative heat loss since soot is emit strongly heat by radiation. It will decrease the flame temperature at the flame tip. When this temperature at flame tip decreases below the temperature at which soot and other hydrocarbons are oxidized, these escape from flame as pollutants. We call this an *open-tip* flame. The study of radiative extinction phenomena at normal gravity is complicated because the presence of buoyant forces that accelerates the flow by decreasing the residence time. Laminar diffusion flames under microgravity have longer residence times that tend to produce more soot and radiative loss. Thus, these flames are ideal to study radiative extinction.

The configuration considered in present study is a laminar boundary layer diffusion flame under microgravity. This configuration has been largely studied by groups around Jose Luis Torero and Pprime in Poitiers. Several experimental results regarding flame geometry and soot production are

available. But these flames that are characterized by radiative extinction phenomena at the flame tip, have not been numerically simulated by using an advanced soot production and radiation models.

The first objective of this thesis is to develop an advanced numerical tool to predict soot production, radiative heat transfer and radiative extinction at the flame tip. A soot production model based on PAH is used. Radiative quenching takes place when the excess of radiative heat loss significantly lowers the reaction rate such that the flame can no longer sustain itself. A description of this situation needs a coupling between flow and chemistry. This model will be use to provide a better understanding of soot production mechanisms and radiative quenching in laminar boundary layer diffusion flames under microgravity. Also, it will be applied to soot production problem in oxy-combustion processes. To do that, experiments carried out in Universidad Tecnica Federico Santa Maria where axisymmetric laminar diffusion flames under and over-oxygenated will be simulated.

The first chapter oh present manuscript presents the context of the study, physical phenomena involved and a bibliographic review of soot production models, radiative gases properties, results obtained previously regarding laminar boundary layer diffusion flames under microgravity and about the main works about soot production in oxy-combustion processes.

The second chapter describes the numerical model developed. It includes the solution of the overall continuity equation, the Navier–Stokes equations in a low Mach number formulation, and transport equations for gas-phase species mass fraction, the soot mass fraction, the soot number density per unit mass of mixture, and energy. The kinetics mechanisms to predict the PAH production until Pyrene (A_4) were used. A soot production model based on PAH that includes soot nucleation by collision of two Pyrene molecules, surface growth through HACA mechanism and PAH surface condensation, soot oxidation by OH* and O_2 and, finally coagulation have been implemented. The species transport equations are coupled through production/destruction terms of chemical species and need to be solved in a fully coupled fashion at each control volume using a direct solver to ensure the convergence process. This process is very time consuming and restrict the utilization of model to two dimensional configurations. The radiative source term in the transport equation of energy was computed by the discrete ordinate method coupled to a statistical narrow-band-correlated k (SNBCk)-based wide-band model for properties of CO, CO_2, and H_2O.

In the third chapter the numerical model is applied to simulate under and over-oxygenated laminar coflow ethylene diffusion flames. The experimental data was taken from work carried out in

UTFSM. Model results are on the whole in satisfactory agreement with the experimental data for flame structures, radial profiles of soot volume fraction, and the integrated soot volume fractions.

The fourth chapter is devoted to laminar boundary layer diffusion flames under microgravity. The objective of this chapter is to provide a better understanding of soot production and flame quenching at the trailing edge in these flames. In order to accomplish this task, the experiments performed by Fuentes during his PhD thesis (Fuentes 2006) will be analyzed on the basis of a dimensionless analysis. In a second part, the numerical model will be applied to complete the discussion. Finally the effects of the use of simplified radiation models on both soot production and flame structure will be investigated.

The final chapter takes the conclusions of this work again and presents some perspectives. In general, this thesis has allowed refining a numerical model able to predict soot production and radiative extinction phenomena. The perspectives of this work are diverse. It seems that an improvement in computing time needs to be done. No information about the soot aggregates of primary particles is available so methods could be implemented to improve this point.

Keywords : Dimensionless analysis, boundary layer diffusion flame, soot production, oxygen index, microgravity, radiation.

Contents

List of Figures XI
List of Tables XIV
Nomeclature XV
1. Introduction 1
1.1. Context and objectives of this study 1
1.2. Literature survey 4
1.2.1. Soot production processes 4
1.2.2. Radiative heat transfer 8
1.2.2.1. Line-by-line method 8
1.2.2.2. Narrow-Band (NB) models 10
1.2.2.2.1. The statistical NB model 10
1.2.2.2.2. The NB correlated-K (CK) model 11
1.2.2.2.2.1. NB k-distribution concept 11
1.2.2.2.2.2. SNBCK model 12
1.2.2.2.2.3. Global models 13
1.2.3. Laminar boundary layer diffusion flame in microgravity. 15
1.2.4. Effects of oxygen index on soot production. 16
1.3. Overview of the manuscript 18
2. Numerical Models 20
2.1. Flame model 20
2.1.1. Model set-up 20
2.1.2. Gas phase governing equations 21
2.1.3. Radiative transport. 24
2.1.3.1. Spectral radiative transfer equation (RTE) 24
2.1.3.2. Soot radiative properties 25
2.1.3.3. Gas-phase radiative properties 25
2.1.3.4. Discrete Ordinate Method (DOM) 27
2.1.3.5. Optically Thick Approximation (OTA) 27
2.2. Soot model 28
2.2.1. Gas-phase reaction mechanism 28

2.2.2. Soot particle dynamic 29
2.2.3. Soot processes 30
2.2.3.1. Nucleation model 30
2.2.3.2. Surface growth and oxidation 31
2.2.3.3. PAH-surface condensation 33
2.2.4. Agglomeration 34
2.3. Boundary Conditions 34
2.4. Numerical Method 34
Oxygen Index Effect on Axysymmetric Diffusion Flames 36
3.1. Experiments 36
3.2. Computational details 37
3.2.1. Chemical mechanism 37
3.3. Results and Discussion 38
3.3.1. Flame Structure and comparison with experimental data 38
3.3.2. Controlling mechanisms 42
3.4. Conclusions 46
4. Applications to Laminar Boundary Layer Diffusion Flames 47
4.1. Experimental Data Analysis 47
4.1.1. Experimental Set-Up 47
4.1.1.1. Configuration 47
4.1.1.2. Parameters 48
4.1.1.3. Diagnostics 49
4.1.2. Theoretical Analysis 50
4.1.2.1. Dimensionless Variables 51
4.1.2.2. Dimensionless Terms 54
4.1.2.3. Scaling analysis 55
4.1.3. Results 58
4.1.3.1. Stand-off distance 58
4.1.3.2. Flame length 61
4.1.3.3. Soot production 63
4.1.4. Conclusions remarks 66
4.2. Numerical Analysis 67

4.2.1. Chemical mechanism 67
4.2.2. Computational details 67
4.2.3. Comparison with available data 68
4.2.3.1. Stand-off distance (SOD) 68
4.2.3.2. Soot production 70
4.2.4. Flame structure 73
4.2.5. Further discussion 76
4.2.6. Radiative heat transfer 79
4.2.6.1. Radiative structure 80
4.2.6.2. Effects of approximate radiation models 81
4.2.6.2.1. Radiant fractions 81
4.2.6.2.2. Flame geometry 81
4.2.6.2.3. Temperature 83
4.3. Concluding remarks 86
5. Conclusions and perspectives 88
Appendix A 92
Discretization and solution of Radiative Heat Transfer Equation 92
Appendix B 102
Soot model development 102
B.1 Initial PAH formation. 102
B.2 Planar growth and coagulation 103
B.3 Spherical particle formation 104
Collision between molecules 106
B.4 Surface growth and oxidation 109
B.5 PAH-surface condensation 112
B.6 Particle coagulation 113

List of Figures

Figure 1-1: The smoke point concept, taken from (De Ris 2000). 2
Figure 1-2: Characteristic times for the chemical and physical processes (Maas 1992) 6
Figure 1-3: Soot formation/oxidation processes. 8
Figure 2-1: Schematic of a) laminar co-flow diffusion flame and b) laminar boundary layer diffusion flames. 21
Figure 3-1: Domain and boundary conditions. 38
Figure 3-2: Measured and numerical flame heights as a function of ζ. Squares correspond to experimental results for a fuel flow rate of 2.35 cm^3/s. Triangles correspond to numerical results. 39
Figure 3-3: Radial profiles of soot volume fraction for three OIs: (a) 21%, (b) 25% and (c) 29%. (d) The maximum soot volume fraction as a function of the OI. 41
Figure 3-4: a) Distribution of the integrated soot volume fraction as a function of the height normalized by ζ, b) The maximum integrated soot volume fraction as a function of the OI. 42
Figure 3-5: Predicted distributions of: a) nucleation rates, b) surface growth rate, c) temperature, d) molar concentration of pyrene, e) molar concentration of acetylene, and f) molar concentration of hydrogen radical for OIs of 17% and 25%. 44
Figure 3-6: Predicted distributions of: a) soot oxidation rates by OH, b) soot oxidation rate by O2, c) molar concentration of OH, d) temperature, e) soot volume fraction and f) molar concentration of O_2. 45
Figure 4-1: a) Schematic of experimental apparatus (Fuentes 2007); b) Greyscale side view of the visible flame for V_{ox}=150 mm/s and V_F=3 mm/s (Legros 2005). 48
Figure 4-2: Definition of the characteristic quantities. 51
Figure 4-3: Shows the effects of U_{ox} and V_F on stand-off distance for the three oxygen index studied a) 21, b) 35 and c) 50%. 59
Figure 4-4: Evolution of the stand-off distance as a function of the distance along the plate for three different couples of oxidizer and fuel velocities of 300 mm/s and 3mm/s (red symbols), 200 mm/s and 4 mm/s (green symbols) and 125 mm/s and 5 mm/s (blue symbols), leading to ratios between U_{ox} and V_F of 100, 50, and 25, respectively. 60
Figure 4-5: Parameter ($\delta/V_F^{0.4}$) as a function of $(\rho_\infty x/\mu_\infty U_{OX})$ for a) OI=21%, b) OI=35%, and c) OI=50%. 61

Figure 4-6: Effects of oxidizer velocity, fuel velocity and oxygen index on flame length. Symbol nomenclature is displayed as: (□) for V_F=5, (Δ) for V_F=4 and (○) for V_F=3 mm/s. Red, black and blue symbols are used for OI 50, 35 and 21, respectively. 62
Figure 4-7: Represents the effects on maximum soot volume fraction of a) oxidizer velocity (U_{ox}) for V_F=5 mm/s and OI 50%, b) Fuel injection velocity (V_F)for a U_{ox}= 250 mm/s and OI=21%, and c) oxidizer index (OI) for a V_F=5 mm/s and U_{ox}=300 mm/s. d) Residence time as a function of the oxidizer velocity for different fuel velocities and oxidizer velocities. 64
Figure 4-8: Peak of soot volume fraction as a function of the residence time. Red, black and blue symbols are used for OI 50, 35 and 21, respectively. 65
Figure 4-9: Numerical domain and boundary conditions. 68
Figure 4-10: Evolution of the stand of distance as a function of the distance along the plate. a) influence of the U_{ox} for a given V_F of 5 mm/s, b) influence of the V_F for a given U_{ox} of 250 m 69
Figure 4-11: Vertical profiles of soot volume fraction at different longitudinal locations for a) V_F=3 mm/s and U_{ox}=250 mm/s, b) V_F=4mm/s and U_{ox}=250 mm/s, c) V_F=5mm/s and U_{ox}=250 mm/s, d) V_F=5 mm/s and U_{ox}=300 mm/s. 71
Figure 4-12: Integrated soot volume fraction, a) effect of the oxidiser velocity for a given fuel injection velocity of 5 mm/s, and b) effect of the fuel injection velocity for a given oxidizer velocity of 250 mm/s. 72
Figure 4-13: Interaction between reaction zone, soot formation and soot concentration for VF=3 mm/s. Iso-contours for: a) numerical results, and b) experimental results. 73
Figure 4-14: a) Soot production interaction for V_F=3 mm/s, b) soot production precursor species interaction for V_F=3 mm/s, and c) integrated soot formation rate as a function of x-coordinate for V_F=3 mm/s and V_F=4 mm/s. 75
Figure 4-15: Effects of oxidizer velocity and fuel velocity on flame length 78
Figure 4-16: Divergence of radiative flux for V_F=3 mm/s and U_{OX}=250 mm/s 80
Figure 4-17: Flame shape for different radiation models. 82
Figure 4-18: Distributions of the reference temperature distribution and temperature error predicted using approximate radiation models, (a) temperature distribution of the reference model, (b) error of the Gray soot, (c) error of the Planck mean, and (d) error of OTA. 84
Figure 4-19: Distributions of the reference soot volume fraction the relative error of soot volume fraction, (a) soot volume fraction distribution of reference model, (b) Gray soot, (c) Planck mean and, (d) OTA. 85

Figure A-1: Schematic of rectangular geometry a) coordinates and boundary properties, and b) definition of the control volume for discretization of the RTE..... 92
Figure B-1: H-abstraction-C2H2-addition reaction pathway of PAH growth (Frenklach 1994) 103

List of Tables

Table 1-1 : Literature survey on the works developed in Poitiers concerning microgravity LBL diffusion flames..... 15

Table 2-1: Summary of the transport equations solved in simulations..... 22

Table 2-2: HACA-based soot surface growth and oxidation reactions and reaction rate parameters for $k = AT^n e^{(-E/RT)}$. $C_{soot} - H$ represents an active site on the soot particle surface and $C^{\bullet}_{soot}$ is the corresponding radical..... 32

Table 2-3 : Boundary conditions..... 34

Table 3-1: Experimental conditions: the second, third and fourth columns represent respectively the fuel flow rate, the oxidizer flow rate and the flame residence time computed as $\tau = \int_0^{h_f} dz / u_z \left(r = 0, z\right)$..... 37

Table 4-1 : Some characteristics of the flames: oxidizer velocity, fuel velocity, flame length, residence time, Heat Release Rate (HRR), heat released by chemical reactions, combustion efficiency, heat released due to radiative loss, radiant fraction, characteristic time for radiant cooling..... 79

Table 4-2 : Fraction of the HRR radiated away from the flame χ_R with a fuel velocity of 3 mm/s and an oxidizer velocity of 250 mm/s..... 81

Table A-1 : The T_3 quadrature set in the Cartesian geometry. 96

Table A-2 : The T3 quadrature set in the axisymmetric cylindrical geometry (M = 12)..... 98

Table B-1 : HACA-based soot surface growth and oxidation reactions and reactions parameters *for* $k = AT^n \exp(-E/RT)$. $\left(C_{soot} - H\right)$ represents an active site on the soot particle surface and $C^{\bullet}_{soot}$ the corresponding radical..... 110

Nomeclature

A	Pre-exponential factor
A_S	Soot surface area per unit volume of the gaseous mixture
B_R	Pre-exponential factor for radiation
C	Soot absorption coefficient constant
C_A	Agglomeration rate constant
C_S	Mole concentration of soot particle
c_p	Specific heat of the mixture under constant pressure.
$c_{p,k}$	k^{th} species specific heat capacity under constant pressure
d_{A_4}	Collision diameter of the Pyrene nucleation
Da	Damkhöler number
D_∞	Diffusion coefficient at ambient temperature
D_k^T	Thermal diffusion coefficient
D_{jk}	Binary diffusion coefficients
E_{r,f_s}	Relative error for the soot volume fraction
F_i	Line shape profile
F_v	Integrated soot volume fraction
f_s	Soot volume fraction
g	Gravity force
g_k	Quadrature points
h	Planck constant
h_f	Flame height
h_k	k^{th} species specific enthalpy
I	Intensity of radiation
I_b	Planck function
k_B	Boltzmann constant

L_b	Burner length
L_f	Flame length
L_S	Soot formation characteristic length
m_c	Mass of carbon atom
$\dot{m}'_F$	Mass fuel rate
M_c	Molar mass of soot (12.0 g/mol).
N_{av}	Avogadro number (6.022×10^{23} particles/mole)
N_S	Soot molecules number
N_{c,A_4}	Number of carbon atoms in Pyrene molecule (A_4)
p	Pressure
q_r	Divergence of the radiative heat flux
$\dot{q}''$	Radiative flux
$\dot{Q}_{chem}$	Heat released by the chemical reactions
$\dot{Q}_{rad}$	Total radiative heat loss
R_0	Soot particle nucleation rate
R_1	Soot mass nucleation rate
R_2	Soot mass surface growth rate
R_c	Soot mass surface condensation rate
R_{O_2}	Soot mass oxidation by O_2 rate
R_{OH}	Soot mass oxidation by OH rate
R_{agg}	Soot particle agglomeration rate
S	Molar oxidizer to fuel ratio
S_i	Line intensity of the i^{th} line
S_m	Soot mass source term
S_N	Soot number density source term
T_∞	Oxidizer and/or ambient temperature
T_{ad}	Adiabatic temperature

T_f	Characteristic flame temperature
$T_{f,q}$	Temperature at the flame quenching
t_{res}	Residence time
$t_{res,S}$	Residence time for soot formation
t_{rad}	Characteristic time scale of radiative loss
U_{ox}	Oxidizer velocity
u	Axial and/or horizontal velocity
v	Radial and/or vertical velocity
V_F	Fuel velocity
V_k	Diffusion velocity
V_{ok}	Ordinary diffusion velocity
V_T	Thermophoretic soot particle velocity
V_{Tk}	Thermal diffusion velocity
V_{ck}	Correction diffusion velocity
W_k	molecular weight of k^{th} species
w_k	Corresponding weights
Y_k	The k^{th} species mass fraction
Y_S	Soot mass fraction
Y_F	Fuel mass fraction
Y_{ox}	Oxidizer mass fraction
X	Mole fraction

Subscripts

x	Radial and/or vertical coordinate
z	Vertical and/or axial coordinate
i	Properity assigned to i^{th} direction
k	Properity assigned to k^{th} species

Greek Symbols

α	Fraction of the reactive soot surface (steric factor)
γ_{cond}	Pyrene-soot surface condensation efficiency
γ_{OH}	Soot-OH reaction probability
δ_f	Stand-off distance at flame tip
ε	Emissivity
η	Wavenumber
κ_η	Spectral absorption coefficient
$\kappa_{S,\eta}$	Spectral absorption coefficient of soot
λ	Thermal conductivity
μ	Dynamic viscosity
μ_∞	Dynamic viscosity of oxidizer
ν	Kinematic viscosity
ρ	Density of mixture (soot and gas)
ρ_F	Fuel density
ρ_∞	Oxidizer density
τ	Characteristic residence time
$\tau_{f,S}$	Characteristic time scale for soot formation
χ	Combustion efficiency
χ_R	Radiant fraction
ω	Molar production rate

Acronyms

HRR	Heat release rate
HACA	Hydrogen-Abstraction-Acetylene-Addition
LBLDF	Laminar Boundary Layer Diffusion flames
OI	Oxygen index
OTA	Optically thin approximation
PAH	Polycyclic aromatic hydrocarbon

PMMA	Polymethyl methacrylate
RTE	Radiative transfer equation

The person in front of you right now is the most important person in the world

Acknowledgments

First of all, I would like to thank my supervisor Prof. Jean-Louis Consalvi for providing me this research opportunity, for his valued guidance throughout my research, and for his encouragement when there were dead ends and shortage of motivation. The impulse to pursue this PhD began in Chile when I was working with Prof. Andrés Fuentes at UTFSM. Thanks to Andrés for invite me to work with him and then motivate me to give this important step. This thesis was conducted at the IUSTI laboratory (CNRS UMR 7343) in Marseille, France, thus I want to thanks to Mr. Lounès Tadrist, IUSTI director and all laboratory staff that helped me when I didn't speak french and then during my residency. Finally, CONICYT Chile through its program of "Formacion de Capital Humano Avanzado" is acknowledged for funding this project.

1. Introduction

1.1. Context and objectives of this study

The growing concerns about increasing energy demand and hazardous effects of combustion–related pollutants to human health and climate change have led to increasingly stringent regulations on exhaust emissions from combustion devices. Among these pollutants, soot particles have received considerable attention since they have been found detrimental to human health and were suggested to be the second largest contributor to climate change after carbon dioxide.

The release of soot in the atmosphere, but also that of other undesirable pollutants, carbon dioxide or unburnt hydrocarbons, from diffusion flames is directly related to the flame quenching phenomenon. Extinction of diffusion flames has received tremendous attention in combustion studies both theoretically and experimentally because of its fundamental and practical importance. Its implication includes loss of power in engines, operation determent of industrial furnaces, heating outage in buildings, waste of fuels, generation of pollutants and fire safety. Two mechanisms can lead to flame quenching. The first mechanism of flame quenching, widely studied in the literature is the kinetic extinction (S.H. Chung and Law 1983; Suk Ho Chung and Law 1986; Krishnamurthy, Williams, and Seshadri 1976; Law 1975; Liñán 1974; Sohrab and Williams 1981; T'ien and Foutch 1987). It occurs when the mixing time (or residence time) becomes significantly lower than the characteristic time for the chemical reactions (low Damkhöler number, *Da*). It can be induced by high strain rates, high scalar dissipation rates, low reactant concentrations or low mass flow rates for which the residence times are low. The other mode of quenching, opposite to the kinetic mode, is the radiative quenching. It exists only in the presence of radiative heat loss, and occurs at long residence times (large *Da*). While the increase of *Da* enhances reaction, the energy loss through radiation causes a decrease in flame temperature and renders a reduction of the reaction rate. Extinction takes place when excess heat loss significantly lowers the reaction rate such that the flame can no longer sustain itself (Q. Wang and Chao 2011). This mode of extinction was studied experimentally and theoretically by Santa and coworkers (Santa et al. 2007) in the case of a spherical burner diffusion flame in microgravity. They showed that the peak temperature at extinction is about of 1100 K. In addition

they found that while radiative heat losses can drive transient extinction, this is not only because radiative losses are increasing with time but also because the heat release rate is falling off as the flame expands away from the burner and the reactant supply to the flame decreases.

The relationship between soot production and radiative extinction can be better understood by considering the smoke point phenomena in a candle flame at normal gravity (De Ris, Wu, and Heskestad 2000). Figure 1-1 gives an illustration. The flame on the left side is a "closed-tip" flame, i.e. that all the fuel including soot is consumed at the flame tip due to oxidation. Let us increase progressively the fuel flow rate. The flame length and then the residence time will increase progressively leading to an enhancement in soot production.

This will produce an increase in radiative loss since the soot particles emit strongly thermal radiation. The temperature of the gas at the flame tip will decrease. When this temperature will be not sufficient to oxidize soot, soot and other hydrocarbons will be emitted from the flame. The temperature at which soot ceases to be oxidized is known to be around 1400K (Kent 1986). The point at which the flame just starts to emit soot is called the smoke point ((the smoke point can be seen in the fifth flame from left to right in Figure 1-1). Above this point, an "open tip" flame is observed and the fuel is not fully consumed at the flame tip. Markstein and De Ris (Markstein and De Ris 1985) established that candle flames burning in air at normal gravity, the flame quenches at a fixed radiant fraction (defined as the ratio of the heat release rate radiated away from the flame) of about 30%.

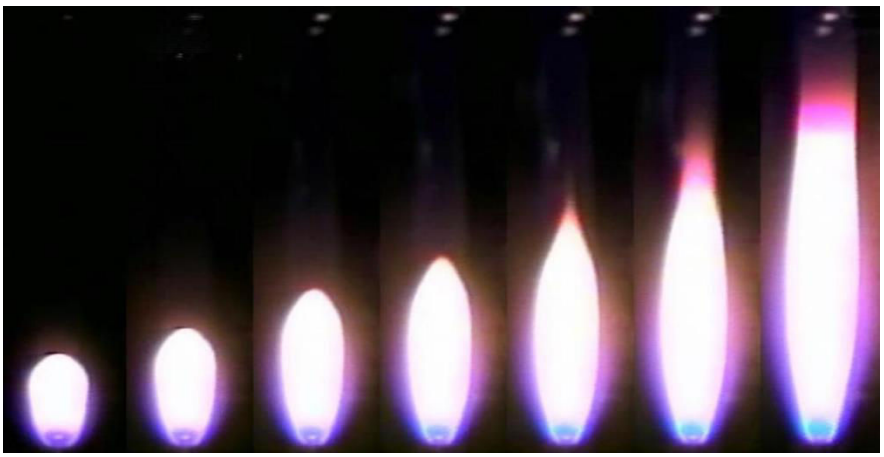

Figure 1-1: The smoke point concept, taken from (Urban et al. 2000).

The existence of radiative extinction was less studied than the kinetic quenching because it is more difficult to observe on earth as the intrusion of buoyancy force accelerates the flow and

reduces the residence time. Microgravity laminar diffusion flames exhibit much longer residence times which enhance the soot production and the radiative loss as compared to laminar flames in the same conditions at normal gravity (Konsur 1999b; Liu 2011; Demarco 2013). They are then good candidate to study theoretically, experimentally and numerically the soot production as well as the radiative quenching processes.

Most of the experimental works performed in microgravity laminar diffusion flames considered an axi-symmetric configuration (Greenberg and Ku 1997; Konsur, Megaridis, and Griffin 1999a; Megaridis, Griffin, and Konsur 1996; Urban et al. 2000).

On the other hand, laminar boundary layer (LBL) diffusion flames at microgravity were extensively studied by the group of researchers around Torero (Fuentes, Legros, Claverie, et al. 2007; Fuentes, Legros, El-Rabii, et al. 2007; Legros and Torero 2015; Legros et al. 2006, 2009; Torero et al. 2002; Vietoris et al. 2000). This geometry occurs when a flame sets over a fuel plate supported by a low oxidizer flow blowing parallel to this plate. The fuel can be solid, like a PMMA plate (Fuentes et al. 2005; Torero et al. 2002; Vietoris et al. 2000), a liquid film or gaseous fuel injected through a flat porous burner (Fuentes, Legros, Claverie, et al. 2007; Legros and Torero 2015; Legros et al. 2006, 2009).

The use of gas burners to simulate the combustion of a solid or a liquid was justified by longer experiments times, no fuel surface regression and because this configuration is easier to control. The oxidizer flow is expected to be laminar, due to low velocities, leading to the formation of a laminar boundary layer diffusion flame (LBLDF). This particular configuration was considered as being one of great relevance to fire safety for spacecraft (Torero 2000), and the classical Emmons formulation of the LBL theory (Emmons 1956) was proposed as a candidate to interpret current material flammability procedures (Torero et al. 2002).

Extensive measurements of flame shape, PAH and soot concentrations in such flames were reported for different fuel and oxidizer velocities and oxygen indexes (defined as the molar fraction of oxygen contained in the oxygen/nitrogen mixture that composes the oxidizer). An analysis of the data suggested that these belong to the category of open-tip flames (Fuentes, Legros, Claverie, et al. 2007), i.e. flame quenching occurs at the trialing edge of these flames owing to radiative loss. They are then good candidate to study soot production and flame

quenching at the flame trailing edge. To the author's best knowledge no numerical study involving advanced soot production and radiation models were reported.

The first objective is to develop an advanced numerical tool in order to simulate soot production, radiative heat transfer and the flame quenching process at the flame tip in laminar diffusion flames. An exhaustive soot production model based on PAH is considered. Flame quenching at the trailing edge depicts a situation where the chemical reactions become frozen and unreactive mixing occurs. A description of this situation requires a direct coupling between the flow and the chemistry and conservation equations for all the gaseous species have to be considered. This model will be applied to provide a better understanding of the soot production mechanisms and radiative flame quenching at the trailing edge in microgravity LBL diffusion flames. It will be also applied to the problem of soot production in oxy-combustion. For this purpose the experiments performed at the University Fédérico Santa Maria in Valparaiso (Chile) and concerning laminar axi-symmetric coflow ethylene flames burning under different oxygen indexes ranging from under-oxygenated to over-oxygeneted conditions will be simulated.

1.2. Literature survey

The previous section has revealed the importance of soot production and radiative heat transfer for the problem of interest in the present work. As a consequence, a significant part of the following literature survey will be devoted to these two points. The Third part will consider the works developed by the group of researchers around Torero concerning the microgravity LBL diffusion flames since this configuration and the experimental data collected during these studies are of particular interest for the present work. Finally, the last part will be devoted to the problem of soot production in oxy-fuel conditions.

1.2.1. Soot production processes

Soot is an agglomerate of particles, which vary in structure and size (Lahaye and Prado 1981). The main constituent of soot is carbon with some minor amounts of hydrogen and oxygen. Depending on the surrounding gas, other species may adsorb onto the surface of soot. Although many properties of soot have been identified, it has not been possible to uniquely define the chemical composition of soot.

The size of the smallest soot particle follows the limits of experimental research. The size of the smallest primary particle is detected with an electron microscope and has a size of 20nm (Liu, Smallwood, and Gülder 2000). Soot is produced during the combustion of hydrocarbons under fuel-rich conditions at high temperatures. The emission of soot from a flame is determined by its formation and oxidation processes.

Two difficulties exist in the modelling of soot concentrations:

1. The first difficulty can be analyzed from Figure 1-2 which shows the characteristic time scales for the different physical and chemical processes. When the chemistry is sufficiently fast, i.e. characteristic times for chemical processes are much faster than those of the flow; the chemical reactions occur in a quasi-steady state and adjust immediately to the flow conditions. In this case, the chemistry and the mixing can be decoupled. This is the basis concept of the "flamelet". We can then generate state relationships for the different reactive scalars, such as the temperature or the species mass fraction, as a function of a reduced number of parameters describing the local flow conditions (mixture fraction, scalar dissipation rate, radiative loss). Figure 1-2 shows that the chemistry associated to soot, and more generally to pollutants, is slow. As a consequence, the simplifications described previously cannot be rigorously applied.

2. The second difficulty comes from the fact that, contrary to NO and other pollutants, the soot acts on the flow through the radiative losses that it produces. As a consequence, the formation of soot cannot be considered a posteriori, i.e. once the flow field has been predicted. This implies that reduced or simplified soot models must be developed in view of applications. It is also required to take into account for radiative heat transfer in an accurate manner, soot formation/oxidation processes being sensitive to temperature. The effects of the coupling between soot formation and radiative heat transfer is important because of, the continuum radiation of soot plays an important part in the radiative loss of flames, affecting the temperature field and consequently the formation/oxidation processes of soot particles themselves. Coupled flow field/combustion/radiative heat transfer calculations are then required, raising the question about the radiative model to be used in order to keep the computational requirement compatible with an exhaustive study. The small dimensions of the

laminar co-flow diffusion flames considered in the present study suggest that the optically thin approximation (OTA) may be used. However, previous studies have shown that this approximation, valid for 'closed-tip' laminar diffusion flames at normal gravity (Liu, Guo, and Smallwood 2004), can be deficient for 'open-tip' flames at both normal and micro-gravity(Liu et al. 2003). As an example the amount of soot released from the flame in the case of smoking flames can be widely affected by the soot model (Liu et al. 2003). As a consequence, before evaluating the soot model a study, involving smoking and non-smoking ethylene flames (Megaridis and Dobbins 1989a, 1989b; Santoro et al. 1987), is carried out to find an adequate radiative model.

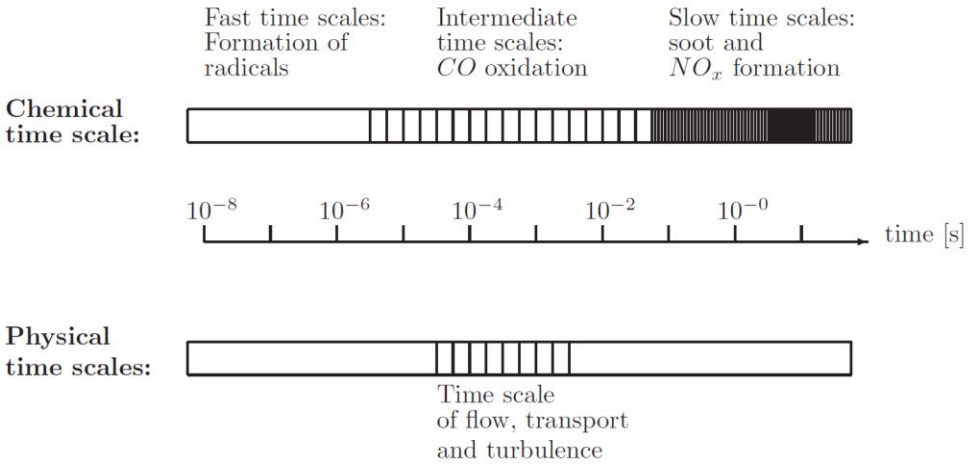

Figure 1-2: Characteristic times for the chemical and physical processes (Maas and Pope 1992)

The more-detailed soot models of today describe the formation of soot in eight steps (Appel, Bockhorn, and Frenklach 2000; Chernov et al. 2012; Dworkin et al. 2011; Slavinskaya and Frank 2009):

1. Gas phase reactions: the first step in soot formation is the formation of benzene (C_6H_6) and phenyl (C_6H_5).
2. Poly-aromatic Hydrocarbons (PAH) grow in two-dimension through the HACA (Hydrogen Abstraction Carbon Addition) mechanism and the condensation of PAH.

3. The nucleation of soot particles: this is the first step where two-dimensional PAH merge into three-dimensional soot particles.
4. Condensation: the particles grow via condensation of a two-dimensional PAH on a three-dimensional PAH.
5. Surface growth: soot particles grow in mass through reactions between the gaseous species and the surface of soot particle. Acetylene (C_2H_2) is the dominant species in this step.
6. Coagulation: two soot particles merge.
7. Agglomeration: large chains of primary particles are formed.
8. Oxidation: the soot particle loses mass in reactions with gas phase molecules O_2 and OH.

As a consequence, detailed soot models require describing the following mechanisms:

1. A gas phase kinetic mechanism sufficiently large to predict the concentrations of the chemical species involved in the soot production mechanism (C_2H_2, C_4H_x, C_3H_3, C_6H_5, C_6H_6, PAH …).
2. A soot kinetic model (interactions between soot particle and surrounding gas) including nucleation, mass growth and oxidation.
3. A dynamic of soot particles (interactions between soot particles). Including coagulation and agglomeration. The dynamic of the soot particles can be treated by three different ways:
    - By using a moment method where the moments of the size distribution of soot particles are solved (Appel, Bockhorn, and Frenklach 2000; Bai et al. 1998; Balthasar and Kraft 2003; Balthasar et al. 1996; Michael Frenklach and Harris 1987).
    - By using a sectional method where the size distribution of soot particles is divided into discrete sections (Q. Zhang et al. 2009).
    - By using stochastic methods (Balthasar and Kraft 2003).

Detailed models were applied to laminar (Balthasar et al. 1996; Dworkin et al. 2011) and turbulent (Bai et al. 1998) flames.

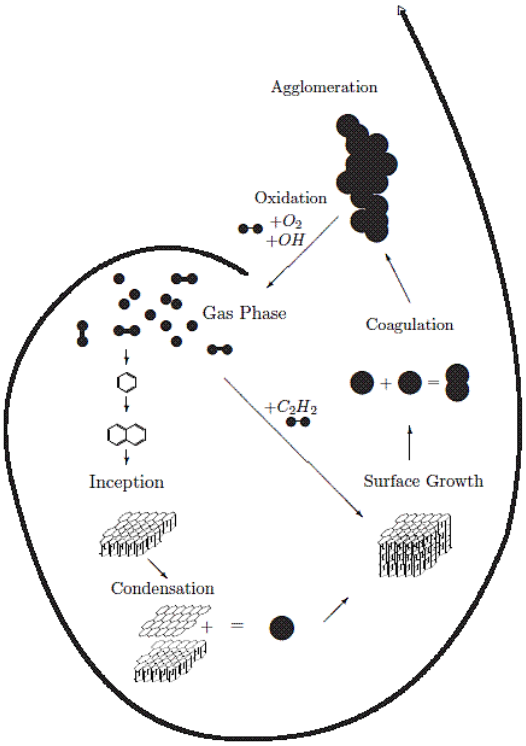

Figure 1-3: Soot formation/oxidation processes.

1.2.2. Radiative heat transfer

An accurate prediction of radiative heat transfer in flames is a difficult task since it requires a precise solution of the radiative transfer equation (RTE) and a proper modelling of the spectral dependence of radiating species (radiative participating gases and soot particles). In particular the determination of accurate solutions for radiative heat transfer is difficult in media involving combustion products due to the strong dependence of the absorption coefficient of gases on the wavenumber. In this part the models to compute the radiative property models of gaseous radiative species are discussed. The models will be decomposed into three categories: the Line-by-Line (LBL) method, the Narrow band (NB) models and the global models.

1.2.2.1. Line-by-line method

The line-by-line method (LBL) can be viewed as an 'exact' method since no assumption is made on the absorption coefficient. It requires about 10^6 resolutions of the Radiative Transfer

Equation (RTE) to consider the strong dependence of the absorption coefficient on the wave number (Modest 2013) involving computation requirements which are too large for practical applications. However it can be used to compute reference solutions to assess approximate radiative property models (Chu, Liu, and Zhou 2011; Consalvi and Liu 2014a, 2014b) or to generate NB databases to be used for NB models (Consalvi and Liu 2014a, 2014b; L. Wang and Modest 2005). A brief description of this model is provided below.

The RTE is integrated with a spectral resolution of the order of 0.01 cm^{-1}. At each wavenumber of the spectral discretization the absorption coefficient is calculated as (Modest 2013; Taine and Soufiani 1999):

$$\kappa_\eta = N \sum_{i=1}^{n_{LINES}} S_i(T) F_i(\eta) \tag{1.1}$$

Where N is the molecule number density of the radiating species, S_i is the line intensity of the i^{th} line and F_i is the line shape profile. For a medium involving a mixture of radiative participating gases, the spectral absorption coefficient for the mixture is computed by adding the absorption coefficient of each gas.

The line intensity is obtained from the following expression (Modest 2013; Taine and Soufiani 1999):

$$S_i(T) = S_i(T_0) \frac{Q_v(T_0) Q_r(T_0)}{Q_v(T) Q_r(T)} \exp\left[\frac{hcE''}{k_B} \left(\frac{1}{T_0} - \frac{1}{T} \right) \right] \frac{1-\exp(-hc\eta_i / k_B T)}{1-\exp(-hc\eta_i / k_B T_0)} \tag{1.2}$$

Where η_i is the wavenumber at the line center. T_0, and Q_v and Q_r are the reference temperature, and the vibrational and rotational partition functions of the absorbing gas, respectively. $S_i(T_0), h,\ c$ and k_B are the line intensity at T_0, the lowest energy state for transition, the Planck constant, the speed of light in the vacuum and the Bolzmann constant, respectively.

At atmospheric pressure the line shape profile can be assumed to follow a Lorentz profile:

$$F_i(\eta) = \frac{\gamma_c}{\pi \left[(\eta - \eta_i)^2 + \gamma_c^2 \right]} \tag{1.3}$$

Where γ_c is the line half-width at half-maximum (HWHM) due to collision or pressure broadening and η_i is the centre wavenumber of the line:

$$\gamma_C = \left(\frac{T_0}{T}\right)^n \left[\gamma_{air}\left(1-x\right)+\gamma_{self}x\right]P \tag{1.4}$$

In equation (1.4), γ_{air}, is the air-broadened half-width, γ_{self} is the self-broadened half-width, and *x* and *m* are the molar concentration and the mass of a molecule of the gas species under consideration, respectively. n is the coefficient of temperature dependence for γ_C.

In the case of gaseous combustion products at relevant temperatures for combustion applications, spectroscopic database such as CDSD 1000 for CO_2 (Tashkun et al. 2003) and HITEMP 2010 (Rothman et al. 2010) for CO_2, H_2O and CO are available. These database contains the line parameters for each line i, i.e. η_i, $S_i(T_0)$, γ_{air}, γ_{self}, E'' and n.

1.2.2.2. Narrow-Band (NB) models

NB models are based on the discretization of the spectrum into small spectral intervals (typically between 5 to 50 cm^{-1}), $\Delta\eta$, over which the Planck function and the radiative properties of particles and walls are essentially constants.

1.2.2.2.1. The statistical NB model

The Malkmus model is recognized as the most suitable statistical NB model for combustion gases. In this model, the line probability distribution is assumed to have the following expression (Modest 2013):

$$P(S) = \frac{1}{S\ln R}\left[\exp\left(-S/S_m\right)-\exp\left(-RS/S_m\right)\right] \tag{1.5}$$

Where S_{max} is the maximum value of the line intensity and *R* is the ratio of the maximum to minimum value of the line intensity. $P(S)$ is the probability density function and thus satisfies $\int_0^\infty P(S)\,dS = 1.$ The NB averaged transmissivity is then expressed as (Modest 2013):

$$\tau_{\Delta\eta}(L)=\frac{1}{\Delta\eta}\int_{\Delta\eta}exp\left(-\kappa_\eta\left(\underline{\phi}\right)L\right)=exp\left[-\frac{\pi B}{2}\left(\sqrt{1+\frac{4SL}{\pi B}}-1\right)\right] \tag{1.6}$$

Where $B=2\bar{\beta}_\nu/\pi$, $S=\bar{\kappa}_\nu \mathrm{X}p$, $\bar{\beta}_\nu=2\pi\bar{\gamma}_\nu/\bar{\delta}_\nu$. The NB databases with a spectral resolution of 25 cm^{-1} were generated from spectroscopic databases by Soufiani and Taine (Soufiani and Taine 1997) for a range of temperature between 300K and 2500K and by Rivière and coworkers for a range of temperatures between 300 K and 4000 K (Rivière and Soufiani 2012), can be used.

The accuracy of the SNB model, which gives the spectral transmissivity over a NB, is well recognized. However, this method suffers from two drawbacks. Firstly it cannot be easily coupled with differential solution methods of the RTE, such as the Discrete Ordinates Method (DOM) (Fiveland 1984), the Finite Volume Method (FVM) (Raithby and Chui 1990) or the P1 (Sazhin et al. 1996), without the introduction of approximations leading to a loss in accuracy (Liu et al. 1998; L. Zhang, Soufiani, and Taine 1988). In order to keep its accuracy the SNB model is generally coupled with the Ray Tracing (RT) method. As the RT method is time consuming, the SNB model is often limited to determining radiative intensity along a line of sight (Kounalakis, Gore, and Faeth 1989a, 1989b; Sivathanu, Gore, and Dolinar 1991) or to providing benchmark solutions when LBL solutions are not available (Coelho, Perez, and El Hafi 2003; Goutiere, Liu, and Charette 2000). Secondly it is not a feasible way to account for scattering unless the Monte Carlo method is used, which increases even more the computational time.

1.2.2.2.2. The NB correlated-K (CK) model

Contrary to the SNBCK model the NBCK method gives the absorption coefficient, so it can be coupled with arbitrary RTE solvers and can account for scattering. This method consists in reordering the absorption coefficient in a NB into a smooth; monotonically increasing function called the k-distribution and is described in this section.

1.2.2.2.2.1. NB k-distribution concept

A detailed explanation of the method can be found in (Modest 2013). The NBCK model introduces two new variables, namely the distribution function $f_{NB}\left(\underline{\varphi},k\right)$ and its cumulative distribution function $g_{NB}\left(\underline{\varphi},k\right)$ given by: $f_{NB}\left(\underline{\varphi},k\right)=\int_{\Delta\eta}\delta\left[k-\kappa_\eta\left(\underline{\varphi}\right)\right]d\eta\Big/\Delta\eta$ and

$g_{NB}\left(\underline{\varphi},k\right)=\int_0^k f\left(\underline{\varphi},k'\right)dk'$, where k is a variable absorption coefficient. The NB RTE and the average NB intensity $\overline{I_\eta}$ are then expressed as:

$$\frac{dI_g}{ds}=k_g^*\left(\underline{\varphi},g_{NB}\right)\left(I_{b\eta}-I_g\right) \tag{1.7}$$

$$\overline{I_\eta}=\frac{1}{\Delta\eta}\int_{\Delta_\eta} I_\eta d\eta=\int_0^1 I_g dg \tag{1.8}$$

Since the function $g_{NB}\left(x\right)$ increases monotonically, integration over the g-space can be performed by using a simple Gauss quadrature scheme with few points.

1.2.2.2.2.2. SNBCK model

The use of the NBCK model requires the knowledge of the k-distribution. k-distributions can be obtained from the SNB model, leading to the SNBCK model. The averaged NB transmissivity, as defined in (1.9), may also be computed from NB k-distribution function or from the cumulative NB k-distribution function as (Modest 2013):

$$\bar{\tau}_{\Delta\eta}=\int_0^\infty f_{NB}\left(k\right)e^{(-kl)}dk=\int_0^1 e^{\left[-k\left(g_{NB}\right)l\right]}dg_{NB} \tag{1.9}$$

Equation (1.9) shows that the NB transmissivity is the Laplace transform of the absorption coefficient probability density function $f_{NB}\left(x\right)$. This latter function can be then deduced from the transmissivity given by the Malkums model by considering an inverse Laplace transform of equation (1.9). The following analytical expression was obtained by Domoto (Domoto 1974):

$$f_{NB}\left(k\right)=\frac{1}{2\pi k}\left(\frac{2\beta_M xp\bar{\kappa}_M}{k}\right)^{1/2}\exp\left[\frac{\beta_M}{2\pi}\left(2-\frac{xp\bar{\kappa}_M}{k}-\frac{k}{xp\bar{\kappa}_M}\right)\right] \tag{1.10}$$

Equation (1.10) can be integrated to give the cumulative density function:

$$g_{NB}\left(k\right)=\frac{1}{2}\left[1-erf\left(\frac{a}{\sqrt{k}}-b\sqrt{k}\right)\right]+\frac{1}{2}\left[1-erf\left(\frac{a}{\sqrt{k}}+b\sqrt{k}\right)\right] \tag{1.11}$$

With $a=\sqrt{\frac{\beta_M xp\overline{\kappa_M}}{2\pi}}$ and $b=\sqrt{\frac{\beta_M}{2\pi xp\overline{\kappa_M}}}$. Although an analytical expression for $k\left(g\right)$ does not exist, it can be found numerically by using a Newton-Raphson iteration method. In general only few iterations are required when $k_{\max}$ (where $f_{NB}\left(x\right)$ peaks) is used as the initial value of k (Domoto 1974).

1.2.2.2.2.3. Global models

Global models are generally limited to problems with grey walls and/or particles. The Weighted-Sum-of-Grey-Gases (WSGG) model, initially developed by Hottel and Sarofim (Hottel and Sarofim 1967), can be applied to any method for solving the RTE (Modest 2013). It consists in replacing the non-grey gas by a number of grey gases, for which the radiative rates are computed independently. The absorption coefficient and the weighting factor of each gray gas can be obtained by fitting data of total emittance. In its original form, the WSGG correlations are obtained for fixed ratios between the molar concentrations of the participating species, which limits its application to homogenous media. In recent studies, the fitting parameters of the WSGG have been derived from spectroscopic databases and by avoiding to considerer fixed ratio of molar concentration between CO_2 and H_2O. Benchmarks have shown that these kinds of WSGG can be promising (Centeno et al. 2015).

The Spectral-Line-Based Weighted-Sum-of-Grey-Gases (SLW) (Denison and Webb 1993a, 1993b, 1995a, 1995b, 1995c, 1995d) and the Full-Spectrum *k*-distribution model (FSK) (Modest and Zhang 2001) can be viewed as improvements of the WSGG. The basic idea of these methods consists in reordering the absorption coefficient over the entire spectrum into a smooth, monotonically increasing function called the full-spectrum (FS) *k*-distribution. The integration over about 10^6 lines is then reduced to the integration of a single smooth function. As shown by

Modest (Modest 2013), SLW and FSK models differ in the methodology employed to perform this integration. The SLW uses a simple trapezoidal scheme, defining N_G grey gases, whereas the FSK uses a quadrature scheme. Solovjov and Webb (Solovjov and Webb 2000a, 2000b) and Modest and Riazzi (Modest and Riazzi 2005) developed models to generate a single FS *k*-distribution for a mixture of gases and soot. Due to the similarities between these two methods, only the Full Spectrum Correlated k (FSCK) method is presented here.

The FSCK extends the NB CK distribution method by reordering the absorption coefficient over the entire spectrum. This task is accomplished by defining a Full Spectrum (FS) Planck-function weighted-*k* distribution $\left(f\left(T,\underline{\varphi},k\right)=\int_0^{\infty} I_{b\eta}\left(T\right)\delta\left[k-\kappa_\eta\right]d\eta \Big/ I_b\left(T\right)\right)$ and a FS Planck-function weighted cumulative *k*-distribution $\left(g\left(T,\underline{\varphi},k\right)=\int_{\grave{a}}^{k} f\left(T,\underline{\varphi},k'\right)dk'\right)$. Due to the smooth nature of the cumulative function, the integration of the reordered wavenumber can be easily achieved with a simple integration scheme. In the case of non-homogeneous and/or non-isothermal media, as for the NBCK model, the assumption that the absorption coefficient is scaled or correlated is applied introducing errors in the methods (Modest 2013). The FSCK leads to a reordered RTE in smoothly-varying g_{ref}-space (Modest 2013):

$$\frac{dI_g}{ds}=k^*\left(T_{ref},\underline{\varphi},g_{ref}\right)\left[a\left(T,T_{ref},g_{ref}\right)I_b\left(T\right)-I_g\right] \quad \text{with} \quad a\left(T,T_{ref},g_{ref}\right)=\frac{dg\left(T,\underline{\varphi}_{ref},k\right)}{dg\left(T_{ref},\underline{\varphi}_{ref},k\right)} \tag{1.12}$$

The spectrally integrated intensity $\left(I\right)$ is evaluated as:

$$I=\int_{\Delta_\eta} I_\eta d\eta=\int_0^1 I_g dg \tag{1.13}$$

Generally a Gauss quadrature scheme with about 10 quadrature points is to obtain accurate solutions (Consalvi and Liu 2014a, 2014b; Demarco et al. 2011). The reference state is usually defined by the molar fractions of the gas species averaged over the flame volume. The reference temperature can be calculated as an emission weighted temperature (Modest and Riazzi 2005).

1.2.3. Laminar boundary layer diffusion flame in microgravity.

The objective of this section is to provide an overview of the works developed by the group of researchers around Torero. These studies as well as the principal findings are summarized in Table 1-1.

Table 1-1 : Literature survey on the works developed in Poitiers concerning microgravity LBL diffusion flames.

Reference	Kinds of study	Focus	Parameters	Methods	Findings
(Vietoris et al. 2000)	**Exp. :** - Opposed flame spread over PMMA slab - Oxygen index 40%	- Visible flame shape - Flow field	U_{ox}= 50, 100, 150 mm/s.	- CCD Lat and top view. - IR cam (4.28µm) for PMMA temperature. - A green-light sheet to follow flow traces.	- Exp results provide evidence of the role of flame radiation, in-depth conduction and surface reradiation in the low velocity extinction process. - The effect of the flame on the flow decreases with U_{ox}
(Torero et al. 2002)	**Exp. and Theoretical:** - Cocurrent flame spread over PMMA slab	- Methodology to extract the B number from a comparison of theoretical predictions and video recordings of the flame stand-off distance	OI= [0.235-0.432] U_{OX}=[63-400] mm/s	- Emmons theory for µg forced flames (Emmons 1956) - Pagni and Shih, Kosdon and Anamalai for natural convection (Pagni and Shih 1977) and (Annmalai and Sibulkin 1979; Kee et al. 1996; Kosdon, Williams, and Buman 1969).	- Flame length increases with V_{ox} - T_F is a "linear" function of B - Da decreases with "x"
(Rouvreau et al. 2002)	**Numerical (FDS):** - Gas burner, (Ethylene) - No radiation model: Radiative loses are set to 40%.	- Understanding the effects of flame on the flow and to validate the use of LBL theory to model the stand off distance. - Quantify the influence of both injection and heat release on the free stream	U_{OX} V_F C_q= V_F/ U_{OX}	- Comparison with Emmons LBL theory, 2D flow.	- Velocity overshoots produced by P grad induced by fuel inject and amplified by flame. - 2 regimes: Vf<0,01m/s, flow conforms BLA. Vf>0,01, separation of flow
(Fuentes et al. 2005)	**Exp.** - Cocurrent. PMMA - OI 35%	- Soot formation in non-buoyant LBLDF - Quantify soot concentrations to carry out radiation calculations	U_{OX}	- Instantaneous grey scale (CCD) is used to determine flame geometry.	- A methodology to estimate the extinction factor at different cross-sections. - Extinction factor can be used to calculate directly f_S
(Brahmi et al. 2005)	**Exp.** - Gas burner **Num.**: - FDS, no Radiation Model, 1step finite rate chemistry.	- Visible flame shape - Influence of V_F, Uox and OI on the flow structure	OI, V_F, U_{OX}	- Particle Image Velocimetry	- Min V_F is necessary to obtain a stable flame. - 3 charac. regimes. - As Cq increases, the thermal expansion is enhanced and 3D effects are more pronounced.
(Legros et al. 2005)	**Exp**. - Gas burner - Ethylene	- 3D Measurements of f_S and CH to produce data to estimate RHT.	U_{OX}, V_F	- CH* chimiluminescence. - Soot measurements: Light attenuation at 532 nm.	- Soot formation and oxidation are enhanced as U_{ox} increases. - Only soot formation increases with V_F.
(Fuentes, Rouvreau, et al. 2007)	**Exp.** - Burner – Ethylene **Num.** - A one-step reaction. - simulate soot parts trajectory	- Controlling mechanisms for soot production - Soot trajectory	U_{OX}, OI	- 10mW green laser diode (532 nm) is used as a backlighting source to measure with a CCD light attenuation.	- U_{ox} ▲ → ▼ Oxidation Residence time → f_S ▲ - It seems to indicate the presence of a maximum in the flame length and luminosity at oxidizer velocities below those encountered in natural convection.

(Fuentes, Legros, Claverie, et al. 2007)	**Exp. & Num. (same as above)**	- Understanding soot production. - To determine if the local ratio of soot formation/oxidation - Residence times controls the local soot volume fraction.	U_{OX} - OI	- Soot: LII CH*: Chemiluminescence	- U_{ox} ▲ → f_S ▲ - U_{ox} ▲ → L_f ▲ - U_{ox} ▲ → Luminousity ▲ - U_{ox} ▲ → Stand-off ▼
(Legros et al. 2009)	**Exp. & Num. (same as above)**	- To clarify the mechanisms by which local soot concentrations are defined in laminar diffusion flames and the effect of soot on trailing edge quenching, and thus on flame length.	Uox	**Exp** – Results were taken from Fuentes, 2007.	- U_{ox} ▲ → CH* emission ▲ - U_{ox} ▲ → Soot attenuation ▲ Soot production and oxidation vary not only with the magnitude of the Vox, but also depend on the distance from trailing edge.
(Legros and Torero 2015)	**Exp.** Burner-Ethylene	- Phenomenological model of soot production inside a non-buoyant laminar diffusion flame	U_{OX} V_F	**Exp.** OI :35%	$\frac{F_v}{V_F U_{ox}^{1/2}} = a \times \frac{x}{L_p} + b$ (a, b are constants)

1.2.4. Effects of oxygen index on soot production.

The question of how soot production is affected by varying the oxygen concentration in the oxidizer flow (called oxygen index and referred to as OI hereafter) of non-premixed flames is of practical interest in the design of oxy-fuel burners, applied to a variety of industrial processes in order to improve efficiency and pollution characteristics, where the generation of intermediate soot is desirable for increasing radiant heat transfer (Zelepouga et al. 2000).

Well-defined laminar flames were used in previous works to investigate the influence of varying the OI on soot production. Laminar flames offer more tractable configurations for analysis and experiments (Bento, Thomson, and Gülder 2006; Faeth 2001; Moss 1995) than the practical turbulent diffusion flames involved in combustion systems and fires. Moreover their use is justified by the similarities existing between laminar and turbulent diffusion flames and the results can be extrapolated to turbulent flames through approximate approaches like the laminar flamelet concept (Bento, Thomson, and Gülder 2006; Faeth 2001; Moss 1995). Experimental

studies of counterflow diffusion flames showed that soot production was enhanced with increasing the OI (Beltrame et al. 2001; D. X. Du, Axelbaum, and Law 1991; Hwang and Chung 2001; Leusden and Peters 2000; Vandsburger, Kennedy, and Glassman 1984), thermal effects being the main cause for this enhancement (D. X. Du, Axelbaum, and Law 1991; Leusden and Peters 2000). Encouraging numerical predictions in terms of flame structure and soot concentrations were also reported in oxygen-enriched counterflow configurations by using either a detailed soot formation model (Leusden and Peters 2000) or two-equation semi-empirical soot models (Beltrame et al. 2001; Guo, Liu, and Smallwood 2004; Liu et al. 2004).

Axisymmetric laminar diffusion flames were also experimentally and numerically investigated (Bennett et al. 2008; Glassman and Yaccarino 1980; Lee et al. 2000; Zelepouga et al. 2000). Bennett et al. (Bennett et al. 2008) provided accurate predictions of oxygen-enhanced axisymmetric laminar methane flames by considering a fully coupled fluid flow/detailed chemistry numerical model. However, soot formation was ignored. Glassman and Yaccarino (Glassman and Yaccarino 1980) investigated experimentally the influence of the OI on smoke point characteristics in ethylene diffusion flames. They found that the ethylene flow rate at the smoke point reached a maximum for an OI of 24%. Lee et al.(Lee et al. 2000) considered a well characterized methane flame, and two other methane diffusion flames with the same volumetric flow rate of fuel and with oxygen enrichments of 50% and 100%, respectively. A reduction in the mass of soot particles within the flame in both enrichment conditions was observed, with larger reduction for the methane/100% oxygen flame. On the other hand, they found that the peak of soot volume fraction followed a non-monotonic evolution with the OI with a maximum for the methane/50% oxygen flame. Zelepouga et al. (Zelepouga et al. 2000) used the same methane/air flame as Lee et al. (Lee et al. 2000) as a reference flame in order to study the influence of the addition of acetylene and polycyclic aromatic hydrocarbons on soot formation. Oxygen

concentrations of 35, 50, and 100% were also considered. The authors also observed a reduction in the overall mass of soot particles in the three cases whereas the peak of radially integrated soot volume fraction was found to increase between 21 and 35% and to decrease for OIs greater than 35%.

1.3. Overview of the manuscript

The manuscript is organized as follows: the second chapter is devoted to the presentation of the numerical model developed in this work. The governing equations are first presented, followed by the radiation model, the soot production model and the numerical procedure used to solve the transport equations.

Before applying the model to microgravity LBL diffusion flames, the model is used to simulate experiments performed at the University Féderico Santa Maria in Valparaiso (Chile) in the third chapter. The configuration considered is that of axi-symmetric laminar coflow diffusion flames fueled by ethylene. Different oxygen indexes, defined as the molar fraction of oxygen in the oxidizer, are considered ranging from under-oxygenated to over-oxygenated configurations. The simulations of these experiments are of particular interest for me for two reasons: first, I have participated to the development of the experimental set up and to the experiments when I was research engineer at the University Féderico Santa Maria. Secondly, these experiments are also of practical interest in the design of oxy-fuel burners, applied to a variety of industrial processes in order to improve efficiency and pollution characteristics, where the generation of intermediate soot is desirable for increasing radiant heat transfer (Baukal Jr. 1998).In particular, Oxy-fuel combustion for power generation with CO2 capture and storage is recognized as one of the key, promising technologies for cutting down global CO2 emissions and is currently developing in emerging countries as Chile.

The fourth chapter is devoted to LBL diffusion flames in microgravity. In a first part the experimental configuration, the varying parameters, and the experimental set up used by Fuentes during its Phd thesis (Fuentes 2006) are presented. Based on a dimensional analysis and on a simple scaling model some experimental data are presented, discussed and analyzed. The numerical results obtained by simulating the experiments are first compared with the

experiments. The results are then used to provide a better understanding of the soot formation process, of the resulting radiative heat transfer and of the flame quenching phenomena. In a last part, the influence of using approximate radiative property models on soot production and quenching phenomena is investigated.

Finally, the conclusions drawn from the present study and the perspectives for future works are presented in the fifth chapter.

2. Numerical Models

The main objective of this chapter is to show the mathematical model implemented in FORTRAN® programming language to simulate the flames studied in present work. The integral code integrates a CFD solution, complex chemical gas-phase mechanisms, soot model, coupled to a radiation model.

2.1. Flame model

The numerical simulation of the laminar ethylene diffusion flames studied in the present work, includes the solution of the overall continuity equation, the Navier–Stokes equations in a low Mach number formulation, and transport equations for gas-phase species mass fraction, the soot mass fraction, the soot number density per unit mass of mixture, and energy(Guo et al. 2006). The conservation equations are solved either in axisymmetric cylindrical or Cartesian coordinates using a finite volume method. Correction diffusion velocities in both directions were used to ensure that the mass fractions of gaseous species and soot sum to unity. The thermophoretic velocities of soot in both directions were accounted for, as were the interactions between the gas-phase chemistry and the soot chemistry. Diffusion terms in the transport equations are discretized by the central difference and the convection terms by the power law scheme (Patankar 1980). The SIMPLE algorithm (Patankar 1980) was used to treat the pressure and velocity coupling. Conservation equations of gas-phase species are solved in a fully coupled fashion at each control volume using a direct solver to ensure the convergence process. All other transport equations are solved using the tridiagonal-matrix algorithm.

2.1.1. Model set-up

Both axisymmetric and rectangular coordinates are considered keeping in mind applications to axisymmetric laminar co-flow diffusion (LCD) flames and laminar boundary layer diffusion (LBLD) flames, respectively. Fig. 2-1 shows schematically the two configuration flames as well as the coordinate system and computational domain.

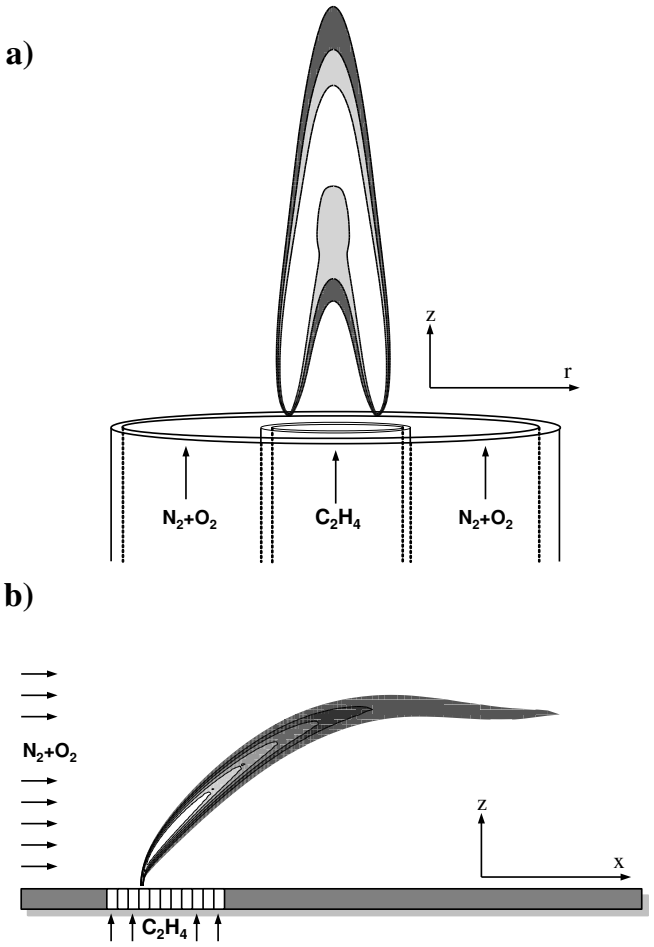

Figure 2-1: Schematic of a) laminar co-flow diffusion flame and b) laminar boundary layer diffusion flames.

2.1.2. Gas phase governing equations

The transport equations solved in present study can be summarized as follows (Kuo 1986):

$$\frac{\partial}{\partial t}(\rho\Phi)+\frac{1}{x}\frac{\partial}{\partial x}(x\rho v\Phi)+\frac{\partial}{\partial z}(\rho u\Phi)=\frac{1}{x}\frac{\partial}{\partial x}\left(x\Gamma_{\Phi x}\frac{\partial\Phi}{\partial x}\right)+\frac{\partial}{\partial z}\left(\Gamma_{\Phi z}\frac{\partial\Phi}{\partial z}\right)+S_{\Phi} \qquad (1.14)$$

Where x can be seen as a geometrical variable taking the value of r in axisymmetric cylindrical coordinates or 1 for Cartesian systems, Φ is the transported quantity, $\Gamma_{\Phi i}$ is the diffusion coefficient and S_{Φ} is the source term.

Table 2-1: Summary of the transport equations solved in simulations.

Eq.	Equation for	Φ	$\Gamma_{\Phi i}$	S_Φ
			Axi-symmetric cylindrical coordinates	
a	Continuity	1	0	0
b	Axial Momentum	u	μ	$\frac{\partial p}{\partial z}+\rho g_z+\frac{1}{r}\frac{\partial}{\partial r}\left(r\mu\frac{\partial v}{\partial r}\right)+\frac{\partial}{\partial z}\left(\mu\frac{\partial u}{\partial z}\right)-\frac{2}{3}\frac{\partial}{\partial z}\left[\mu\left(\frac{1}{r}\frac{\partial(\mathrm{v})}{\partial r}+\frac{\partial u}{\partial z}\right)\right]$
c	Radial Momentum	v	μ	$-\frac{\partial p}{\partial r}+\frac{1}{r}\frac{\partial}{\partial r}\left(r\mu\frac{\partial v}{\partial r}\right)+\frac{\partial}{\partial z}\left(\mu\frac{\partial u}{\partial r}\right)-\frac{2}{3}\frac{\partial}{\partial r}\left[\mu\left(\frac{1}{r}\frac{\partial(ru)}{\partial r}+\frac{\partial u}{\partial z}\right)\right]$
d	Energy	T	$\frac{\lambda}{c_p}$	$\sum_{k=1}^{KK+1}\left[\rho\frac{c_{pk}Y_k}{c_p}\left(V_{kr}\frac{\partial T}{\partial r}+V_{kz}\frac{\partial T}{\partial z}\right)\right]-\sum_{k=1}^{KK+1}\frac{h_k}{c_p}W_k\omega_k+\frac{q_r}{c_p}$
e	Gas Species	Y_k	ρD_k	$\frac{1}{r}\frac{\partial}{\partial r}\left(r\frac{D_k^T}{T}\frac{\partial T}{\partial r}\right)-\frac{1}{r}\frac{\partial}{\partial r}\left(\rho r Y_k\left(V_{cr}\right)\right)+\frac{\partial}{\partial z}\left(\frac{D_k^T}{T}\frac{\partial T}{\partial z}\right)-\frac{\partial}{\partial z}\left(\rho Y_k\left(V_{cz}\right)\right)+W_k\omega_k$
			Rectangular coordinate system	
f	Continuity	1	0	0
g	x-momentum	u	μ	$\frac{1}{3}\frac{\partial}{\partial x}\left(\mu\frac{\partial u}{\partial x}\right)-\frac{\partial y}{\partial x}\left(\frac{2}{3}\mu\frac{\partial v}{\partial z}\right)+\frac{\partial}{\partial z}\left(\mu\frac{\partial v}{\partial x}\right)$
h	z-momentum	v	μ	$\frac{1}{3}\frac{\partial}{\partial z}\left(\mu\frac{\partial u}{\partial z}\right)-\frac{\partial}{\partial z}\left(\frac{2}{3}\mu\frac{\partial v}{\partial x}\right)+\frac{\partial}{\partial x}\left(\mu\frac{\partial v}{\partial z}\right)+\rho g_z$
i	Energy	T	$\frac{\lambda}{c_p}$	$\sum_{k=1}^{KK+1}\left[\frac{\rho c_{pk}Y_k}{c_p}\left(V_{kx}\frac{\partial T}{\partial x}+V_{ky}\frac{\partial T}{\partial z}\right)\right]-\sum_{k=1}^{KK+1}\frac{h_k}{c_p}W_k\omega_k+\frac{q_r}{c_p}$
j	Gas Species	Y_k	ρD_k	$\frac{\partial}{\partial x}\left(\frac{D_k^T}{T}\frac{\partial T}{\partial x}\right)-\frac{\partial}{\partial x}\left(\rho r Y_k\left(V_{cx}\right)\right)+\frac{\partial}{\partial z}\left(\frac{D_k^T}{T}\frac{\partial T}{\partial z}\right)-\frac{\partial}{\partial z}\left(\rho Y_k\left(V_{cz}\right)\right)+W_k\omega_k$

The derivation of the equations presented in Table 2-1 can be found in the text book of (Kuo 1986). Velocities are represented by u and v for x- and r- for axi-symmetric, and x- and z- for Cartersian coordinate directions, respectively. Density of mixture (soot and gas) is ρ and g_z is the gravity acceleration. In the energy equation Eq. 1.14 d) and i), T is the temperature, λ is the thermal conductivity of the mixture and c_p is the specific heat of the mixture under constant

pressure. In the source term c_{pk} is the k^{th} species specific heat capacity under constant pressure, h_k h_k is the k^{th} species specific enthalpy, W_k the molecular weight of k^{th} species, ω_k the mole production rate of k^{th} species per unit volume, p is the pressure. It should be pointed out that the production rate of gas species include the contribution due to soot inception, surface growth and oxidation; V_{kx_i} is the diffusion velocity in x_i coordinate direction. The diffusion velocity can be written as:

$$V_{kxi} = V_{okx_i} + V_{Tkx_i} + V_{cx_i} \tag{1.15}$$

the three terms of right hand side are: ordinary diffusion velocity $\left(V_{okx_i}\right)$, thermal diffusion velocity $\left(V_{Tkx_i}\right)$ and correction diffusion velocity $\left(V_{cx_i}\right)$. The first velocity is computed for all species whereas the thermal diffusion is only considered for H and H_2. The ordinary diffusion velocity and thermal diffusion velocity of the k^{th} species are obtained by the approximate mixture-averaged formulation. The ordinary diffusion velocity and thermal diffusion velocity of the k^{th} species are obtained by the approximate mixture-averaged formulation (Kee et al. 1986).

$$V_{okx_i} = -\frac{1}{Y_k} D_k \frac{\partial Y_k}{\partial x_i} \tag{1.16}$$

$$V_{Tkx_i} = -\frac{D_k^T}{\rho Y_k} \frac{1}{T} \frac{\partial T}{\partial x_i} \tag{1.17}$$

where D_k^T is the thermal diffusion coefficient obtained by the method given by Kee et al. (Kee et al. 1986). The correction diffusion velocity $\left(V_{cx_i}\right)$ is used to ensure that the mass fractions of gaseous species and soot sum to unity (Kee et al. 1986). Quantity D_k in equation (1.16) is related to the binary diffusion coefficients through the expression:

$$D_k = \frac{1 - X_k}{\sum_{j \neq k}^{KK} \frac{X_j}{D_{jk}}} D_k \frac{\partial Y_k}{\partial x_i} \tag{1.18}$$

Where X_k is the mole fraction of the k^{th} species, and D_{jk} is the binary diffusion coefficient.

2.1.3. Radiative transport.

The effect of radiation transport appears in the last parameter of source term in the energy equation in equation **Erreur ! Source du renvoi introuvable.**. The term, q_r, is the divergence of the radiative heat flux $\left(\vec{\nabla}\cdot\vec{q}''\right)$ inside the medium taking account soot and gaseous species and corresponds to a balance of radiative heat.

2.1.3.1. Spectral radiative transfer equation (RTE)

The spectral RTE for an absorbing and emitting medium is expressed as (Modest 2013):

$$\frac{dI_\eta}{ds} = \kappa_\eta\left(\underline{\varphi}\right)\left[I_{b\eta}\left(T\right) - I_\eta\right] \tag{1.19}$$

Where $I_{b\eta}$ is the Planck function, κ_η is the absorption coefficient, both evaluated at the wavenumber η. The temperature is T and $\underline{\phi}(T, p, X_i, f_s)$ is an array of state variables affecting the absorption coefficient, i.e. the temperature, the molar concentrations of the radiatively participating gaseous species, X_i, the total pressure, p, and the soot volume fraction, f_s.

The total radiative flux, $\left(\dot{q}''\right)$, onto a surface element of normal $\vec{n}$ and the divergence of the total flux are expressed as (Modest 2013):

$$\dot{q}_n'' = \int_0^\infty \int_{4\pi} I_\eta \vec{n}\cdot\vec{s}\, d\Omega\, d\eta \tag{1.20}$$

$$\vec{\nabla}\cdot\vec{q}'' = \int_0^\infty \kappa_\eta \left(4\pi I_{b\eta} - \int_{4\pi} I_\eta d\Omega\right) d\eta \tag{1.21}$$

The spectral coverage range considered in the present study is 150-9300 cm^{-1}. The radiatively participating species considered are CO_2, H_2O, CO and soot.

2.1.3.2. Soot radiative properties

Soot particles were assumed to be spherical and small as compared with the wavelength, Rayleigh's theory then being applied to obtain the soot absorption coefficient. Scattering was ignored since it is negligible as compared with absorption within the limits of small particles. The spectral absorption coefficient of soot, $\kappa_{S,n}$, is then expressed as:

$$\kappa_{S,\eta} = C_\eta f_{vS} \eta \tag{1.22}$$

The diameter of the soot particles is so much smaller that the wavelengths of interest in emission calculations that the spectral absorption coefficient may be computed from the small particle limit of the Mie equation. In this limit, the spectral absorption coefficient of soot is proportional the soot volume fraction of space occupied by the particles independent of the particle size. In the present case, the constant C_η takes a value of 5.5 (Dalzell and Sarofim 1969).

2.1.3.3. Gas-phase radiative properties

The SNBCK model was found to be too much time consuming to be applied in studies involving a detailed chemistry. In order to accelerate the solution of the radiative heat transfer problem a wide band model was derived from the SNBCK described in the previous section. The accuracy and the efficiency of this approach, called the wide band correlated-k (WBCK) model, were established by Liu and co-workers (Liu, Smallwood, and Gulder 2000).

The spectrum was divided into NW=9 WBs with a spectral resolution of $\Delta\eta_{WB} = 500\,\mathrm{cm}^{-1}$. On each wide band (WB) *k*-distributions were assembled from a narrow band (NB) database, generated form high-temperature spectroscopic databases (Liu, Smallwood, and Gulder 2000), by using a lumping strategy:

$$g_i^{WB}\left(k, \underline{\varphi}\right) = \sum_{j=1}^{NB_i} \frac{\Delta\eta_{NB,j}}{\Delta\eta_{WB}} g_j^{NB}\left(k, \underline{\varphi}\right) \tag{1.23}$$

Where $\underline{\varphi}$ is an array of state variables that affects the absorption coefficient of the gas phase, k is the absorption coefficient variable at state $\underline{\varphi}$, NB_i is the number of NBs that compose the i^{th} WB (typically 20 with $\Delta\eta_{NB}$ of the order of 25 cm^{-1}). g_i^{WB} and g_j^{NB} are the cumulative k-distribution over the i^{th} WB and the j^{th} NB, respectively. Since the cumulative k-distribution is smooth and increases monotonically, integration over g-space can be performed by using a Gauss quadrature scheme with few points. In the present study, the number of quadrature points, N_G, is taken equal to 4 (Demarco et al. 2011). The RTE, for the i^{th} WB and for the k^{th} quadrature point and the total intensity are then expressed as:

$$\frac{dI_{gk}^i}{ds}+\left(k_k^i\left(g_k,\underline{\varphi}\right)+\kappa_{S\eta,i}\right)I_{gk}^i=\left(k_k^i\left(g_k,\underline{\varphi}\right)+\kappa_{S\eta,i}\right)I_{b\eta,i}\left(T\right) \tag{1.24}$$

$$\mathrm{I}=\int I_\eta d\eta=\sum_{i=1}^{NW}\sum_{k=1}^{N_G}I_{gk}^i w_k\Delta\eta_{WB} \tag{1.25}$$

where the blackbody intensity, $I_{b\eta}$, and $\kappa_{s,\eta}$ are evaluated at the center of the WB. The quadrature points and the corresponding weights, are represented by g_k and w_k, respectively. For each WB and each quadrature point, the low dependence of spectral line broadening on the species mole fraction was disregarded and the temperature-related part of the corresponding absorption coefficients for the gas phase were fitted as a function of temperature by 9th order polynomials. During the sequence of calculation, the absorption was computed as:

$$\kappa_\eta=\left[\left(a_{CO_2}x_{CO_2}+a_{H_2O}x_{H_2O}+a_{CO}\,x_{CO}\right)\times p\right]+5.5f_s\nu \tag{1.26}$$

The terms a_i are computed as

$$a_i=\sum_{j=1}^{9}A_{ij}T^{j-1} \tag{1.27}$$

Where A_{ij} is the polynomial coefficient of a species expressed as a function of temperature (Ju et al. 1997).

2.1.3.4. Discrete Ordinate Method (DOM)

The discrete ordinates method is based on a discrete representation of the directional variation of the radiative intensity. A solution to the transport problem is found by solving the RTE, equation (1.19), for a set of discrete directions spanning the total solid angle range of 4π. As such, the discrete ordinates method is simply a finite differencing of the directional dependence of the equation of transfer. Integrals over solid angle are approximated by numerical quadrature (Modest 2013).

DOM is a general algorithm that can describe radiation transport in a media which is optically thin, thick or intermediate. It is not necessary to make a preliminary estimate of the optical thickness of the media being studied since the DOM algorithm is valid for any level of opacity. Another advantage of the DOM algorithm is the ease with which it can be readily incorporated into multidimensional finite-volume codes. The discretization of RTE using DOM is presented in Appendix A.

The radiative transfer equation, equation (1.19), is numerically solved in as described by (Fiveland 1984). The T_7 quadrature (Thurgood, Pollard, and Becker 1995) is used for axi-symmetric coordinates whereas the T_3 (Thurgood, Pollard, and Becker 1995) is used in Cartesians coordinates. Either a central or an upwind scheme is used for the spatial discretization.

2.1.3.5. Optically Thick Approximation (OTA)

Optically Thick Approximation model neglects the gas and soot re-absorption, assuming that the medium is optically thin (Modest 2013). For an optically thin medium, the integral term of equation (1.21) is negligible, and the divergence of the radiative flux may be calculated without having to solve the integro-differential radiative transfer equation (RTE). Thus, the divergence of radiative flux is computed as:

$$\vec{\nabla}\cdot\vec{q}'' = \int_0^\infty \kappa_\eta \left(4\pi I_{b\eta}\right) d\eta \tag{1.28}$$

The absorption coefficient κ_η is computed taking account the radiative effects of gases CO_2, H_2O and CO, but also adding the soot radiation effect through the last term of equation (1.22)

2.2. Soot model

Assuming that the polycyclic aromatic hydrocarbons (PAHs) are the precursors of soot formation, the model can be described as a sequence of steps (M. Frenklach and Wang 1991): (1) fuel pyrolysis, (2) formation of the first PAH, (3) PAH planar growth and coagulation into spherical particles, and finally, (4) surface growth and oxidation of particles. In addition soot particles may undergo coagulation and agglomeration. Fuel pyrolysis and formation of the first PAH are modeled by a detailed gas-phase reaction mechanism. Once the first aromatic ring (Benzene, A1) is formed, PAHs grow by a sequential two-step process: H-abstraction which activates the aromatic molecules, and acetylene addition which propagates molecular growth and cyclization of PAH. This sequential mechanisms is known as HACA (Appel, Bockhorn, and Frenklach 2000). This step is also included in the detailed gas-phase reaction mechanism. The modeling of soot production requires addressing two other issues. The first is related to the soot chemistry in order to describe the very first inception of a soot particle from gaseous species and its growth and oxidation. The second is related to the particle dynamic in order to describe the size distribution of the soot.

2.2.1. Gas-phase reaction mechanism

The gas-phase chemistry was modeled using detailed gas-phase reaction mechanisms, where chemistry was described by a collection of elementary reactions. The thermal properties of the gaseous species, their chemical reaction rates and their transport properties, which include gas-phase multicomponent viscosities, thermal conductivities, diffusion coefficients, and thermal diffusion coefficients, are obtained using the CHEMKIN (Kee et al. 1996) and TRANSPORT (Kee et al. 1986) libraries and the database associated with the reaction mechanism selected.

For axisymmetric simulations, the mechanism developed by (Appel, Bockhorn, and Frenklach 2000) which was based on the earlier work of Wang and Frenklach (H. Wang and Frenklach 1997) is used to describe the pyrolysis and oxidation of the initial C_2H_4 fuel. It includes the pyrolysis and oxidation of C_1 and C_2 species, the formation of higher, linear hydrocarbons up to C_6 species, the formation of benzene and further reactions leading to pyrene (A_4, with 4 aromatic rings, molecular formula: $C_{16}H_{10}$), as well as the oxidation pathways of the aromatic species. The description of the small hydrocarbon reactions is founded on GRIMech1.2,

one of the most consistent and reliable description of C_1 combustion chemistry. The formation of benzene and phenyl is described by reactions of C_4H_x species with acetylene, by cyclization reactions of C_6H_x species, and the combination of propargyl radicals. The formation path of pyrene starting with benzene follows the HACA reaction sequence, along with the ring-ring condensation (i.e. via the formation of biphenyl (M. Frenklach et al. 1988). The mechanism is fairly large, containing 101 species and 544 reactions.

For the laminar diffusion boundary layer flames (LBLDF), studied in Chapter 1, the gas-phase chemical kinetic mechanism developed by (Slavinskaya and Frank 2009) is used. It consists of three sub mechanisms namely (i) methane oxidation, as the base chemistry for all hydrocarbons; (ii) ethylene oxidation, which is the key reaction set in oxidation of alkanes; and (iii) PAH formation up to five rings. This mechanism was developed to predict the formation of PAH and their growth of up to five aromatic rings in methane and ethane-fueled flames.

The formation of the first aromatic ring specie (A_1 – Benzene) is performed in 12 reactions. The mechanism has been developed to include almost all reasonably well-established reaction classes for aromatic ring formation and soot particle molecular weight growth precursors (Slavinskaya and Frank 2009). The model was initially validated for zero- and one-dimensional premixed flame systems (Slavinskaya and Frank 2009) and then was updated and extended to a sooting ethylene/air diffusion flame in the co-flow geometry (Dworkin et al. 2011). The mechanism contains 94 species and 723 reactions.

2.2.2. Soot particle dynamic

In present work, the primary soot particles are assumed to be spherical and locally monodisperse. Thus only the two firsts moments of the soot particle size distribution (PSD) function (Leung, Lindstedt, and Jones 1991) need to be solved, namely, the mass concentration of soot particles (ρY_S) and the soot number density (ρN_S). Hence, two additional transport equations are coupled in order to predict the soot production (Leung, Lindstedt, and Jones 1991). The two additional equations are:

$$u\frac{\partial(\rho Y_s)}{\partial x}+\rho v\frac{\partial(\rho Y_s)}{\partial z}=\frac{\partial}{\partial x}\left[\rho V_{T,x}(\rho Y_s)\right]-\frac{\partial}{\partial z}\left[\rho V_{T,y}(\rho Y_s)\right]+S_m \tag{1.29}$$

$$\rho u\frac{\partial(\rho N_s)}{\partial x}+\rho v\frac{\partial(\rho N_s)}{\partial z}=\frac{\partial}{\partial x}\left[\rho V_{T,x}(\rho N_s)\right]-\frac{\partial}{\partial z}\left[\rho V_{T,y}(\rho N_s)\right]+S_N \tag{1.30}$$

The last term of equation (1.29) is the soot mass source term and is defined as $S_m = R_1 + R_2 + R_c - R_{O_2} - R_{OH}$. It accounts for the contribution of soot nucleation (R_1), surface growth (R_2), PAH-surface condensation (R_c) and oxidation by O_2 (R_{O_2}) and by OH (R_{OH}). In turn, the source term in equation (1.30) is defined as $S_m = R_0 - R_{agg}$, where soot particle nucleation $\left(R_0\right)$ and particles agglomeration $\left(R_{agg}\right)$ are taken into account. Both source terms are described in next section.

Conservation equations for the soot mass concentration and number density are solved in the present model along with the gaseous species in the solution domain. As soot particles do not follow the molecular diffusion theory, the diffusion velocities in the soot conservation equations are replaced by the corresponding thermophoretic soot particle velocity $\left(V_{T,x_i}\right)$ (Talbot et al. 1980) and is calculated as:

$$V_{T,x_i} = -0.55 \frac{\mu}{(\rho T)} \frac{\partial T}{\partial x_i} \tag{1.31}$$

2.2.3. Soot processes

This section describes the two source terms of Eqs. (1.29) and (1.30), the mass source term $\left(S_m\right)$ and the soot particle number source term $\left(S_N\right)$, respectively. These terms are described in terms of reaction rates for unit volume for processes considered. The units are then (g/cm^3/s) for S_m and (part/cm^3/s) for S_N.

2.2.3.1. Nucleation model

Up to now, particle inception is the least understood process of soot formation in hydrocarbon combustion. It is widely accepted that gaseous precursors of solid soot particles are polycyclic aromatic hydrocarbons (PAH) (M Frenklach and Wang 1994; Schuetz and Frenklach 2002). However, the understanding of this transformation in mechanistic terms is far from being complete. The state of the art of nucleation modeling is to assume soot nucleates through the collision and sticking of PAH species to form a "dimmer". Pyrene (A_4) is generally assumed to

be the only PAH species responsible of nucleation. Thus, mass nucleation rate $\left(R_1\right)$, in (g/cm^3/s) is defined as:

$$R_1 = 2 N_{c,A_4} m_c R_0 \tag{1.32}$$

Where N_{c,A_4} is the number of carbon atoms in the nucleation PAH species (16 for pyrene), m_c is the mass of carbon atom; in present work it was considered as $12 \times$ AMU (where AMU is equal to 1.6710^{-24} g). R_0 corresponds to soot particle nucleation rate (particles/cm^3/s), derived from collision theory (see Appendix A), and is computed as:

$$R_0 = 2.2 N_{av}^2 \left[A_4\right]^2 \left(\frac{4\pi k_B T}{m_{A_4}}\right)^{1/2} \left(d_{A_4}\right)^2 \tag{1.33}$$

Where N_{av} is the Avogradro number $\left(6.022\times10^{23}\text{part/mole}\right)$, $\left[A_4\right]$ the molar concentration of pyrene, k_B the Boltzmann constant $\left(1.3807\times10^{-16}\text{erg/K}\right)$ and d_{A_4} is the collision diameter of the nucleation PAH. The constant 2.2 represents an enhancement coefficient owing to Van der Wall forces (Harris and Kennedy 1988; Kennedy 1987). It was assumed that the diameter of *A4* is related to content of carbon atom according to (Lindstedt 1994):

$$d_{A_4} = 1.395\sqrt{2N_{c,A_4}} \tag{1.34}$$

2.2.3.2. Surface growth and oxidation

Apparently, the surface growth is the primary process responsible of the yield of soot mass. Thus, a kinetic model is required to simulate the heterogeneous soot-gas surface reactions. The soot surface growth model used in this thesis is based on the HACA soot surface reaction scheme developed by Frenklach and coworkers (Appel, Bockhorn, and Frenklach 2000; M Frenklach and Wang 1994; M. Frenklach and Wang 1991). Reactions of with O_2 and OH are added into HACA reaction scheme to account for soot oxidation. The whole soot surface reaction scheme is detailed in Table 2-2 taken from (Appel, Bockhorn, and Frenklach 2000).

Table 2-2: HACA-based soot surface growth and oxidation reactions and reaction rate parameters for $k = AT^n e^{(-E/RT)}$. $C_{soot} - H$ represents an active site on the soot particle surface and $C^{\bullet}_{soot}$ is the corresponding radical.

N°	Reaction	A (cm^3/mol/s)	n	E (kcal/mol)
S1	$(C_{soot}\text{-}H) + H \Leftrightarrow C^{\bullet}_{soot} + H_2$	4.2×10^{13}	--	13.0
S2	$(C_{soot} - H) + OH \Leftrightarrow C^{\bullet}_{soot} + H_2O$	1.2×10^{10}	0.734	1.43
S3	$C^{\bullet}_{soot} + H \Rightarrow C_{soot} - H$	2.0×10^{13}	--	--
S4	$C^{\bullet}_{soot} + C_2H_2 \Rightarrow C_{soot} - H + H$	8.0×10^{7}	1.56	3.8
S5	$C^{\bullet}_{soot} + O_2 \Rightarrow 2CO + Products$	2.2×10^{12}	--	7.5
S6	$C_{soot} - H + OH \Rightarrow CO + Products$		$\gamma_{OH} = 0.06$	

Reaction of soot oxidation with OH (S6) is modeled based on the formulation of (Fenimore and Jones 1967) and a collision factor $\gamma_{OH} = 0.06$ is considered (Guo et al. 2006). The kinetics of other surface reactions are described using the concept of surface sites (an armchair site on the particle surface), which are carbon atoms either saturated $(C_{soot}\text{-}H)$ or radical/dehydrogenated $(C^{\cdot}_{soot})$. An important parameter to be considered is the number density of radical $(C^{\cdot}_{soot})$ sites, $\chi_{C^{\bullet}_{soot}}$ representing the possible available sites to proceed with acetylene addition. The active sites are assumed to be created and destroyed faster than the other species. As a consequence, these reactions can be considered in a quasi-steady state regime, leading to the following expression for the number density of radical sites:

$$\chi_{[C^{\cdot}_{soot}]} = \frac{\left\{k_{f1}[H] + k_{f2}[OH]\right\}}{\left\{k_{r1}[H_2] + k_{r2}[H_2O] + k_{f3}[H] + k_{f4}[C_2H_2] + k_{f5}[O_2]\right\}} \times \chi_{[C_{soot}-H]} \tag{1.35}$$

The number density of sites per particle surface ($\chi_{[C_{soot}-H]}$) is considered constant and the value adopted has been taken from (Appel, Bockhorn, and Frenklach 2000) and corresponds to 2.3×10^{15} (sites/cm^2).

The HACA reaction scheme also uses an empirical (steric) parameter α to account for the fraction of surface sites available for a given reaction. Physically, it takes into account the probability of a gaseous species colliding with the prismatic (edge) planes instead of unreactive

basal planes of particles and the fact that not all of the edge carbons are available for a given reaction. The rates for mass surface growth (R_2), oxidation by O_2 (R_{O_2}) and oxidation by OH R_{OH} in (g/cm^3/s) are computed from:

$$R_2 = 2\alpha \times \frac{k_{f,S4} \times [C_2H_2] \times \chi_{[C_{soot}^{\bullet}]} \times A_S \times M_c}{N_A} \tag{1.36}$$

$$R_{O_2} = 2\alpha \times \frac{k_{f,S5} \times [O_2] \times \chi_{[C_{soot}^{\bullet}]} \times A_S \times M_c}{N_A} \tag{1.37}$$

$$R_{OH} = -1.27 \times 10^2 \times \gamma_{OH} \times \frac{P_{OH}}{\sqrt{T}} \times A_S \tag{1.38}$$

Where M_c is the molar mass of soot (12.0 g/mol).

2.2.3.3. PAH-surface condensation

The collision of PAH species with a soot particle and the resultant condensation leads to an increase in the mass of the soot without changing the soot number density. Various PAH species may be involved in the process of condensation; only pyrene is considered as the condensation species in this study (Appel, Bockhorn, and Frenklach 2000). The soot mass growth rate term owing to PAH-surface condensation is computed using the same principle as used for soot particle nucleation rate, based on the collision theory between pyrene molecules and soot aggregates (Park et al. 2005). Then, the R_{cond} term is computed as:

$$R_{cond} = 2.2\gamma_{cond} M_c N_{c,A4} \left[\frac{\pi k_B T}{2 M_C N_{c,A4}} \right]^{1/2} N_S N_A \left(d_{soot} + d_{A_4} \right)^2 \tag{1.39}$$

In order to account for the probability that a collision between one pyrene and a soot aggregate leads to condensation, ac collision efficiency coefficient for PAH-surface condensation, γ_{cond}, is considered. The value of γ_{cond} is taken equal to 0.5 (Q. Zhang 2009).

2.2.4. Agglomeration

Soot agglomeration is a process affecting the soot number density due to the collision of two soot particles (Lindstedt 1994).

$$R_{agg} = 2C_A \times (\rho N_s)^2 \times \sqrt{\frac{6k_B T}{\rho_s}} \times \left(\frac{6M_c}{\pi\rho_s}\right)^{1/6} \times (\rho Y_s)^{11/6} [C_S]^{1/6} \quad (1.40)$$

Where $[C_S]$ is the mole concentration of soot particle (mole/cm^3) and C_A is the agglomeration rate constant taken as equal to 1, meaning that every collision of two soot particles become agglomerated.

2.3. Boundary conditions

The boundary conditions are described in follow table.

Table 2-3 : Boundary conditions.

Boundary	Conditions
Inlet	$u=U_{inj}$; $v=V_{inj}$; $Y_i=Y_{i,inj}$; $\partial p/\partial n = 0$
Solid wall	u=0 ; v=0 ; $\partial\Phi/\partial n = 0$
Outlet	$\partial\Phi/\partial n = 0$; p= p_{atm}
Free slip	$\partial\Phi/\partial n = 0$
Symmetry axis	v=0 ; $\partial u/\partial n = 0$ $\partial u/\partial n = 0$; $\partial\Phi/\partial n = 0$

The boundary conditions to solve the radiative transfer equation (described in Appendix A) have been established in all boundaries as cold wall.

2.4. Numerical method

After being written in the general transport equation form, the gas-phase governing equations and the soot transport equations are discretized based on the infinite volume method. The Semi-Implicit Method for Pressure Linked Equations (SIMPLE algorithm) is used to handle the pressure and velocity coupling (Patankar 1980). The continuity equation is converted into the pressure correction equation. A staggered mesh is used to formulate the discretized equations for velocities and scalars. The diffusive terms are discretized by the second order central difference scheme while the convective terms are discretized by the power law scheme (Patankar 1980). A Pseudo-time marching method is used to achieve convergence. The momentum, pressure correction and energy equations are solved in a segregated manner using the Tri-Diagonal Matrix Algorithm (TDMA). Since the gaseous species equations are normally closely coupled and stiff , they are solved simultaneously at each control volume (Smooke, Mitchell, and Keyes 1986) to deal effectively with the stiffness of the system and speed up convergence. The key point of this method is to linearize the current time step chemical reaction source terms by using Taylor series expansions based on the previous time step values and neglecting the second and higher order terms. The resulting Jacobian matrices are obtained by the perturbation method (Kee et al. 1986). A direct solver (Gauss elimination method) is used to solve the resulting linear system at each control volume. The species equations are solved control-volume-by-control-volume until the whole computational domain is covered.

3. Oxygen Index Effect on Axysymmetric Diffusion Flames

This chapter describes the work performed to study the effects of oxygen index, here after OI, in the flame structure and soot formation/oxidation controlling mechanisms of steady axisymmetric laminar co-flow diffusion flames. This kind of flame configuration has a relatively simple flow field and thus is a convenient configuration to study both numerically and experimentally diffusion flames. On the other hand, these flames are multi-dimensional and thus provide a convenient platform for studying the formation of soot aggregates and the interactions between soot formation and gas-phase chemistry in a multi-dimensional scenario. Such flames enclose regions from soot nucleation all the way to soot oxidation hence provide opportunities to study all the soot formation/oxidation processes.

3.1. Experiments

The experiment set-up and diagnostic technique are described in (Fuentes et al. 2013). The experimental configuration involves a burner consisting of two concentric steel tubes (Guo et al. 2006). The fuel flows through the central tube and the oxidizer is injected trough the outer one. The inner diameters are 10 mm for the fuel tube and 100 mm for the oxidizer tube. Experimental conditions are summarized in Table 3-1. The fuel volume flow rate is fixed at 2.35cm^3/s**.** The oxidizer is a mixture of oxygen and nitrogen in which the oxygen is fixed at 20 L/min. The oxygen index is varied from 17% to 35% by decreasing the nitrogen flow rate from 97.6 L/min to 37.1 L/min, these flow rates being injected at ambient temperature. The radial profiles of soot volume fraction are determined from extinction measurements carried out at a wavelength of 670 nm by using the deconvolution procedure described in (Dasch 1992; Daun et al. 2006) and by assuming that soot particles are within the Rayleigh regime. Flame height measurements were based on CH* emission.

Table 3-1: Experimental conditions: the second, third and fourth columns represent respectively the fuel flow rate, the oxidizer flow rate and the flame residence time computed as $\tau = \int_0^{h_f} dz / u_z \left(r = 0, z \right)$.

Oxidizer composition	V_F (cm^3/s)	U_{OX} (l/min)	U_{OX} (cm/s)	τ (s)
$17\%O_2 + 83\%N_2$	3.89 (2.35)	117.6	24.41	0.131
$21\%O_2 + 79\%N_2$	--	95.2	19.76	0.119
$25\%O_2 + 75\%N_2$	--	80	16.60	0.107
$29\%O_2 + 71\%N_2$	--	69	14.32	0.097
$33\%O_2 + 67\%N_2$	--	60.6	12.57	0.089

3.2. Computational details

3.2.1. Chemical mechanism

In order to determine the flame structure (gas-phase mechanism) and to describe the evolution of the soot particle ensemble (soot particle dynamics), the detailed kinetic model of soot formation developed by Appel et al. (Appel, Bockhorn, and Frenklach 2000) was chosen. The model considers a full chemical kinetic scheme consisting of 99 species and 538 reactions was considered. It includes the pyrolysis and oxidation of $C_1$and C_2species, the formation of higher, linear hydrocarbons up to C_6species, the formation of benzene and further reactions leading to pyrene, as well as the oxidation pathways of the aromatic species.

Following the works of Xu and coworkers (Xu, Dai, and Faeth 2002) and Guo and coworkers (Liu et al. 2006) the steric factor is given by

$$\alpha = 0.0040 \times \exp\left(9000/T\right) \tag{3.1}$$

3.2.2. Computation domain and boundary conditions

The overall computational domain is 3.21 cm (r) × 9.72 cm (z) is shown in Figure 3-1. A preliminary grid refinement study indicated that a non-uniform mesh with 79 (r) × 158 (z) cells was adequate to achieve grid-independent results. A parabolic profile is imposed on the fuel

stream inlet, while a flat profile is considered for the oxidizer injection. Fuel and oxidizer are injected at ambient temperature (300 K), neglecting the effects of fuel pipe preheating by the flame base. Ambient pressure is fixed to 1 atm. The fuel inlet velocity corresponds to a fuel flow rate of 2.35 cm^3/s.

The numerical domain and boundary conditions are given in Figure 3-1. The reader is referred to Table 2-3 to have a detailed explanation of the different type of boundary conditions.

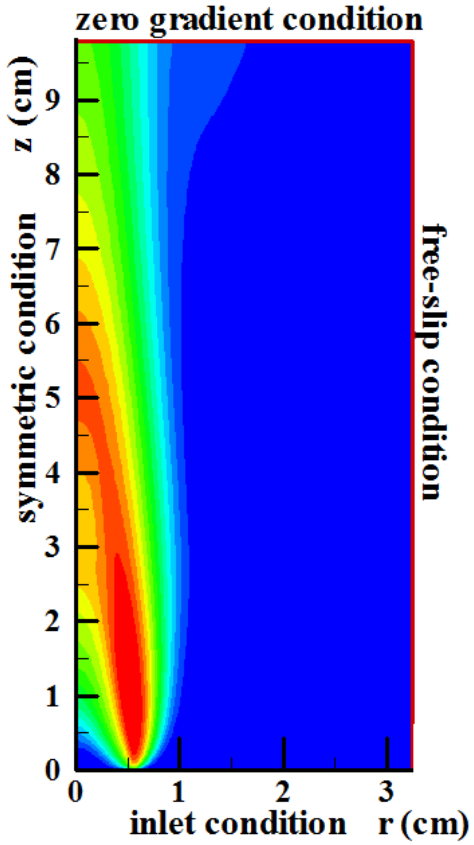

Figure 3-1: Domain and boundary conditions.

3.3. Results and discussion

3.3.1. Flame Structure and comparison with experimental data

Flame height is an important characteristic of co-flow laminar diffusion flames, since flame height measurements can be used to test models of flame structure (Mcenally et al. 2000) and to estimate residence times of soot particles (J. Du 1995). Figure 3-2 shows that both

experimental and numerical flame heights increase linearly with $\zeta = \dot{V}_f \left[D_\infty \ln\left(1+1/S\right) \right]^{-1} \left(T_\infty / T_{ad} \right)^{0.67}$ which is taken from the analysis of Roper (Roper 1977). This analysis predicts that evolution of the flame length above the port, h_f, for a circular burner diffusion flame is proportional to ζ. D_∞, S and T_{ad} represent the diffusion coefficient at ambient temperature, T_∞, the molar air to fuel ratio, and the adiabatic flame temperature. To be consistent with the experimental measurements, numerical flame heights were defined as the height where the maximum CH* concentration is reached (Fuentes et al. 2013) along the flame centerline. The numerical results agree well with the experimental data which suggests that the numerical model reproduces accurately the flame height. It can be noted that flame height for the OI 29% and 33%; which are slightly above the smoke point shows the same behavior as the other measurements.

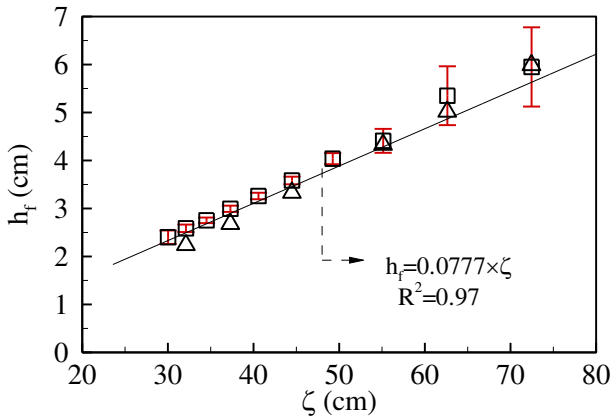

Figure 3-2: Measured and numerical flame heights as a function of ζ. Squares correspond to experimental results for a fuel flow rate of 2.35 cm^3/s. Triangles correspond to numerical results.

The predicted and experimental radial profiles of soot volume fraction are compared in Figure 3-3 for three OIs of 21% (Figure 3-3a), 25% (Figure 3-3b), and 29% (Figure 3-3c). For each OI the results for three axial locations are presented: low in the flame, where soot particles undergo nucleation and growth, near the middle of the flame, where the maximum soot volume fraction occurs, and higher in the flame, where soot is oxidized. Numerical profiles are in reasonable agreement with the experimental data: whatever the OI and the part of the flame considered the magnitude of the peaks is well captured by the numerical model. However the peak locations are generally shifted outwards as compared with the experiments, this trend being more pronounced in the lower part of the flame. This later behavior was also observed in a

previous study where the semi-empirical acetylene-based two-equation soot model proposed by (Leung, Lindstedt, and Jones 1991) was considered.

Figure 3-3d shows the evolution of the maximum soot volume fraction as a function of the OI. As was discussed in work developed by (Fuentes et al. 2013), the evolution of the soot formation process with the OI results from a competition between an enhancement of the soot formation rate and a reduction in residence time due to shortened flame length (see the fifth column of Table 3-1). The experimental data reported in Figure 3-3d suggest that, for the flames under consideration, the first mechanism dominates leading to higher values of the maximum soot volume fraction as the OI increases. They also show that the rate of increase is considerably reduced for OI greater than 25%. Previous simulations of these flames using an empirical acetylene-based soot model were presented in (Fuentes et al. 2013) and the maximum soot volume fractions, obtained with this model, are also shown in Figure 3-3d. The comparison of these numerical results with the experimental data shows that the rate of increase in soot volume fraction with OI is greatly over-predicted in both regimes. As a consequence, substantial discrepancies are observed: the predicted soot volume fraction is under-predicted by a factor of 2.84 for an OI of 17% and over-predicted by a factor of 1.62 for an OI of 33%. Figure 3-3d shows that predictions are significantly improved when considering the PAH-based soot model. The maximum soot volume fractions are found in reasonably good agreement with the experimental data for OIs up to 30% and the rate of increase in the maximum soot volume fraction with OI is well reproduced in the first regime. Nevertheless, the reduction in the rate of increase observed experimentally in the second regime is not reproduced and the maximum soot volume fraction is overestimated by 27% for an OI of 33%. On the other hand, the large discrepancies obtained with the C_2H_2-based soot model for an OI of 17% were previously attributed to combustion conditions close to flame blow-off (Fuentes et al. 2013). The present results reveal that this argument does not hold and the observed-discrepancies were due to the semi-empirical nature of the acetylene-based soot model.

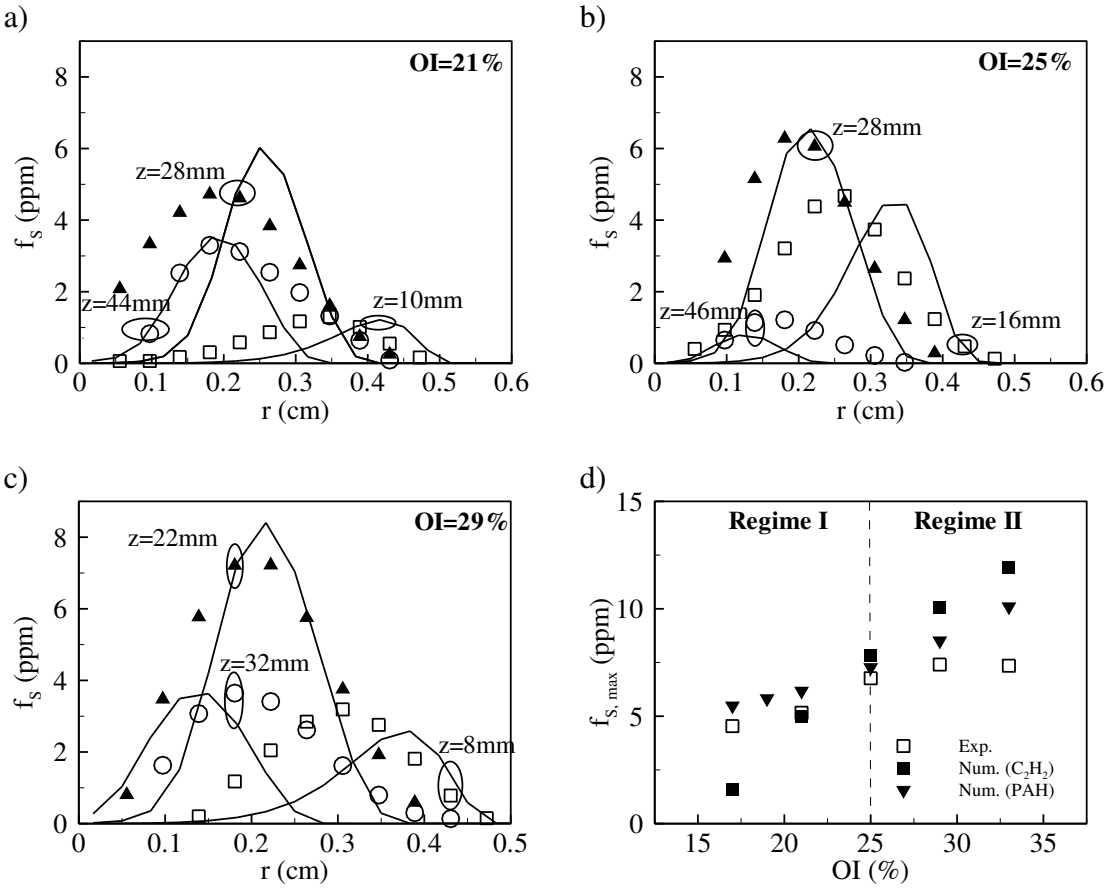

Figure 3-3: Radial profiles of soot volume fraction for three OIs: (a) 21%, (b) 25% and (c) 29%. (d) The maximum soot volume fraction as a function of the OI.

The evolutions of both computed and experimental integrated soot volume fractions, defined as $F_v = 2\pi \int r f_S dr$, as a function of the height normalized by ζ for OIs of 17%, 25% and 29% are displayed in Figure 3-4a. The use of this normalized height was found to provide a reasonably good scaling in terms of location of the maximum of integrated soot volume fraction (Fuentes et al. 2013). Figure 3-4a shows that the F_v profiles can be divided into two regions: a soot growth region where F_v increases with height followed by a soot oxidation region where F_v decreases with height. The experimental profiles are reasonably well reproduced by the PAH-soot model: the magnitude of the maximum and their location are accurately predicted. However, Figure 3-4a shows that the rates of oxidation are overestimated whatever the OI considered. The profile calculated with the C_2H_2-based soot model for an OI of 17% is also plotted in Figure 3-4a

to further illustrate the substantial improvement provided by the PAH-based soot model in under ventilated conditions. The evolution of the maximum integrated soot volume fraction with the OI is summarized in Figure 3-4b. Both soot models provide a satisfactory agreement with the experimental data for OIs greater than 25% whereas the PAH-based soot model improves significantly the prediction for OIs lower than 25%.

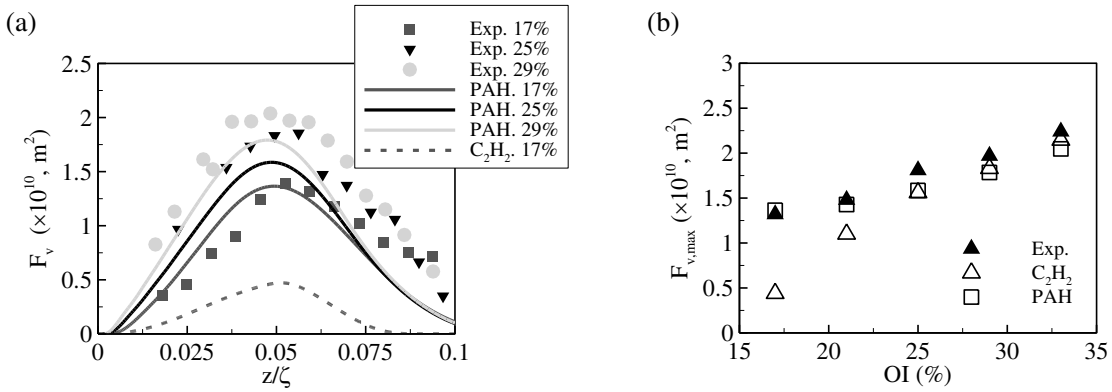

Figure 3-4: a) Distribution of the integrated soot volume fraction as a function of the height normalized by ζ, b) The maximum integrated soot volume fraction as a function of the OI.

3.3.2. Controlling mechanisms

The objective of this section is to provide further insights into how variation in the ambient concentration of oxygen affects soot formation and oxidation rates. To do that, not only formation and oxidation rates are displayed in Figure 3-5 and Figure 3-6, respectively, but also the species related to these processes. Thus, Figure 3-5 compares the distributions of nucleation rate (R_1) and surface growth rate (R_2) for two OIs of 17% and 25%. Also we show the distribution field of pyrene (A_4), acetylene (C_2H_2) and hydrogen radical (H*). The first species is directly linked to soot nucleation as was described in Section 0. The second participates in surface growth process. In turn the hydrogen radical is the active player is HACA scheme (See Table 2-2). As expected soot mass growth is dominated by surface growth mechanism with a difference of three orders of magnitude with nucleation process and this could be confirmed by low mol concentration of pyrene. Both nucleation and surface growth rates are enhanced as the

OI increases. The resulting increase in flame temperature is expected to lead higher rates for soot nucleation and growth mechanisms (D. X. Du, Axelbaum, and Law 1991; Leusden and Peters 2000), being the primarily reason for this enhancement (see Figure 3-5c). However, it is interesting to observe that the molar concentration in pyrene, acetylene, and hydrogen radical are also higher for an OI of 25% which also contributes to promote nucleation and surface growth.

The rates of oxidation (R_{OH} and R_{O_2}), as the concentration of species related (OH and O_2) and soot volume fraction are displayed in Figure 3-5 also for OIs of 17% and 25%. Firstly, we see that both oxidation processes occur in an annular zone with the OH oxidation rate process occupying a larger zone, probably because of a larger zone of the presence of OH on the reaction zone. In turn, O_2 oxidation starts after, in a zone where more O_2 coming from oxidizer flow can be found. Figure 3-6 shows clearly that the contribution of OH dominates soot oxidation whatever the OI considered. Figure 3-6c shows that the molar fractions of hydroxyl radicals are higher for an OI of 25%, explaining that larger oxidation rates are observed in this case (see Figure 3-6a). OH and O2 oxidation rate processes stop relatively at the same location

Figure 3-6b shows that, in spite of higher oxygen concentration in oxidizer flow, the rate of oxidation by O_2 follows an opposite trend, being slightly more efficient on the whole for an OI of 17% than for an OI of 25%. Soot oxidation rate by O_2 is dependent on temperature, concentrations of O_2, and also on soot concentration as well: a careful examination of the corresponding fields show that, in the regions where the maximum oxidation of soot by O2 occurs, the temperature are higher for an OI of 25% whereas O_2 and soot concentrations are higher for an OI of 17%, as shown in Figure 3-6 d), e), and f).

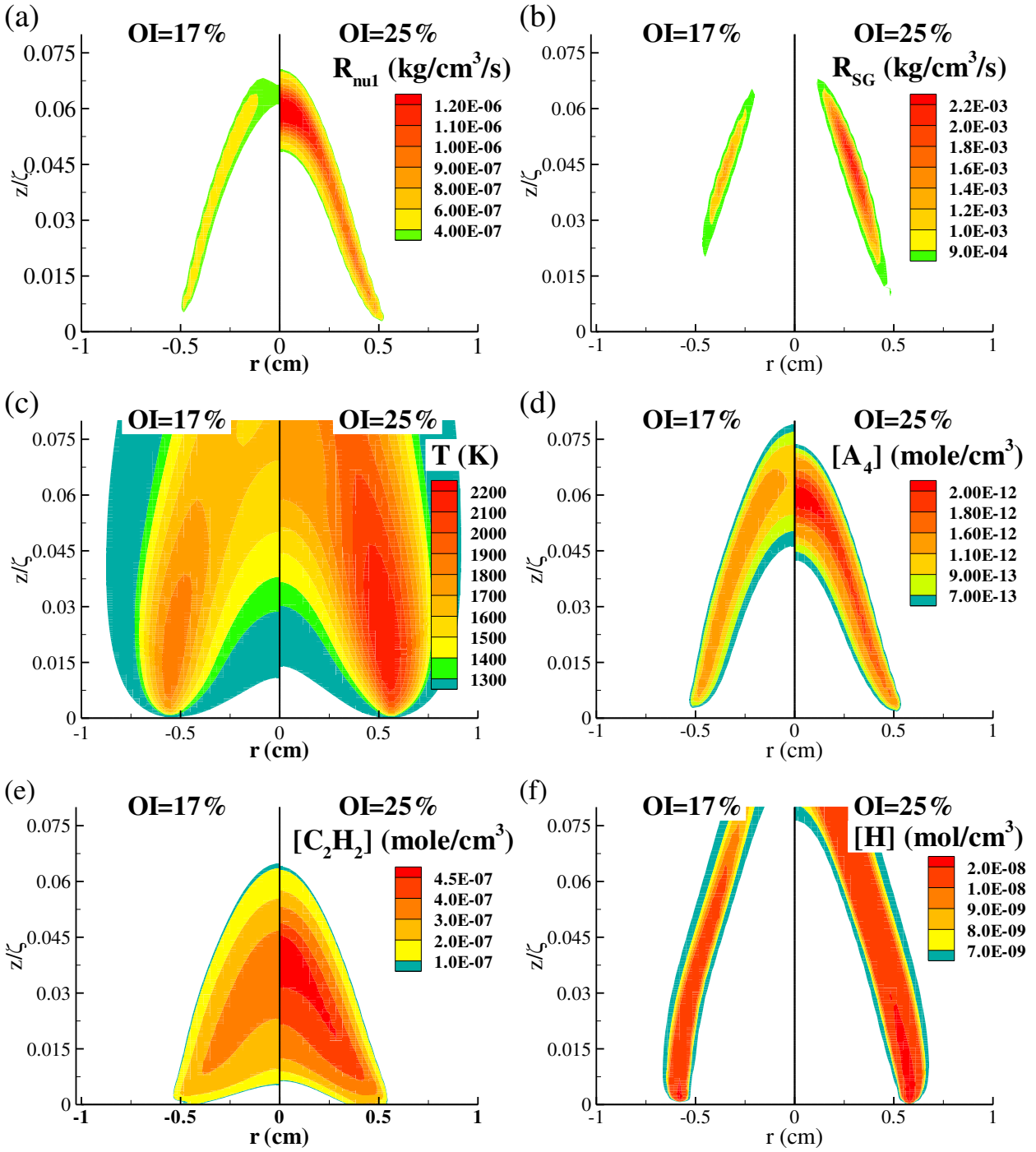

Figure 3-5: Predicted distributions of: a) nucleation rates, b) surface growth rate, c) temperature, d) molar concentration of pyrene, e) molar concentration of acetylene, and f) molar concentration of hydrogen radical for OIs of 17% and 25%.

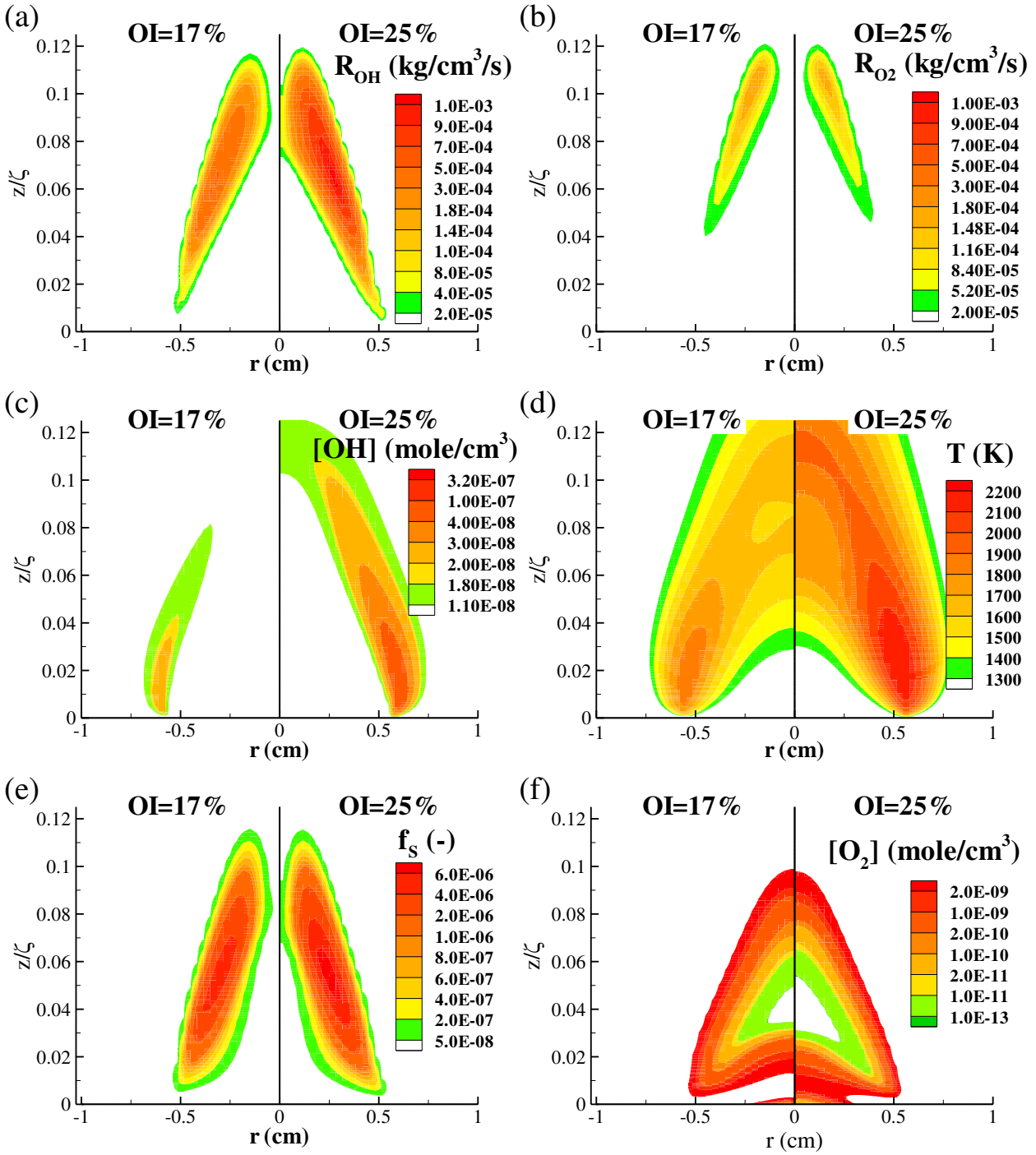

Figure 3-6: Predicted distributions of: a) soot oxidation rates by OH, b) soot oxidation rate by O2, c) molar concentration of OH, d) temperature, e) soot volume fraction and f) molar concentration of O_2.

3.4. Conclusions

The performance of a PAH-based two-equation soot model, derived from the ABF theory, to predict the influence of the OI on soot production in axisymmetric co-flow ethylene diffusion flames is assessed. Model predictions are compared with experimental results for OIs in the range between 17% and 33%. The following conclusions can be drawn: 1) Model results are on the whole in satisfactory agreement with the experimental data for flame structures, radial profiles of soot volume fraction, and the integrated soot volume fractions. Nevertheless, the sharp decrease in rate of increase of the maximum soot volume fraction with OI, observed experimentally for OIs greater than 25%, is not well reproduced. 2) The present soot model provides a better description of the influence of OI on the soot production process than the semi-empirical acetylene-based soot model tested previously. 3) The increases in the nucleation and surface growth rates with OI results from an increase in both temperature and soot precursor concentrations.

4. Applications to Laminar Boundary Layer Diffusion Flames

The objective of this chapter is to provide a better understanding of soot production and flame quenching at the trailing edge in Laminar Boundary Layer Diffusion Flames (LBLDFs) in microgravity. In order to accomplish this task, the experiments performed by Fuentes during his PhD thesis (Fuentes 2006) will be analyzed on the basis of a dimensionless analysis. In a second part, the numerical model will be applied to complete the discussion. Finally the effects of the use of simplified radiation models on both soot production and flame structure will be investigated.

4.1. Experimental Data Analysis

4.1.1. Experimental Set-Up

4.1.1.1. Configuration

To reduce the effects of earth's gravity, experimental microgravity flames were conducted in parabolic flights on board of A300 Zero-G airplane. Parabolic flights provide a 22 s long microgravity period, which allows steady-state conditions to be reached (Vietoris et al. 2000). The limitations imposed by low quality microgravity and g-jitter have been analyzed in detail by Rouvreau et al (Rouvreau et al. 2005) concluding that perturbations similar to those typically observed during parabolic flights showed a minor influence on the flame geometry and can be neglected when analyzing data . The experimental set-up and the methodology are described in detail by Fuentes et al. (Fuentes, Legros, Claverie, et al. 2007) and Legros et al. (Legros et al. 2009), so a brief explanation is presented here. The laminar boundary layer diffusion flame is established inside a 50 L stainless steel combustion chamber. The volume of the chamber is sufficiently large to keep the flame free from wall effects and to accomplish for safety requirements in microgravity facilities (Fuentes, Legros, Claverie, et al. 2007; Fuentes, Legros, El-Rabii, et al. 2007). The pressure is kept at atmospheric value by means of a controlled mass

flow-meter placed at the exhaust of the duct. Ethylene is chosen as fuel for its well characterized sooting behavior. It is injected via a mass flow controller through a square porous which has a 50×50 mm^2 effective section of injection. The oxidizer flow is introduced in the combustion chamber via mass flow controllers through a settling chamber and honeycomb plates. The oxidizer creates a boundary layer flow parallel to the burner surface where the diffusion flame is established. The oxidizer consists in mixtures of O_2 and N_2. Relevant burner dimensions and configuration of diagnostic equipment can be seen in Figure 4-1.

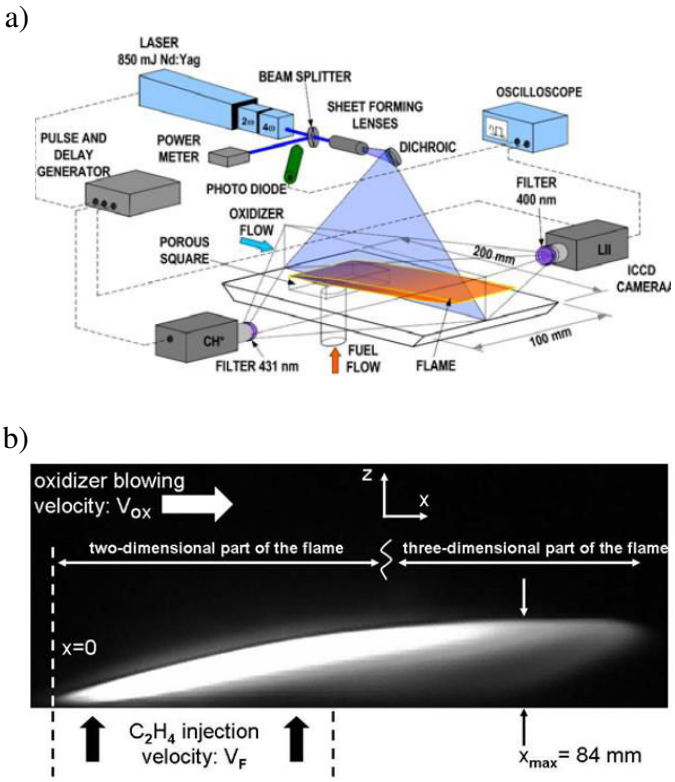

Figure 4-1: a) Schematic of experimental apparatus (Fuentes, Legros, Claverie, et al. 2007); b) Greyscale side view of the visible flame for V_{ox}=150 mm/s and V_F=3 mm/s (Legros et al. 2005).

4.1.1.2. Parameters

Experiments were conducted to study the effects of the oxygen index (OI), defined as the volume fraction of oxygen in the oxidizer stream, the oxidizer velocity (U_{ox}) and the fuel injection velocity (V_F) on flame geometry, soot production and flame quenching processes. Three values of the oxygen index (OI), namely 21%, 35% and 50%, five values of oxidizer velocity of

125, 150, 200, 250, and 300 mm/s, and three values of the fuel injection velocity of 3, 4 and 5 mm/s were considered. The fuel injection velocity can be related in a certain way to the pyrolysis mass rate. Thus, a data set of 45 flames is available and will be analyzed in present chapter in order to provide some insights on the physical behavior of microgravity laminar boundary layer diffusion flames (μ-LBLDFs).

Flame geometry is characterized by the stand-off distance and the flame length. The first indicates, at each location along the plate, the vertical position of the flame sheet where fuel and oxygen reach their stoichiometric conditions. The latter is measured as the distance along the x-coordinate from the burner leading edge to the flame tip. Flame length and stand-off distances are determined from the emission of hydroxyl radical (OH*) which can be seen as representative of the reaction zone.

4.1.1.3. Diagnostics

Laser Induced Incandescence (LII) system allows heating the soot particles up to their incandescence temperature, then its radiative emission is measured by an appropriate device. In the experiments of Fuentes (Fuentes et al. 2006), a Nd:YAG laser beam (see Figure 4-1a), emitting at 266 nm with a nominal energy of 120 mJ, was used to create a laser sheet in the burner symmetry plane. To achieve the LII at 266 nm, an energy flux threshold of 0.03 J/cm^2 is required (Shaddix and Smyth 1996; Vander Wal, Jensen, and Choi 1997). The mean laser energy flux computed was of 0.1 J/cm^2 which is above of aforementioned threshold.

Images were collected in the direction orthogonal to the laser sheet using an intensified charge couple device (ICCD) camera, providing 16-bit black-and-white measurements on a 1024×1024 pixel matrix. Different approaches exist for detection (Santoro and Shaddix 2002) but for present data the method used is based on the recommendations of Van der Wal ans co-worlers (Vander Wal, Jensen, and Choi 1997). Before to impact the CCD sensor, the photons that come from incandescence pass through an interference filter with peak transmission wavelength at 400 nm (60 nm FWHM) mounted in front of the ICCD camera to avoid the most common interference sources and then by a lens chosen to obtain the maximum resolution. The most experiments were carried out employing an f/0.95 25 mm focal length lens. The camera resolution yields a 0.22×0.22 mm^2 per pixel resolution.

Using a pulse timing generator (PTG), the collection of LII signals started 80 ns after the laser pulse was detected by a photodiode. This delay allows discrimination of the LII signal from soot particles with respect to the laser-induced fluorescence (LIF) signal from polycyclic aromatic hydrocarbons (PAH) (Vander Wal, Jensen, and Choi 1997). Both phenomena are simultaneously induced by the 266 nm excitation, but the latter has a much faster decay rate. The intensifier gate width was 50 ns, which gives significant LII intensity levels 80 ns after the laser pulse. For these non-buoyant diffusion flames, soot particle diameter is expected to be poly-dispersed, and consequently for these conditions the signal intensity only weakly influenced by particle diameter (Vander Wal, Jensen, and Choi 1997).

Another ICCD camera was devoted was devoted to OH^* emission. This camera recorded one side-view frame between each laser pulse with an intensifier gate width of 50 ns. This camera was mounted with a narrow band filter centered at 310 nm (12 nm FWHM). A f/1.8 45 mm focal length lens was mounted in the camera to improve the resolution. OH* is an important intermediate species in any flame involving oxygen and hydrogen. It appears in the beginning of the kinetic reaction chain scheme, directly by means of reaction between CH* and O_2. For this reason the emission intensity from OH* (but also from CH^* and C_2^*) in hydrocarbon flames can be used to observe the location of the primary combustion region [Kojima 2000]. Also, Marchese et al. [Marchese1996] suggested that OH* distribution should yield a rational indication of flame-front position, since the maximum OH* emission is near the maximum flame temperature. These excited radicals return to ground-state either through collisional quenching or through spontaneous fluorescence, whose $A^2\Delta \rightarrow X^2\Pi$ transition occurs at 310 nm. Finally, as OH* field covers the maximum temperature zone so that OH* chemiluminescence measurements can be directly related to the burning rate of the primary fuel (e.g., ethylene here) (Fuentes 2006; Walsh et al. 1998).

4.1.2. Theoretical analysis

The aim of this section is to provide tools based on non-dimensionless analysis to explain the experimental results. First, the relevant non-dimensionless parameters of the problem are derived. Secondly, a scaling analysis, based on these parameters and simplified assumptions, is given. This scaling analysis does not consider the flame quenching at the trailing edge and should be invalidated by the experiments.

4.1.2.1. Dimensionless variables

Figure 4-2 shows, in a scheme of the configuration studied, the characteristic parameters used to perform the non-dimensionalization process. The governing differential conservation equations can be made dimensionless by introducing the following dimensionless variables.

$$u^* = \frac{u}{U_{ox}}; v^* = \frac{v}{V_F}; x^* = \frac{x}{L_f}; y^* = \frac{y}{\delta_f}; \rho^* = \frac{\rho}{\rho_\infty}; D^* = \frac{D}{D_\infty}; \mu^* = \frac{\mu}{\mu_\infty}; T^* = \frac{(T - T_\infty)}{(T_f - T_\infty)}$$

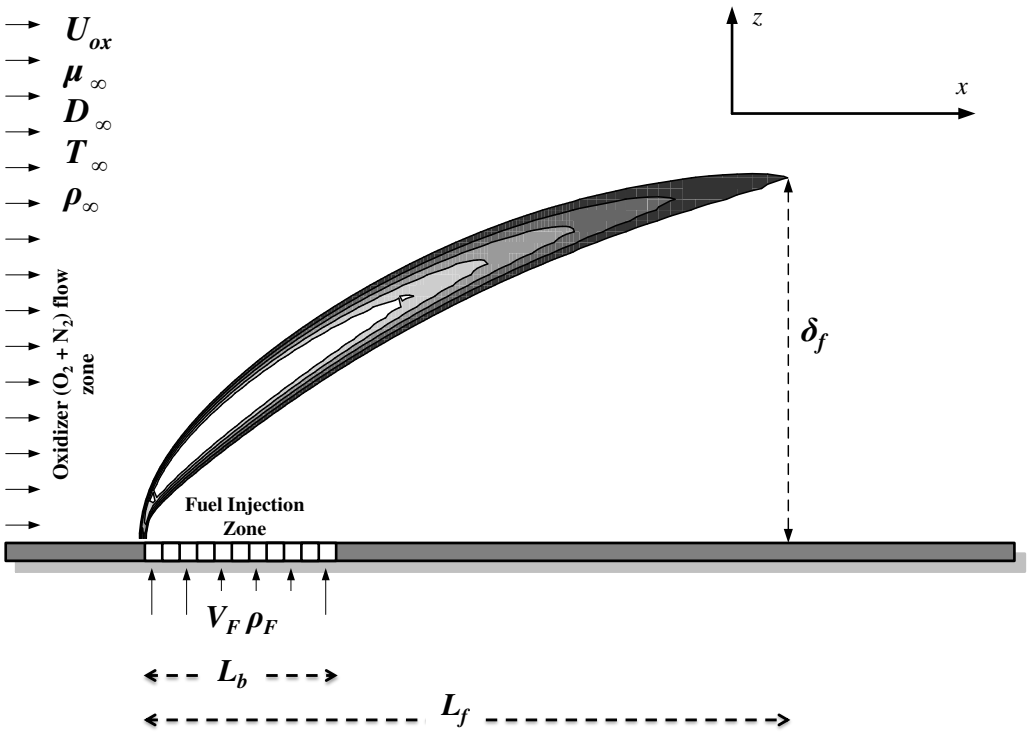

Figure 4-2: Definition of the characteristic quantities.

Where L_f and U_{ox}, the flame length and the oxidizer velocity, are taken as characteristic length scale and velocity scale in the *x*-direction, respectively. Whereas δ_f and V_F the stand-off distance at the flame length and the fuel velocity, are selected as characteristic length scale and velocity scale in the *z*-direction. T_f is a characteristic flame temperature which can be taken as

the maximum temperature and L_b is the characteristic length of burner (5 cm), In turn, ρ_∞, μ_∞, D_∞ and T_∞ are the density, the dynamic viscosity, de diffusion coefficient and the temperature of oxidizer stream, respectively. Finally, ρ_F is the density of fuel flow, respectively.

The time scale of convection along the plate, defined by $t_{res} = L_f / U_{ox}$, is chosen as characteristic time scale or residence time. For sake of simplification the oxidation of fuel into water vapor and carbon dioxide is simply modeled by a single-step reaction with a reaction rate defined by a second-order Arrhenius law:

$$\dot{\omega} = A\rho Y_F Y_{ox} e^{[-E/RT]} \tag{4.1}$$

Set $\sigma \equiv T_f - T = \left(T_f - T_\infty\right)\left(1 - T^*\right)$ which leads to:

$$T = T_f - \sigma = T_f \left(1 - \frac{\sigma}{T_f}\right) \tag{4.2}$$

In regions where the reaction rate is significant, the ratio σ / T_f is generally small. As a consequence the exponential part of equation (4.1) can be developed as follows (Kuo 1986):

$$e^{\left[-E/RT\right]} = e^{\left[-\frac{E}{RT_f\left(1-\sigma/T_f\right)}\right]} \approx e^{\left[-\frac{E}{RT_f}\left(1+\frac{\sigma}{T_f}\right)\right]} = e^{\left[-\frac{E}{RT_f}\right]} e^{\left[-\frac{E\sigma}{RT_f^2}\right]} \tag{4.3}$$

Introducing this last expression in the reaction rate of equation (4.1) we obtain:

$$\dot{\omega} = A\rho Y_F Y_{ox} e^{\left(-\frac{E}{RT_f}\right)} \dot{\omega}^* \tag{4.4}$$

With $\dot{\omega}^* = e^{\left(-\frac{E\sigma}{RT_f^2}\right)}$

The divergence of the radiative flux was computed by assuming an optically-thin medium and, for mathematical convenience, its expression is also modeled by using an Arrhenius law (Chao, Law, and T'ien 1991; Sohrab, Liñán, and Williams 1982; Q. Wang and Chao 2011):

$$\vec{\nabla}\cdot\vec{\dot{q}}'' \approx B_R e^{(-E_R/T)} \tag{4.5}$$

The same development as for the reaction rate is made to re-express this term:

$$\vec{\nabla}\cdot\vec{\dot{q}}'' \approx \mathrm{B_R e}^{\left(-E_R/T_f\right)}\dot{q}^* \tag{4.6}$$

With $\dot{q}^* = e^{\left(-\frac{E_R\sigma}{T_f^2}\right)}$

Thus, the dimensionless form of governing differential conservation equations is:

Mass

$$\frac{\partial \rho^* u^*}{\partial x^*} + \underbrace{\left(\frac{V_F}{\delta_f}\frac{L_f}{U_{ox}}\right)}_{\Pi_1}\frac{\partial \rho^* v^*}{\partial z^*} = 0 \tag{4.7}$$

x-momentum

$$\rho^* u^* \frac{\partial u^*}{\partial x^*} + \underbrace{\left(\frac{L_f}{U_{ox}}\frac{V_F}{\delta_f}\right)}_{\Pi_1} + \rho^* v^* \frac{\partial u^*}{\partial z^*} = -\underbrace{\left(\frac{P_\infty}{\rho_\infty U_{ox}^2}\right)}_{\Pi_2}\frac{\partial P^*}{\partial x^*} + \underbrace{\left(\frac{\mu_\infty}{\rho_\infty L_f U_{ox}}\right)}_{\Pi_3}\frac{\partial}{\partial x^*}\left(\mu^*\frac{\partial u^*}{\partial x^*}\right) + \underbrace{\left(\frac{\mu_\infty}{\rho_\infty \delta_f^2}\frac{L_f}{U_{ox}}\right)}_{\Pi_4}\frac{\partial}{\partial z^*}\left(\mu^*\frac{\partial u^*}{\partial z^*}\right) \tag{4.8}$$

z-mometum

$$\rho^* u^* \frac{\partial v^*}{\partial x^*} + \underbrace{\left(\frac{L_f}{U_{ox}}\frac{V_F}{\delta_f}\right)}_{\Pi_1}\rho^* v^* \frac{\partial v^*}{\partial z^*} = -\underbrace{\left(\frac{P_\infty L_f}{\rho_\infty U_{ox} V_F \delta_f}\right)}_{\Pi_5}\frac{\partial P^*}{\partial x^*} + \underbrace{\left(\frac{\mu_\infty}{\rho_\infty L_f U_{ox}}\right)}_{\Pi_3}\frac{\partial}{\partial x^*}\left(\mu^*\frac{\partial v^*}{\partial x^*}\right) + \underbrace{\left(\frac{\mu_\infty}{\rho_\infty \delta_f^2}\frac{L_f}{U_{ox}}\right)}_{\Pi_4}\frac{\partial}{\partial z^*}\left(\mu^*\frac{\partial v^*}{\partial z^*}\right) \tag{4.9}$$

Fuel mass fraction

$$\rho^* u^* \frac{\partial Y_F}{\partial x^*} + \underbrace{\left(\frac{L_f}{U_{ox}}\frac{V_F}{\delta_f}\right)}_{\Pi_1}\rho^* v^* \frac{\partial Y_F}{\partial z^*} = \underbrace{\left(\frac{D_\infty}{L_f^2}\frac{L_f}{U_{ox}}\right)}_{\Pi_6}\frac{\partial}{\partial x^*}\left(\rho^* D^* \frac{\partial Y_F}{\partial x^*}\right) + \underbrace{\left(\frac{D_\infty}{\delta_f^2}\frac{L_f}{U_{ox}}\right)}_{\Pi_7}\frac{\partial}{\partial z^*}\left(\rho^* D^* \frac{\partial v^*}{\partial z^*}\right) + \underbrace{\left(\mathrm{A}\,\mathrm{e}^{\left(-E/RT_f\right)}\frac{L_f}{U_{ox}}\right)}_{\Pi_8}\omega^* \tag{4.10}$$

Energy

$$\rho^* u^* c_p^* \frac{\partial Y_F}{\partial x^*} + \underbrace{\left(\frac{L_f}{U_{ox}}\frac{V_F}{\delta_f}\right)}_{\Pi_1}\rho^* v^* c_p^* \frac{\partial Y_F}{\partial z^*} = \underbrace{\left(\frac{\lambda_\infty}{c_{p,\infty}L_f^2}\frac{L_f}{U_{ox}}\right)}_{\Pi_9}\frac{\partial}{\partial x^*}\left(\rho^* \lambda^* \frac{\partial Y_F}{\partial x^*}\right) + \underbrace{\left(\frac{\lambda_\infty}{c_{p,\infty}\delta_f^2}\frac{L_f}{U_{ox}}\right)}_{\Pi_{10}}\frac{\partial}{\partial z^*}\left(\rho^* \lambda^* \frac{\partial v^*}{\partial z^*}\right) + \underbrace{\left(\mathrm{A}\mathrm{Y}_\mathrm{F} Y_{ox}\,\mathrm{e}^{\left(-E/RT_f\right)}\frac{L_f}{U_{ox}}\right)}_{\Pi_8}\underbrace{\left(\frac{\Delta h_c}{c_{p,\infty}\Delta T}\right)}_{\Pi_{11}}\omega^* + \underbrace{\left(\frac{B_R\,\mathrm{e}^{\left(-E_R/T_f\right)}}{c_{p,\infty}\Delta T}\frac{L_f}{U_{ox}}\right)}_{\Pi_{12}}q^* \tag{4.11}$$

4.1.2.2. Dimensionless Terms

$\Pi_1 = \frac{L_f}{U_{ox}}\frac{V_F}{\delta_f}$	$\frac{\text{residence time}}{\text{characteristic time scale of convection in the y-direction}}$
$\Pi_2 = \frac{\mathrm{P}_\infty}{\rho_\infty U_{ox}^2}$	
$\Pi_3 = \frac{\mu_\infty}{\rho_\infty L_f^2}\frac{L_f}{U_{ox}} = \frac{\mu_\infty}{\rho_\infty U_{ox} L_f} = \frac{1}{\mathrm{Re}}$	$\frac{\text{residence time}}{\text{charactic time for viscous effects in the } x\text{-direction}}$
$\Pi_4 = \frac{\mu_\infty}{\rho_\infty \delta_f^2}\frac{L_f}{U_{ox}}$	$\frac{\text{residence time}}{\text{charactic time for viscous effects in the } z\text{-direction}}$
$\Pi_5 = \frac{P_\infty L_f}{\rho_\infty U_{ox} V_F \delta_f}$	
$\Pi_6 = \frac{D_\infty}{L_f^2}\frac{L_f}{U_{ox}}$	$\frac{\text{residence time}}{\text{characteristic time for diffusion of species in } x\text{-direction}}$
$\Pi_7 = \frac{D_\infty}{\delta_f^2}\frac{L_f}{U_{ox}}$	$\frac{\text{residence time}}{\text{characteristic time for diffusion of species in } z\text{-direction}}$

$\Pi_8 = Ae^{\left(-E/RT_f\right)} \dfrac{L_f}{U_{ox}}$	$\dfrac{\text{residence time}}{\text{chemical time}} = Da$
$\Pi_9 = \dfrac{\lambda_\infty}{c_{p,\infty} L_f^2} \dfrac{L_f}{U_{ox}}$	$\dfrac{\text{residence time}}{\text{characteristic time for diffusion of heat in } x\text{-direction}}$
$\Pi_{10} = \dfrac{\lambda_\infty}{c_{p,\infty} \delta_f^2} \dfrac{L_f}{U_{ox}}$	$\dfrac{\text{residence time}}{\text{characteristic time for diffusion of heat in } z\text{-direction}}$
$\Pi_{11} = \dfrac{\Delta h_c}{c_{p,\infty} \Delta T}$	normalized heat of combustion
$\Pi_{12} = \dfrac{B_R \exp\left(-E_R/T_f\right)}{c_{p,\infty} \Delta T} \dfrac{L_f}{U_{ox}}$	$\dfrac{\text{residence time}}{\text{characteristic time for radiative loss}}$

In the case where Prandtl $\left(Pr = \mu_\infty c_{p,\infty} / \lambda_\infty\right)$ and Schmidt $\left(Sc = \mu_\infty / \rho_\infty D_\infty\right)$ can be assumed to be constant and equal to 1. Long residence times and, as a consequence, large Damkhöler numbers are observed in the present flames. The radiative quenching at the leading edge implies also that the residence time becomes of the same order than the characteristic time for radiative loss (Lautenberger et al. 2005).

4.1.2.3. Scaling analysis

The present analysis applies in the case where all the fuel is burnt. It is based on the following assumptions:

a) The flow is bi-dimensional.

b) The combustion is complete, i.e. all the fuel is oxidized at the flame tip.

c) The chemical reaction is assumed to be a one-step reaction. $F + SO_x \longrightarrow (1+S)\,\text{Products}$ where S is the mass stoichiometric oxidizer to fuel ratio.

d) Prandtl and Schmidt numbers are assumed to be equal to 1.

The mass conservation can be expressed as follows:

$$\rho_\infty U_{OX}\delta_f + \rho_F V_F L_b \approx \rho_\infty U_{OX}\delta_f \propto (1+S)\rho_F V_F L_b = (1+S)\dot{m}_F^{'} \tag{4.12}$$

where ρ_∞, is the density of oxidizer stream, ρ_F is the density of fuel, L_b is the characteristic length of burner (5 cm) and $\dot{m}_F^{'}$ is the fuel mass flow rate . Equation (4.12) can be simply written as:

$$\rho_\infty U_{ox}\delta_f \propto (1+S)\rho_F V_F L_b \tag{4.13}$$

The stand-off distance (is assumed to be controlled by the diffusion process. This implies that the residence time is of the same order as the characteristic diffusion time in *z*-direction. As a consequence, Π_4, Π_7 and Π_{10} are approximately equal to 1, which leads to:

$$\delta_f \propto \left(\nu_\infty \frac{L_f}{U_{ox}}\right)^{1/2} \tag{4.14}$$

Introducing equation (4.13) into equation (4.12) leads to the following expression for the flame length:

$$L_f = \frac{(1+S)^2 \rho_F^2 V_F^2 L_b^2}{\mu_\infty U_{ox}} \tag{4.15}$$

This equation shows that the flame length increases with the fuel velocity and the mass stoichiometric oxidizer to fuel ratio. This latter situation occurs when the amount of oxygen in the oxidizer stream decreases. Equation (4.15) shows also that the flame length is shortened as the oxidizer velocity increases. The residence time is then defined by:

$$t_{res} \equiv \frac{L_f}{U_{ox}} \propto \frac{(1+S)^2 \rho_F^2 V_F^2 L_b^2}{\mu_\infty U_{ox}^2} \tag{4.16}$$

It follows the same trends as the flame length, increasing with the fuel velocity and the mass stoichiometric oxidizer to fuel ratio and decreasing as the oxidizer velocity increases.
In turn, the characteristic soot formation rate is then given by:

$$\frac{D\left(\rho Y_s\right)}{Dt} \approx \frac{\rho_\infty Y_{S,max}}{t_{res}} \propto \frac{\rho_\infty}{\tau_{f,S}} \tag{4.17}$$

Leading to:

$$Y_{S,max} \propto \frac{t_{res}}{\tau_{f,S}} = \frac{\left(1+S\right)^2 \rho_F^2 V_F^2 L_b^2}{\mu_\infty U_{ox}^2 \tau_{f,S}} \tag{4.18}$$

The maximum soot volume fraction is deduced from the previous equation:

$$f_{_{S,max}} \propto \frac{\rho_\infty Y_{S,max}}{\rho_S} = \frac{\rho_\infty \left(1+S\right)^2 \rho_F^2 V_F^2 L_b^2}{\rho_S \mu_\infty U_{ox}^2 \tau_{f,S}} \tag{4.19}$$

The characteristic time scale for soot formation$\left(\tau_{f,S}\right)$, is expected to be proportional to the smoke point flame length. As an example, it is expected to become shorter as the pressure increases (Kim et al. 2004). It is also expected to depend on the oxygen index (Fuentes et al. 2013; Glassman and Yaccarino 1980). For a given oxygen index, the evolution of the maximum soot volume fraction follows that of the residence time. Eventually the maximum integrated soot volume fraction is expressed as:

$$F_{S,max} \propto f_{S,max}\delta_f = \frac{\rho_\infty \left(1+S\right)^3 \rho_F^3 V_F^3 L_b^3}{\rho_S \mu_\infty U_{ox}^3 \tau_{f,S}} \tag{4.20}$$

4.1.3. Results

4.1.3.1. Stand-off distance

The stand-off distance is determined as the vertical location of the maximum value of the captured emission of OH^*. To evidence the effects of U_{OX} and V_F on OH^* peaks based stand-off distance, Figure 4-3 shows the evolution of vertical location of OH^* emission peaks as a function of the distance along the plate. Data has been grouped to display the evolution of stand-off distance with U_{OX} and V_F. Same symbols have been used for a given value of V_F and same color has been used for a given value of U_{OX}.

The diagrams a, b, and c are relative to OI of 21%, 35% and 50%, respectively. As expected, the flame SOD increases with the distance along the plate. For a fixed x-location, it appears clearly that SOD increases with the V_F and as the U_{ox} decreases. In addition, the results in Figure 4-3 show that the SOD is more sensitive to variation in the U_{ox} than that of the V_F.

Figure 4-4 shows the evolution of SOD along the plate for an OI of 50% and different couples of U_{ox} and V_F ratios of 300 mm/s and 3mm/s, 200 mm/s and 4mm/s and 125 mm/s and 5mm/s. The same trends are observed for the other OI. For the smaller ratio of U_{ox}/V_F=25 (U_{ox}=125 mm/s and V_F=5 mm/s) the stand-off distance is the higher. As expected from the LBL theory (Emmons 1956) its evolution along the plate is controlled by the diffusion process in the z-direction. Π_4, Π_6 and Π_{10} are then of the order of 1 and δ_f scales approximately with $x^{1/2}$. At x equal about to 5 cm, which corresponds to the location of the burner trailing edge, the SOD ceases to evolve with $x^{1/2}$. This change in slope is attributed to the appearance of 3D effects. As the ratio U_{ox}/V_F increases to 50 (U_{ox}=200 mm/s and V_F=4 mm/s) the SOD moves closer to the plate. At the vicinity of the burner leading edge, where the SOD is the closest to the plate, it can be observed that the SOD evolves with x. This shows that close to the burner leading edge the SOD is no longer controlled by the diffusion process but its evolution becomes governed by the convection in the z-direction ($\Pi_1 \sim 1$). As the distance along the plate increases, the SOD increases and the influence of the V_F is reduced. The evolution of the SOD becomes then controlled by the diffusion processes in the z-direction and the SOD scales with $x^{1/2}$. Finally, for U_{ox}/V_F=25, a third regime appears at the burner trailing edge likely owing to the appearance of

3D effects. These three regimes are also observed as the ratio of U_{ox} to V_F is increased further to 100, but the distance along the plate over which the convection-controlled regime prevailed becomes longer.

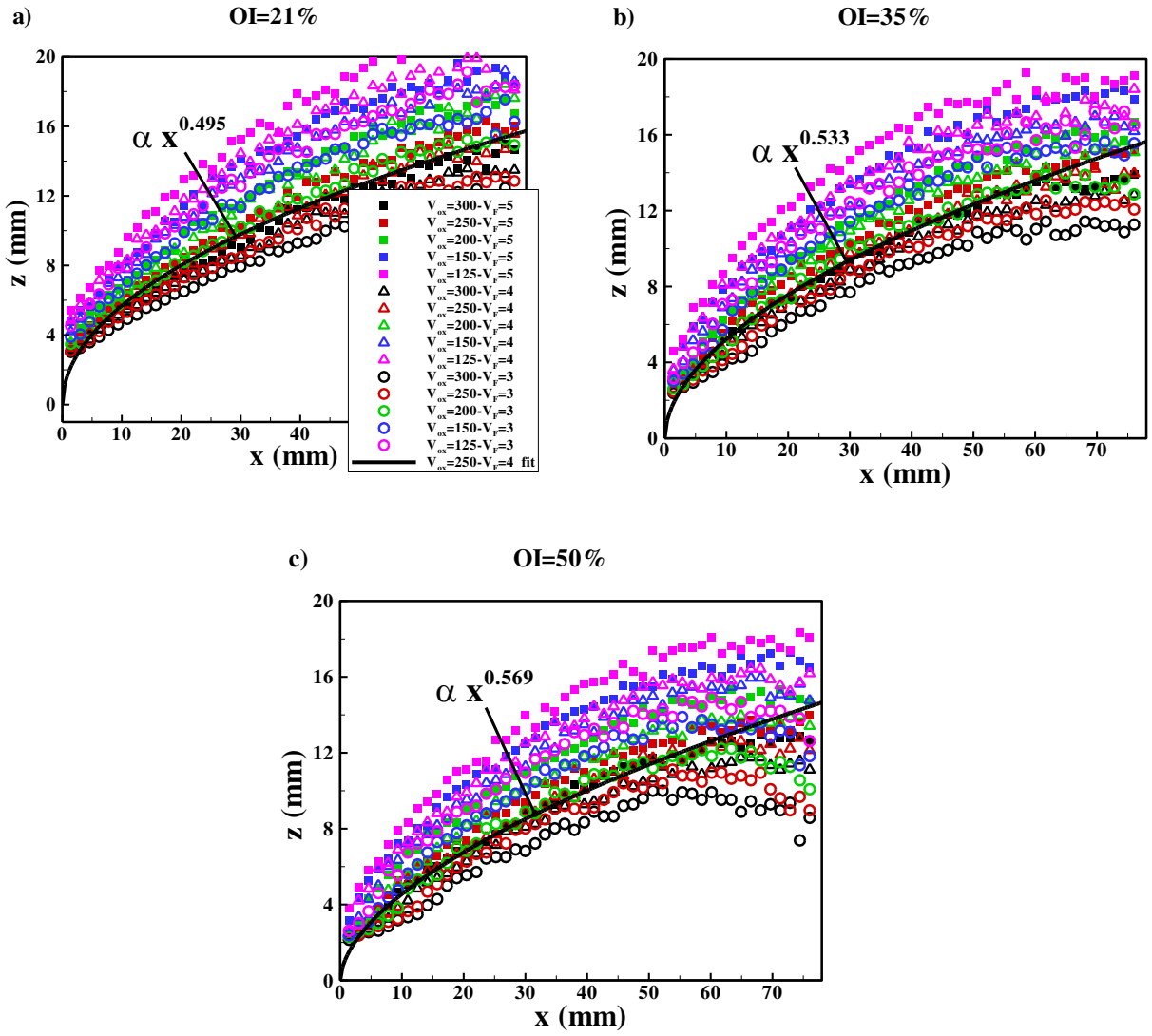

Figure 4-3: Shows the effects of U_{ox} and V_F on stand-off distance for the three oxygen index studied a) 21, b) 35 and c) 50%.

The analysis of Figure 4-4 has revealed that the SOD evolves along the plate according to three regimes: close to the trailing edge of the burner, characteristic convective time in the *z*-direction is of the same order than the local residence time $\left(xV_F/\delta(x)U_{ox} \approx 1\right)$ and $\delta(x)$ scales

with x. The length of this region increases with the ratio U_{ox}/V_F. As the distance along the plate increases the influence of the convection in the z-direction is reduced and that of the diffusion in the z-direction becomes prevailing. A second regime appears where the characteristic diffusion time in the z-direction becomes of the same order than the local residence time $\nu_\infty x/\delta^2(x)U_{ox} \approx 1$ and $\delta(x)$ scales with $x^{1/2}$. This scaling ceases to be valid after the burner trailing edge as 3D effects becomes significant.

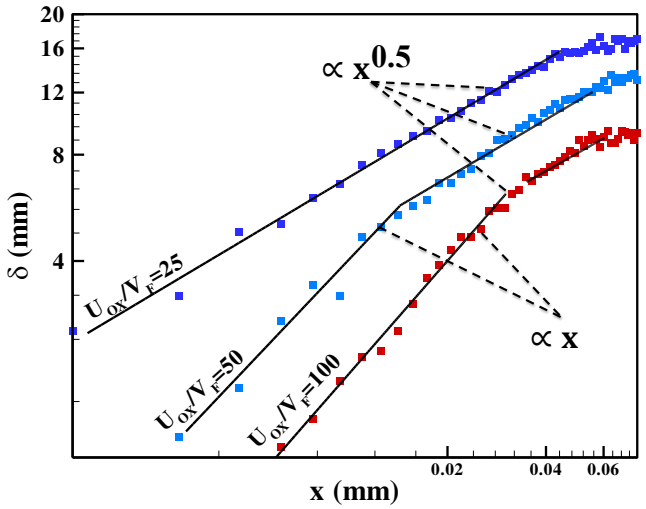

Figure 4-4: Evolution of the stand-off distance as a function of the distance along the plate for three different couples of oxidizer and fuel velocities of 300 mm/s and 3mm/s (red symbols), 200 mm/s and 4 mm/s (green symbols) and 125 mm/s and 5 mm/s (blue symbols), leading to ratios between U_{ox} and V_F of 100, 50, and 25, respectively.

An empirical correlation of the form $\delta(x)/V_F^n = f(\nu_\infty x/U_{ox})$ has been found, assuming that the diffusion controlled regime, prevails over the entire plate. Figure 4-5 shows that plotting $\delta(x)/V_F^n$ as a function of $\nu_\infty x/U_{ox}$ with n=0.4 allows, for each OI, roughly collapsing the data for different fuel injection and oxidizer velocities on a single curve. The best fit indicates that $\delta(x)/V_F^{0.4} = \text{const} \times (\nu_\infty x/U_{ox})^m$ with m ≈ 1/2, the value of this exponent being consistent with the assumption that the SOD is governed by the diffusion regime. As expected from the analysis developed previously, the quality of the correlation deteriorates slightly in the vicinity of the burner leading edge since the SOD in this region is rather governed by the convective regime. The location of the burner trailing edge, which corresponds to the end of validity of the fit, clearly appears in Figure 4-5. In addition, the equations of the fit and the curves in Figure 4-5a, b

and c suggest that the effects of the OI (mass stoichiometric air to fuel mass ratio) are rather weak.

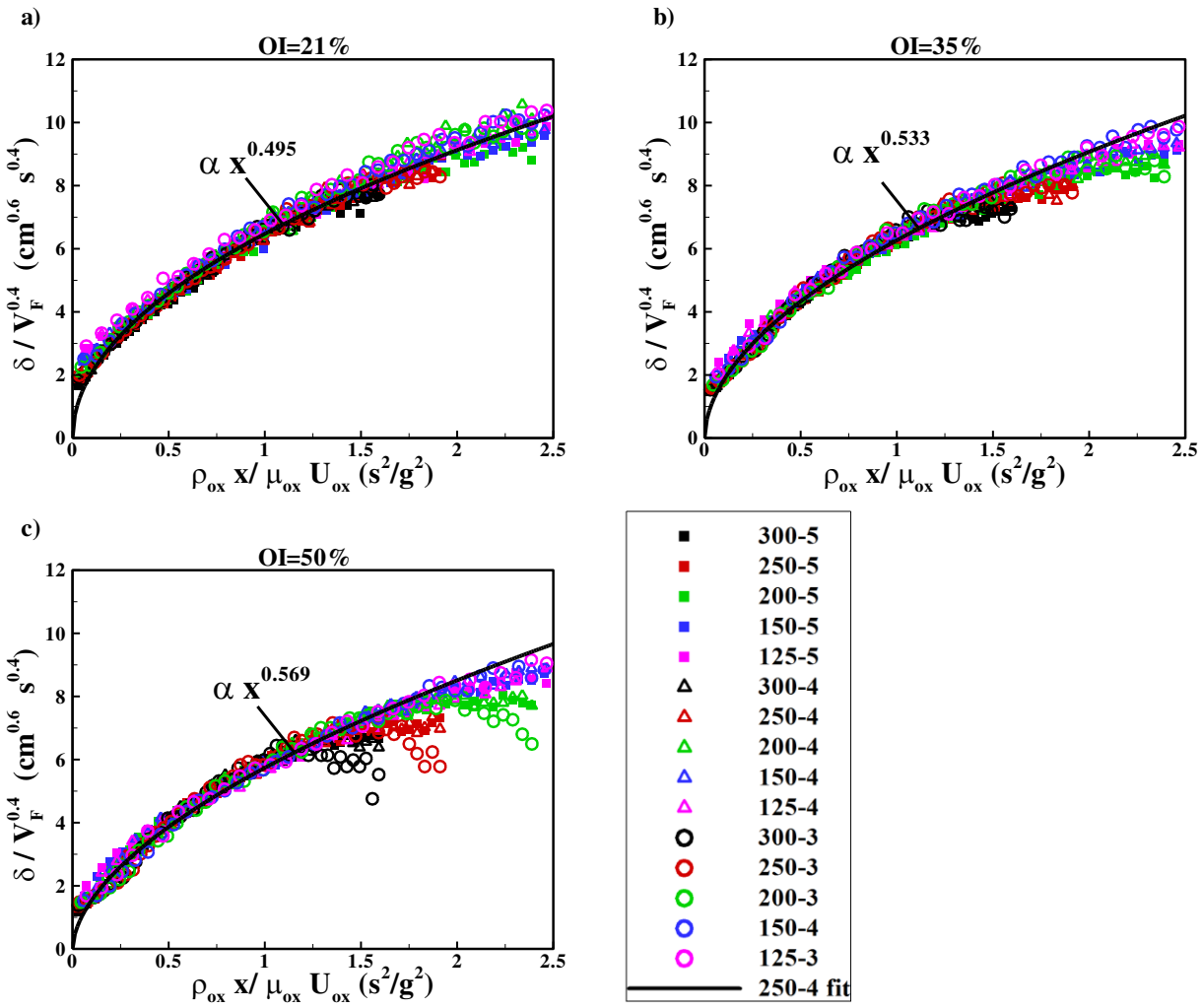

Figure 4-5: Parameter ($\delta/V_F^{0.4}$) as a function of ($\rho_\infty x/\mu_\infty U_{OX}$) for a) OI=21%, b) OI=35%, and c) OI=50%.

4.1.3.2. Flame length

Figure 4-6 shows the evolution of the L_f as a function of the U_{ox} for the different V_F and OI. It appears that, on the whole, the L_f increases with the U_{ox}. The rate of reduction seems to be less pronounced for an OI of 50% and fuel velocities of 4 mm/s and 5 mm/s. The analysis, developed in the previous section and based on the assumption that fuel is fully oxidized at the flame tip, predicts that the L_f decreases as the U_{ox} increases. The present results show that this assumption does not hold for the present flames which exhibit radiative quenching processes at

the flame trailing edge (Bhattacharjee and Altenkirch 1991; Fuentes, Legros, Claverie, et al. 2007; Legros et al. 2009). In this case the residence time is sufficiently long and the radiative loss is sufficiently high to cool down the gases below a temperature at which oxidation reactions cannot occur. Theoretical analysis suggested that this temperature is of the order of 1100 K and is lower than the extinction temperature observed in flame extinction at low Damkhöler number (Santa et al. 2007). This phenomenon can be explained by assuming that the residence time becomes of the same order of magnitude as the characteristic time for radiative loss ($\Pi_{10} \approx 1$). This implies that:

$$\frac{L_f}{U_{ox}} \approx t_{rad} \tag{4.21}$$

The characteristic time scale of radiative loss depends primarily of soot volume fraction and temperature which are themselves influenced by U_{ox}, V_F and OI.

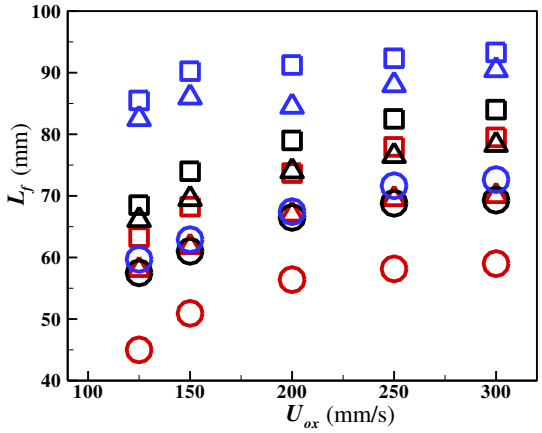

Figure 4-6: Effects of oxidizer velocity, fuel velocity and oxygen index on flame length. Symbol nomenclature is displayed as: (□) for V_F=5, (Δ) for V_F=4 and (○) for V_F=3 mm/s. Red, black and blue symbols are used for OI 50, 35 and 21, respectively.

Qualitative and quantitative understandings of the evolution of this time scale with the different parameters of the problem would require measurements of radiant fraction that unfortunately are not available. Varying the OI modifies significantly the temperature of the system, the adiabatic temperature increasing from 2254 K for an OI of 21% to 3350 K for an OI of 35%. This is then expected to influence strongly the radiative loss. The evolution of the temperature is expected to be less sensitive to variations of U_{ox} and V_F. For given OI, V_F and for

slight variation of U_{ox}, the integrated soot volume fraction (see the variation of the integrated soot volume fraction for U_{ox} increasing from 200 m/s to 300 mm/s in Figure 4-7a) and, consequently, the radiative loss are expected to increase moderately with the oxidizer velocity. As a consequence, the characteristic time-scale for radiative loss can be assumed, in a first approximation, to remain independent of U_{ox}. Assuming t_{rad} = constant in equation (4.21) implies that L_f scales with U_{ox}. This suggests that L_f increases with U_{ox} as observed experimentally. Figure 4-6 shows also that, for a given OI and U_{ox}, the L_f increases with the V_F. This behavior is in accordance with the scaling analysis developed in the previous section. Eventually, Figure 4-6 indicates that, for given fuel and oxidizer velocities, the L_f decreases when increasing the OI. This trend also agrees that obtained from the theoretical analysis derived in the previous section.

4.1.3.3. Soot production

Figure 4-7 shows the evolution of integrated soot volume fractions as a function of the distance from the burner leading edge. The effects of the oxidizer velocity are analyzed on Figure 4-7a that considers different U_{ox} for a fuel velocity of 5 mm/s and an OI of 50%. The effects of the V_F are investigated in Figure 4-7b whereas those of the OI are considered in Figure 4-7c. In all the configurations, the integrated soot volume fraction increases due to soot formation, reaches a peak and decreases as soot oxidation prevails. Figure 4-7a shows that the integrated soot volume fraction increases as the U_{ox} decreases. It can also be observed that the peak location shifts downstream as the U_{ox} is reduced. This behavior is inversed as compared to that observed for the L_f which was found to increase with the oxidizer velocity. This shows that the L_f is not a relevant quantity to define the residence time for soot formation. This is a consequence of the fact that the present flames belong to the category of *"open-tip"* flames. In the following the residence time for soot formation is defined by:

$$t_{res,S} = \frac{L_S}{U_{ox}} \tag{4.22}$$

where L_S is the distance between the burner leading edge and the peak of integrated soot volume fraction.

Figure 4-7b shows that the integrated soot volume fraction increases with the V_F. In addition the peak location seems to be slightly shifted away from the burner as the V_F is

increased, suggesting a slight increase in L_S . Figure 4-7c shows that both the location and the value of the peak of integrated soot volume fraction are reduced as the OI increases (S decreases).

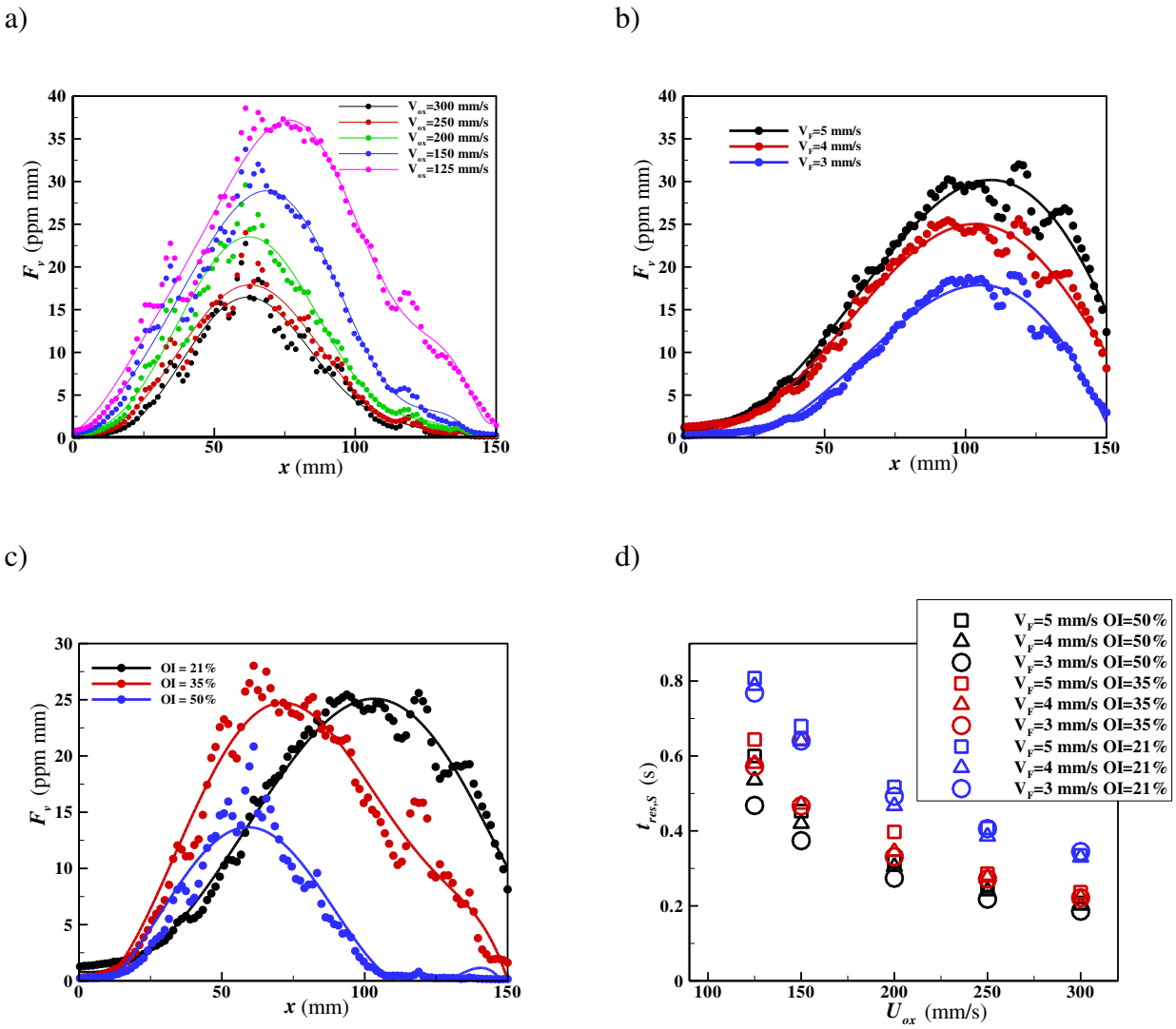

Figure 4-7: Represents the effects on maximum soot volume fraction of a) oxidizer velocity (U_{ox}) for V_F=5 mm/s and OI 50%, b) Fuel injection velocity (V_F)for a U_{ox}= 250 mm/s and OI=21%, and c) oxidizer index (OI) for a V_F=5 mm/s and U_{ox}=300 mm/s. d) Residence time as a function of the oxidizer velocity for different fuel velocities and oxidizer velocities.

The evolution of the residence time, defined by equation (4.22), as a function of the oxidizer velocity is displayed in Figure 4-7d. As expected from equation (4.22) and Figure 4-7a, the residence time for soot formation decreases significantly as the U_{ox} increases, explaining the

reduction in the peak of soot volume fraction observed in Figure 4-7a. Figure 4-7d shows also that, for a given U_{ox} and OI, the residence time increases slightly with V_F. Finally, increasing the OI is found to reduce the residence time.

Figure 4-8 represents the evolution of the peak of soot volume fraction as a function of the residence time for soot formation, defined by equation (4.22). According to equations (4.19) and (4.20), for a given OI, the peak of soot volume fraction is expected to increase linearly with the residence. Figure 4-8 shows that this linear dependency is observed. Figure 4-8 shows also that, for a given residence time, the evolution of the peak of soot volume fraction follows a non-monotonic behavior with the OI, increasing first when the OI is enhanced from 21% to 35% and then decreasing when the OI is further enhanced to reach 50%. The increase in oxygen has conflicting influences on soot kinetics:

a) Higher oxygen concentration increases the hydrogen-radical pool (H_2–O_2 chemistry). The hydrogen radicals are very active and result in more radical sites on the soot surfaces, which in turn increases acetylene-addition and hence promotes soot growth (via surface reactions).

b) Increased oxygen oxidizes the soot precursors as well as the soot that is being formed, thereby reducing the soot formation.

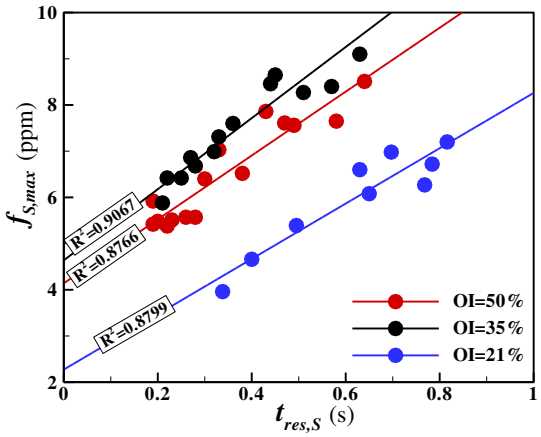

Figure 4-8: Peak of soot volume fraction as a function of the residence time. Red, black and blue symbols are used for OI 50, 35 and 21, respectively.

The net effect of oxygen enrichment is therefore determined by the relative importance of these two effects. For relatively low levels of oxygen enrichment, the increasing oxygen results in

a larger increase of the hydrogen-radical pool and hence a much enhanced soot growth. For high levels of oxygen enrichment, the increased soot (and soot precursor) oxidation rates dominate. The oxygen index at which the change in behavior is observed is between 35% and 50%. This is consistent with the results obtained by Wang et al (L. Wang et al. 2002) in the case of turbulent jet diffusion flames fueled by propane and a blend of methane/ethylene. The characteristic time-scale for soot formation is then reduced as the OI is increased from 21% to 35% and enhanced as the OI is further increased to 50%.

4.1.4. Conclusions remarks

Experiments, carried out in parabolic flight to investigate the behavior of microgravity LBL diffusion flame, have been analyzed. The effects of the oxidizer velocity, fuel velocity and the oxygen index, defined as the amount of oxygen in the oxidizer, on flame geometry and soot production have been investigated. The following conclusions can be drawn:

- The flame stand-off distance exhibit three regimes as the distance from the burner leading edge increases: the first regime is controlled by the fuel injection and the stand-off distance increases linearly with x. This length over which this regime prevails increases as the ratio between the oxidizer velocity and the fuel velocity increases. The second regime is diffusion controlled and the stand-off distance increases with $x^{1/2}$. The third regime appears at the railing edge of the burner and is attributed to tridimensional effects.
- The flame length is controlled by radiant extinction at the flame trailing edge. This mode of extinction occurs at high Damköhler number for long residence in presence of radiative loss. These flames belong then to the category of “open-tip” flames. Flame length was found to increase with the oxidizer and fuel velocities and with the OI.
- The characteristic length scale for soot formation does not evolve as the flame length. As a consequence, the flame length can no longer be used as characteristic length scale in “open-tip” flames. A residence time based on the location of the peak of integrated soot volume fraction and the oxidizer velocity was found appropriate to study soot formation.
- The characteristic time for soot formation was found to exhibit a non-monotonic behavior with the OI. It is reduced as the OI is increased from 21% to 35% and is increased as the OI is further enhanced to 50%. This behavior results from a competition between the

increase in H radical, that enhances the HACA process and soot surface growth, and the increase in oxidation as the OI increases. The first mechanism prevails between 21% and 35% whereas the second becomes dominant as the OI is further increased.

4.2. Numerical analysis

4.2.1. Chemical mechanism

The extended version of the chemical kinetic scheme developed initially by Slavinskaya et al. (Slavinskaya and Frank 2009) for C_2 and updated by Dworkin et al. (Dworkin et al. 2011) and by Chernov et al. (Chernov et al. 2012) is used in the present study. It consists of 94 species and 723 reactions. For the growth of PAH beyond first ring the HACA mechanism is used. The steric factor for the HACA process is now a constant set equal to 0.1 to be in line with the works of Dworkin and coworkers (Dworkin et al. 2011).

4.2.2. Computational details

Two-dimensional numerical calculations were performed on a domain of 360 mm (x) × 190 mm (z). A constant mesh size zone of 0.9 x 0.75 mm^2 was used in the flaming region. In the rest of domain a non-uniform mesh was implemented. The total number of cells was 169 (x) × 93 (z). The fuel and oxidizer were injected according to the experimental conditions of Fuentes (Fuentes 2006) with a flat velocity profile. The temperature of injection was 300 K and the effects of fuel preheating were neglected. Pressure is set at 1 atm. The calculations are carried out only for an oxygen index of 21%. Two oxidizer velocities of 250 and 300 mm/s and three fuel velocities of 3, 4, and 5 mm/s are considered. Calculations were performed on a desktop PC with a 64 bit Intel i7 processor (3.4 Ghz, 16 GB RAM). Approximately 75000 iterations were necessary to reach convergence with a CPU time of about 60 days. The numerical domain and boundary conditions are given in Figure 4-9.

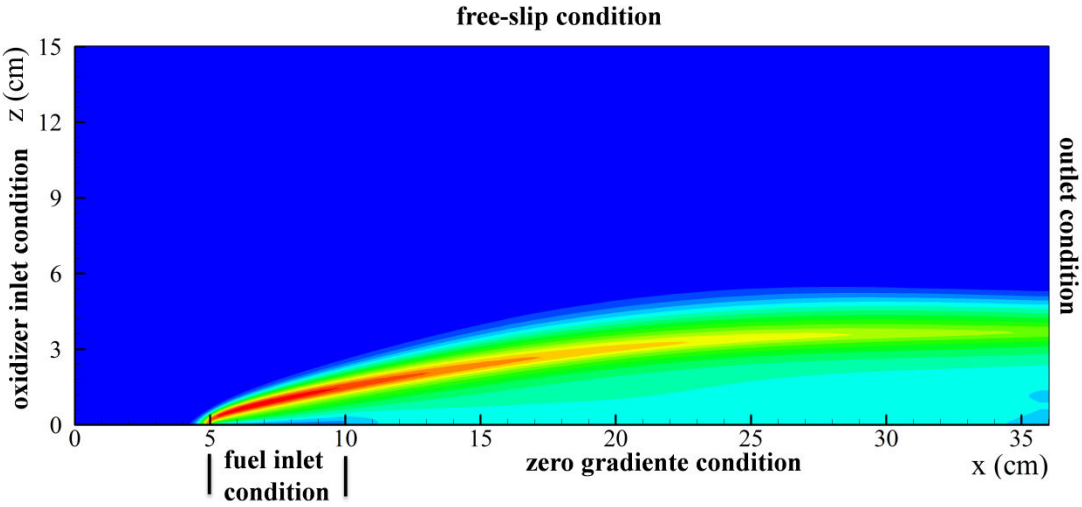

Figure 4-9: Numerical domain and boundary conditions.

4.2.3. Comparison with available data

The aim of this section is to compare the numerical predictions with the experimental data reported in the previous section. As seen previously the experimental data presents 3D effects beyond the burner trailing edge. Legros and coworkers (Legros et al. 2009), have shown that due to these 3D effects, the streamlines, that transport soot inside the boundary layer, cross the high temperature zone two times which has a considerable influence on the oxidation process. The present calculations are 2D and, of course the 3D effects on flame geometry and soot production, are not captured. As a consequence, the comparison between the numerical results and the experimental data are limited to the region upstream the burner trailing edge where the flow is expected to be 2D.

4.2.3.1. Stand-off distance (SOD)

The SOD represents the distance between reaction zone and burner plate. It is an important issue for flames spread over combustible materials since it determines the amount of convective heat transferred from the flame towards the fuel surface.

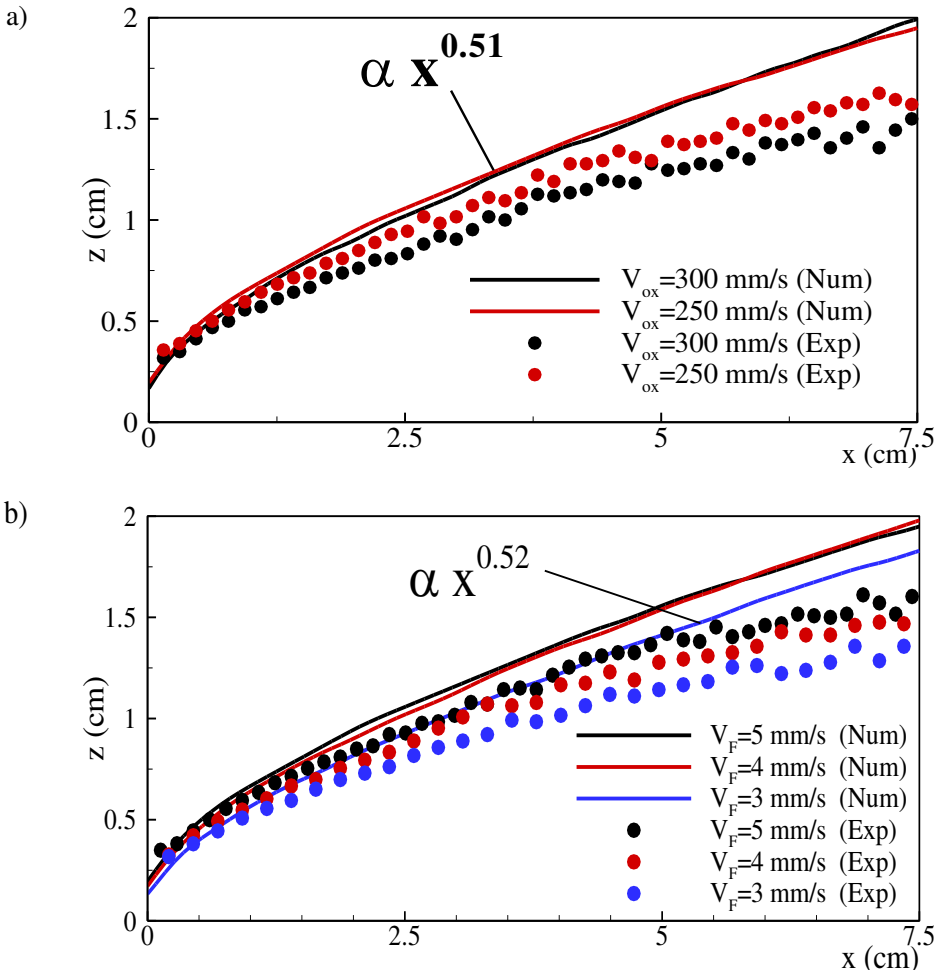

Figure 4-10: Evolution of the stand of distance as a function of the distance along the plate. a) influence of the U_{ox} for a given V_F of 5 mm/s, b) influence of the V_F for a given U_{ox} of 250 m

Figure 4-10 shows the evolution of the calculated SOD as a function of the distance along the plate. The predicted SOD is determined as the vertical location of the maximum value of the molar concentration of OH* radicals. The corresponding measurements are also plotted in this figure. A fit of the numerical data for U_{ox} = 250 mm/s in Figure 4-10a indicates that, as expected from the laminar boundary layer (LBL) theory (Emmons 1956), the SOD increase with $x^{1/2}$. It should be pointed out that the convective regime observed in the region close to the burner leading edge is not clearly observed in the numerical model. Computed stand-off distances agree on the whole well with the experimental data, despite slight overpredictions. The discrepancies seem on the whole to become more significant beyond the trailing edge of the porous burner and

can be attributed to the appearance of 3D effects (Fuentes, Legros, Claverie, et al. 2007; Legros et al. 2009).

The influence of U_{ox} on the evolution of SOD is discussed in Figure 4-10a where the evolution of the SOD as a function of the distance along the plate was plotted for the two different U_{ox} and at a fixed V_F=5 mm/s. The influence of U_{ox} appears clearly for the experiments but not for simulations in the domain analyzed. In experiments the boundary layer becomes thinner as the oxidizer velocity increase but in simulations we see that both oxidizer velocities overlap in zone above burner ($0 < x < 5$ cm) but then, in the trailing edge of burner, models starts to capture the experiments trend.

Figure 4-10b shows the evolution of SOD, along the burner plate, for three different V_F of 3, 4 and 5 mm/s at a fixed U_{ox}=250 mm/s. As was shown by Rouvreau et al. (Rouvreau et al. 2002), the reactive boundary layer is pushed away from burner plate as V_F increases. This behavior is confirmed experimental data and also for model results when we compare V_F of 3 and 4 mm/s. V_F=5 mm/s is less evident and results are overlapped with V_F=4 mm/s.

4.2.3.2. Soot production

The Discussion focuses now on the soot quantities. The experimental uncertainties on soot volume fraction were estimated to be of ± 44% (Fuentes, Legros, El-Rabii, et al. 2007).

Figure 4-11 shows the predicted profiles of soot volume fraction, f_s, as a function of the z-coordinate for different locations along the plate and the corresponding measurements obtained by Fuentes (Fuentes 2006). This figure shows that, whatever the fuel and oxidizer velocities, the peak of soot volume fraction and the width of the sooting region increase with the distance along the plate. The increase in the width of the sooting region is mainly related to the increase in the stand-off distance with the distance along the plate. The numerical model reproduces correctly these trends although the peak of soot volume fraction is significantly overpredicted in the region located between the burner trailing edge and x = 3.75 cm. The agreement between the numerical model and the experimental data concerning the peak of soot volume fraction is considerably improved as the distance along the plate increases. The results reported in Figure 4-11 shows also that the width of the sooting region and the vertical location of the peak of soot volume fraction are overpredicted from x = 3.75 cm. This overestimation can be related, at least partially, to an overestimation of the SOD (see Figure 4-10).

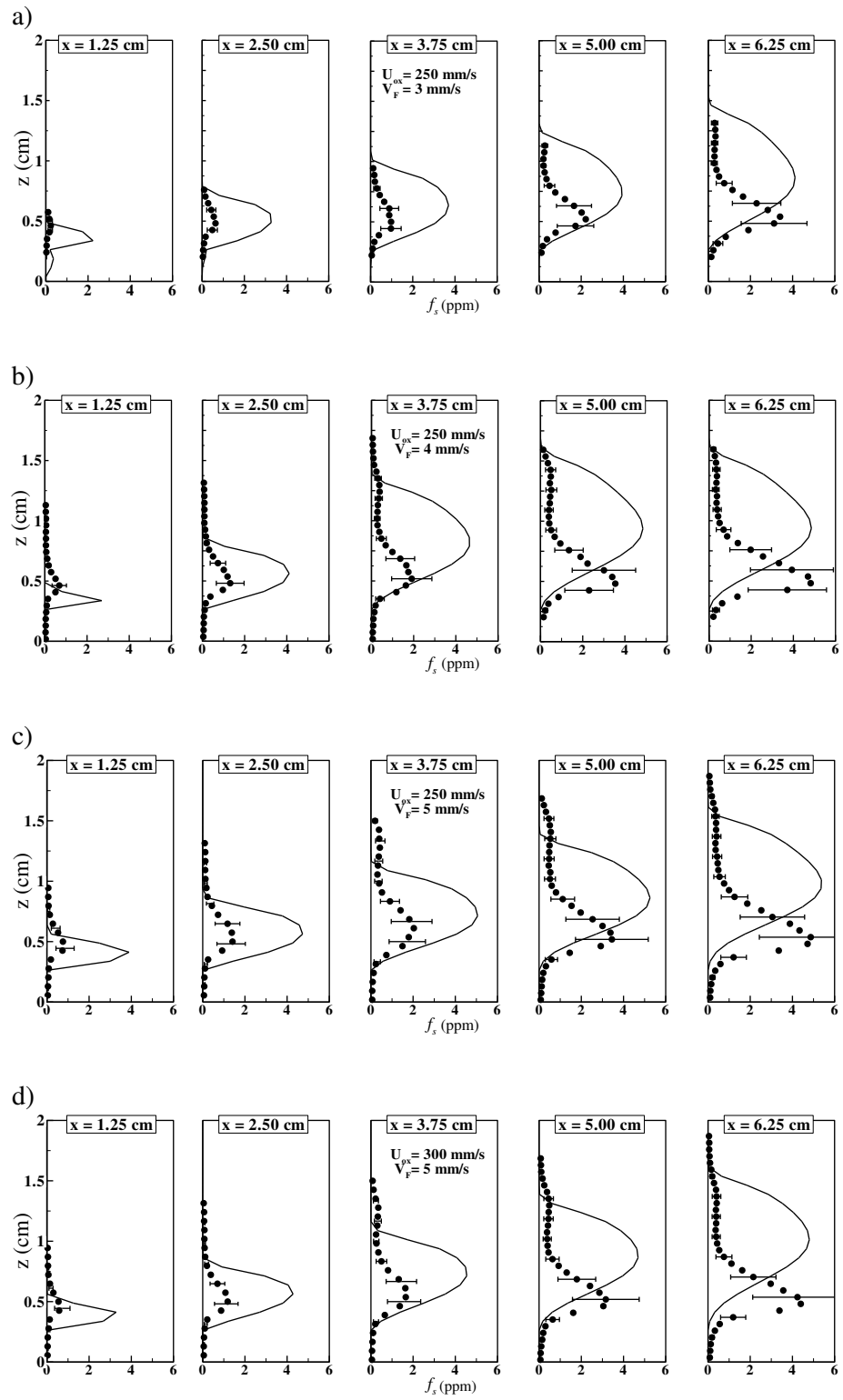

Figure 4-11: Vertical profiles of soot volume fraction at different longitudinal locations for a) V_F=3 mm/s and U_{ox}=250 mm/s, b) V_F=4mm/s and U_{ox}=250 mm/s, c) V_F=5mm/s and U_{ox}=250 mm/s, d) V_F=5 mm/s and U_{ox}=300 mm/s.

The images a, b and c of Figure 4-11 display the effects of the fuel injection velocity for at a fixed oxidizer velocity of 250 mm/s. At a given location along the plate, the experimental peak of soot volume fraction increases with the fuel injection velocity. This behavior is more pronounced when the V_F is increased from 3 mm/s to 4 mm/s than when it is increased between 4 mm/s and 5 mm/s. The predicted peak of soot volume fraction follows the same trends as the experiments. Figure 4-11c and Figure 4-11d display the effect of U_{ox} for a fixed V_F=5 mm/s. Both measured and predicted peaks of soot volume fraction become lower when the oxidizer velocity increases.

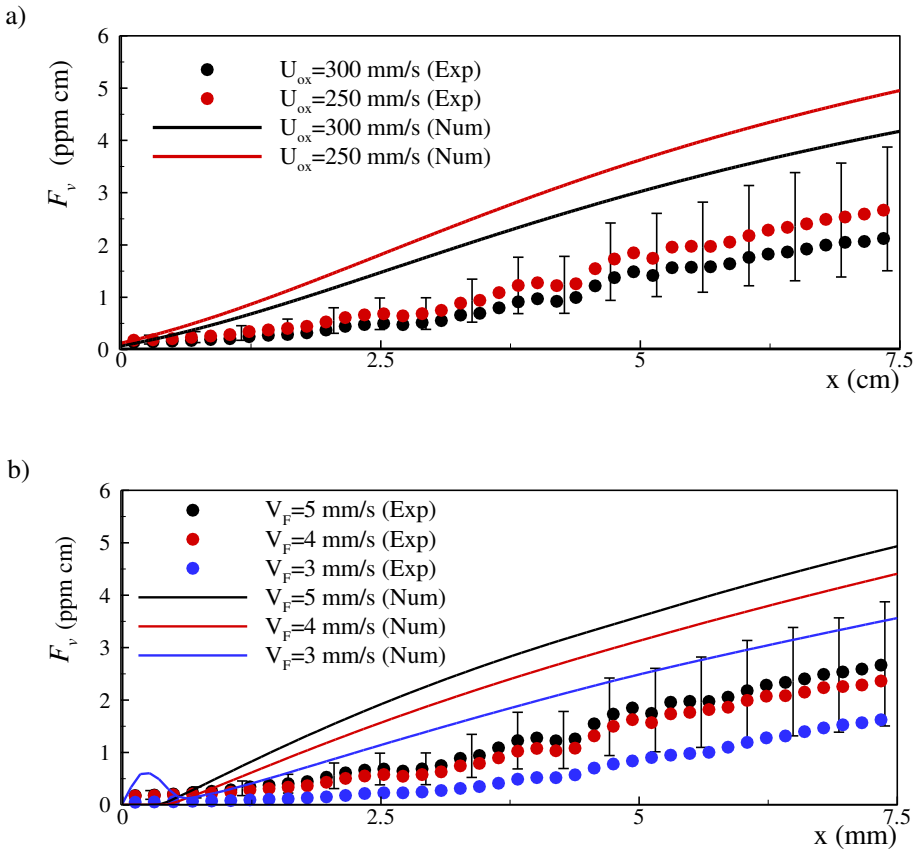

Figure 4-12: Integrated soot volume fraction, a) effect of the oxidiser velocity for a given fuel injection velocity of 5 mm/s, and b) effect of the fuel injection velocity for a given oxidizer velocity of 250 mm/s.

Figure 4-12 shows the evolution of the integrated soot volume fraction, defined as $F_v(x) = \int_o^\infty f_s(x,y)\,dz$, as a function of the distance along the plate. As discussed in the previous section, Figure 4-12a shows that the integrated soot volume fraction (F_v) increases as the U_{ox}

decreases and as the V_F increases. This trend is well reproduced by the numerical model. However the F_v is overprediced. This overprediction can be attributed to an overestimation of the peak of soot volume fraction close to the burner leading edge and to an overestimation of the width of the soot region close to the burner trailing edge.

4.2.4. Flame structure

Figure 4-13 shows a qualitative description of the flame structure in terms of OH*, PAH and soot contours for a fuel velocity of 3 mm/s and an oxidizer velocity of 250 mm/s. Both numerical and experimental flame structures are similar. The OH* contour delimits the reaction zone and evolves with $x^{1/2}$ as described previously. PAHs are located between the plate and the lower part of the OH* zone where they are likely oxidized. Soot is embedded in the PAH zone. Its appearance is delayed along the plate as compared to that of PAH since its formation requires longer times. The region occupied by soot is thinner in the z-direction than the PAH zone which suggests that PAHs are oxidized farther from the plate than soot.

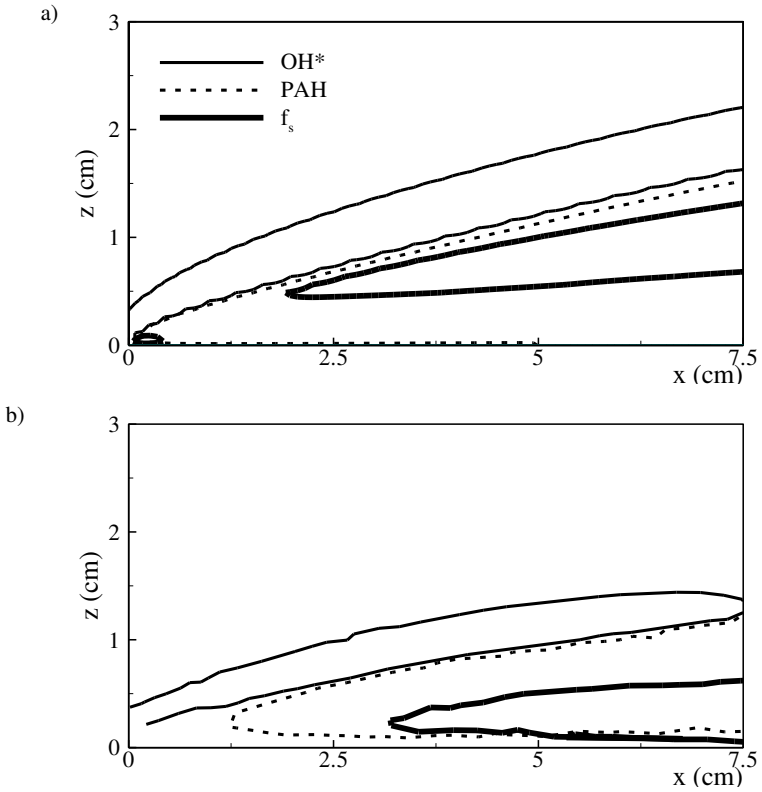

Figure 4-13: Interaction between reaction zone, soot formation and soot concentration for VF=3 mm/s. Iso-contours for: a) numerical results, and b) experimental results.

Figure 4-14 a) and b) illustrate the soot production processes. Figure 4-14a shows the streamlines, the line of maximum temperature, the region where soot growths by inception, surface growth (HACA) and PAH-surface condensation, the region where soot is oxidized mainly by OH*, and the contours of soot volume fraction. As expected, the maximum temperature increases approximately with $x^{1/2}$ in a similar manner as the stand-off distance. Model results show that soot is formed in a region located below the line of maximum temperature (fuel rich zone) and that this region follows the stand-off distance.

The soot produced in this region is then transported along the streamlines but also by thermophoresis inside the boundary layer. It should be pointed out that the z-component of the thermophoretic velocity is about of the same order of magnitude as the z-component of the velocity but has an opposite sign being directed toward the plate. The soot oxidation zone also locates below the line of maximum temperature and follows the stand-off distance which is consistent with the contours of OH radical observed in Figure 4-14a.The locations of the species responsible for soot formation are represented in Figure 4-14b in order to provide a better understanding concerning the shape of the soot formation region. Soot inception and PAH-surface condensation are directly related to the concentration of Pyrene. Figure 4-14b shows that Pyrene is contained in the zone where soot is produced. The HACA process results from the attack of H and OH radicals that produce de-hydrogenated active sites on the soot surface which allows the addition of acetylene. Figure 4-14b shows that the concentration of Acetylene is significant inside the whole region delimited by the plate and the line of maximum temperature. On the other hand, OH and H radicals are located in the region where soot is produced, showing that these species delimit the region where the HACA process occurs.

Figure 4-14c displays the integrated soot formation rate, defined as the integration of inception, surface growth and PAH-surface condensation rates over the z-coordinate, as a function of the distance along the plate. Results show that the integrated soot formation rate increases rapidly close to the leading edge of the burner, mainly due to higher local concentration of soot precursors, reaching a peak around x=1 cm. Beyond x = 1 cm it decreases slowly as x increases. As expected, the soot formation rate is found to increase with the fuel velocity.

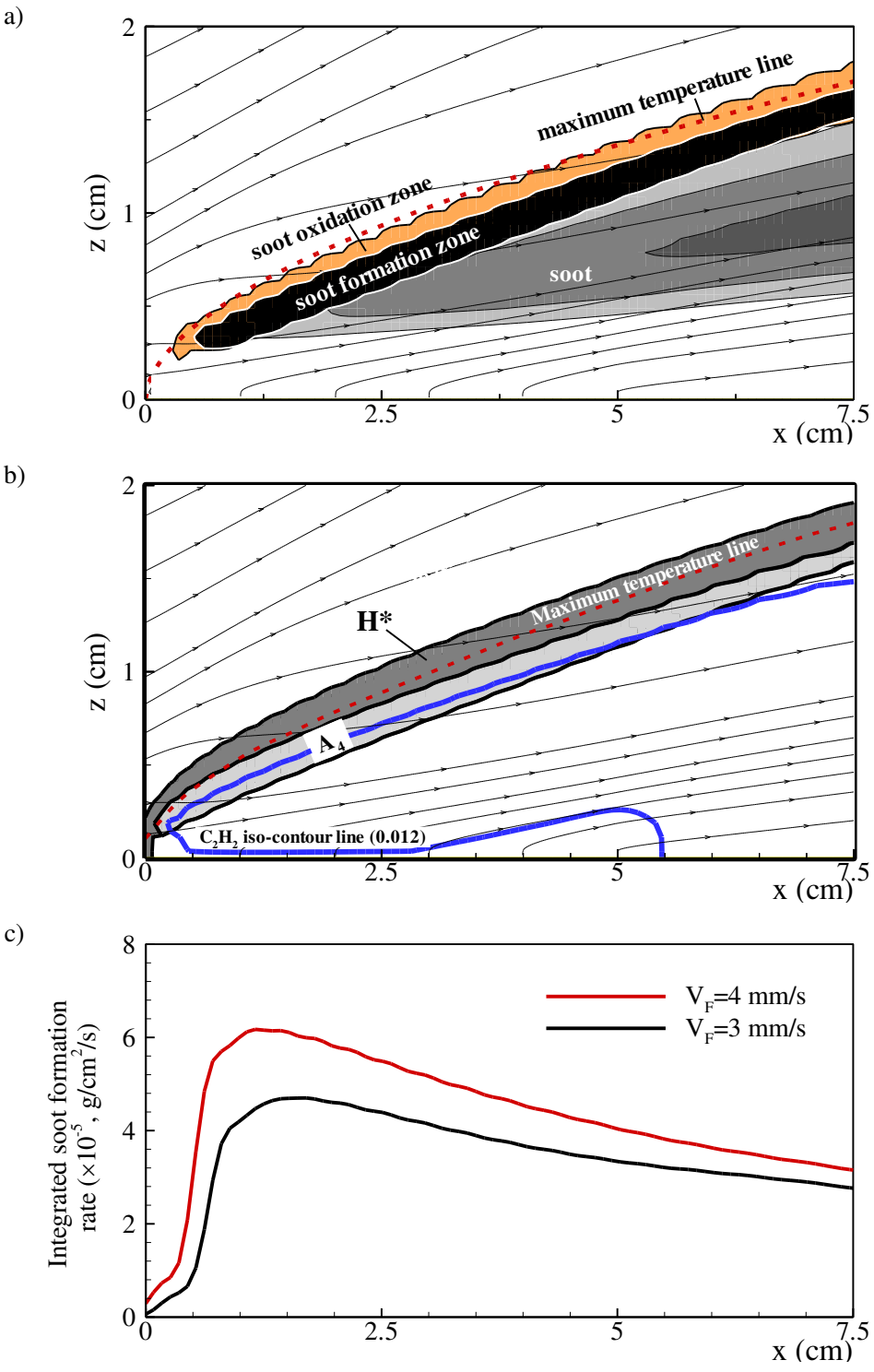

Figure 4-14: a) Soot production interaction for V_F=3 mm/s, b) soot production precursor species interaction for V_F=3 mm/s, and c) integrated soot formation rate as a function of x-coordinate for V_F=3 mm/s and V_F=4 mm/s.

4.2.5. Further discussion

In this section, a special attention is paid to the flame quenching at the flame trailing edge. Figure 4-15 shows the influence of both fuel and oxidizer velocities on the iso-contours 1400 K which is assumed to delimit the flame. This temperature has been selected for two reasons. First, it corresponds approximately to the temperature below which soot ceases to be oxidized and can then be considered as an indicator of the luminous flame (Kent 1986; Markstein and De Ris 1985). Secondly, it is close to the extinction temperature of 1500 K ± 50 K proposed by Williams (Williams 1981) for hydrocarbon combustion in oxygen/nitrogen mixtures. It should be also pointed out that the choice of this temperature to define the flame shape does not affect the analysis of the results. A comparison between Figure 4-15 a) and b) shows that, consistently with the experimental results provided in Section 4.1.3, the flame length decreases with the oxidizer velocity for a given fuel velocity. Figure 4-15 b), c) and d) show that the flame length increases with the V_F for a given U_{ox} which is also in agreement with the experimental observations reported in Section 4.1.3. These similarities sustain that the 3D effects, which are present in the experiments and not in the calculations, does not play a role in the failing of the scaling model reported in Section 4.1.2.3 to predict the reduction in L_f with the U_{ox}.

Table 4-1 presents some characteristics of the flames studied in the present work. The third column represents the L_f, defined as the distance from the burner trailing edge to the farthest location along the plate reached by the iso-contour 1400K. The residence time, which is given in the fourth column, is defined as the ratio between the flame length and the oxidizer velocity ($\left(t_{res} = L_f / U_{ox}\right)$. It should be pointed out that these times are approximately one order of magnitude longer than those observed in laminar axisymmetric flames at normal gravity and are more consistent with those computed in laminar axisymmetric flames at micro-gravity (Demarco, Nmira, and Consalvi 2013). For a given V_F, the t_{res} is found to increase as the U_{ox}. For a given U_{ox}, it is found to increase with the V_F as the result of an increasing L_f. The fifth, sixth and seventh columns represent the theoretical HRR, based on an assumption of complete combustion, the heat released by the chemical reactions, $\dot{Q}_{chem}$, and the combustion efficiency, defined by the ratio between $\dot{Q}_{chem}$ and the HRR. The HRR increases with the V_F due to an increase in the fuel mass flow rate. For a given fuel velocity, $\dot{Q}_{chem}$ is found to decrease slightly with the V_F. For a given U_{ox}, $\dot{Q}_{chem}$ increases with the V_F following the same trend as the HRR. The combustion efficiency is of particular interest

in the present problem since it quantifies the part of the theoretical HRR that burns effectively. In the case where the combustion is complete, i.e. if all the fuel is consumed at the flame tip, it should be around 1. The results reported in Table 4-1 shows that it is significantly lower than 1 for all the flames considered, demonstrating that a significant part of the fuel injected through the burner escapes from the flame without being oxidized. This confirms that the present flames belong to the category of "open-tip" flames. For the range of oxidizer velocity considered, the effect of U_{ox} on the combustion efficiency is rather low. The influence of the fuel velocity appears to be more pronounced, the combustion efficiency increasing significantly as the fuel velocity is reduced. This suggests that the flame quenching at the trailing edge occurs comparatively earlier as the fuel velocity increases.

Since the radiative losses are responsible of the quenching process, the total radiative heat loss, $\left(\dot{Q}_{rad}\right)$, defined as the integration of the divergence of the radiative flux over the computational domain and the radiant fraction, defined as the ration between $\dot{Q}_{rad}$ and the HRR, are of interest. The first important point is that the radiant fractions computed for the present flames are significantly higher than those observed in axi-symmetric laminar flames at normal gravity that do not exceed 0.3 even for heavily sooting flames (Demarco et al. 2011). They are similar to those observed in axi-symmetric flames in micro-gravity which can be explained by the similar residence encountered in the two configurations. The second important point is that although the heat radiated away from the flame increases with the V_F, the radiant fraction decreases, implying that the increase in radiation loss is weaker than the increase in HRR. This behavior is different from that observed in "closed-tip" axisymmetric flames (Demarco, Nmira, and Consalvi 2013) and may be interpreted as a characteristic of the open-tip nature of the present flames. The last column shows the computed characteristic time for the radiative cooling, defined as:

$$t_{rad} = \frac{\rho_\infty C_p \left(T_{f,max} - T_{f,q}\right)}{\frac{\int_{T>T_{f,q}} \nabla \bullet q_R dv}{\int_{T>T_{f,q}} dv}} \tag{4.23}$$

In the previous expression, $T_{f,max}$ and $T_{f,q}$ represent the maximum temperature in the flame and the temperature at the flame quenching, i.e. 1400K in the present study. The term in the denominator represents an average value of the radiative source term. The t_{rad} term can be interpreted as the time requires cooling down the temperature of the flame from its maximum to the temperature of flame quenching due to radiative loss. The results show that this time is not really sensitive to the oxidizer velocity and to the fuel velocity. This justifies the assumption used in section 4.1.2 where it was assumed to be independent of the oxidizer velocity to provide an explanation for the increase in flame length with U_{ox}.

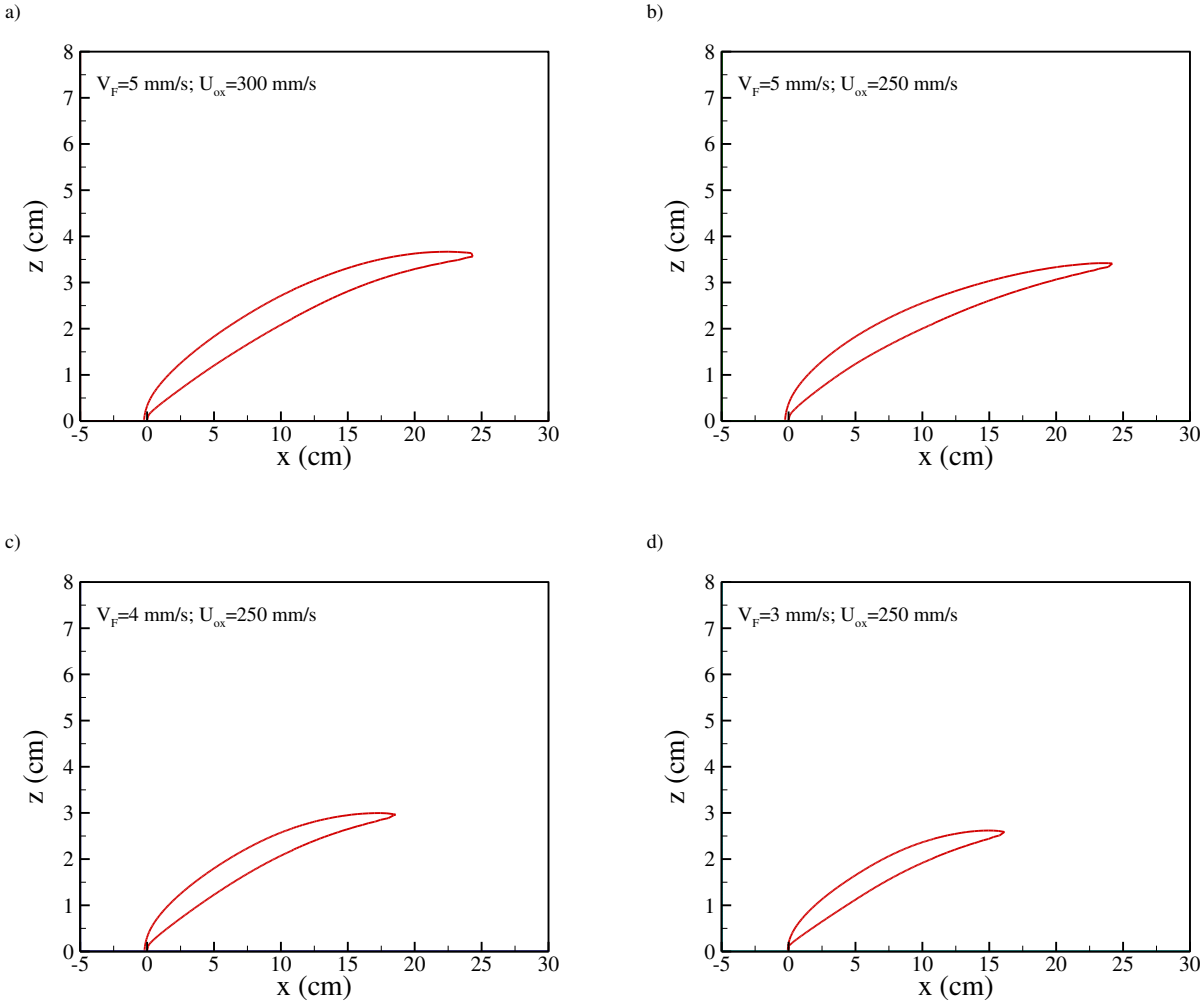

Figure 4-15: Effects of oxidizer velocity and fuel velocity on flame length

Table 4-1: Some characteristics of the flames: oxidizer velocity, fuel velocity, flame length, residence time, Heat Release Rate (HRR), heat released by chemical reactions, combustion efficiency, heat released due to radiative loss, radiant fraction, characteristic time for radiant cooling.

U_{ox} (mm/s)	V_F (mm/s)	L_f (mm)	t_{res} (s)	HRR (W/m)	$\dot{Q}_{chem}$ (W/m)	χ (–)	$\dot{Q}_{rad}$ (W/m)	χ_R (–)	t_{rad} (s)
300	5	239.5	0.790	148.3	93.4	0.63	71.8	0.48	0.25
250	5	215.3	0.860	148.3	90.8	0.61	65.9	0.44	0.25
250	4	184.3	0.737	118.8	85.6	0.72	61.0	0.51	0.23
250	3	161.7	0.646	93.1	77.5	0.83	54.6	0.59	0.19

4.2.6. Radiative heat transfer

The radiative heat transfer plays a major role in both soot formation and flame quenching at the trailing edge. The aim of the section is to provide a better understanding of the radiative structure of the flames and to investigate how the use of approximate radiation model affects the soot production process and the radiative quenching at the trailing edge. The analysis will be provided by considering the flame with an oxidizer velocity of 250 mm/s and a fuel velocity of 3 mm/s. Similar trends were observed for the other flames.

Calculation have been run by considering the following approximate radiation models: (i) disregarding the radiative contribution of both participating gases and soot (no radiation), (ii) disregarding the radiative contribution of soot (no soot), (iii) assuming soot is a gray species by using its Planck-mean absorption coefficient. This model will be referred as gray soot in the following, (iv) assuming both soot and participating gases are gray species. The Planck-mean absorption coefficient was considered for each radiating species. This model will be denoted as Planck mean hereafter. To be consistent with the reference model, the Planck-mean absorption coefficients considered in models iii and iv are computed from the SNBCK wide-band model. It should be pointed out that the differences between gray soot and Planck mean results from the spectral dependence of gaseous radiatively participating species, namely CO, CO_2 and H_2O. (v) The Optically-Thin Approximation (OTA) where the reabsorption of both participating gases and soot is neglected. The results will be compared with the standard SNBCK-wide band model described in the numerical model section and which is used as a reference. The OTA is generally

valid in axisymmetric laminar diffusion flames at normal gravity even in the case of highly sooting fuels (Demarco et al. 2011).

4.2.6.1. Radiative structure

The field of the divergence of the radiative flux is reported in Figure 4-16. The line of maximum temperature, the iso-contours where the divergence of the radiative flux, $\left(\vec{\nabla}\cdot\vec{q}''\right)$, is zero and f_s = 2 ppm, and the contour delimiting the region of soot formation are also plotted in this figure. In the most important part of the flame, the divergence of the radiative flux is negative indicating that radiative emission prevails on absorption. Nevertheless, absorption is found to dominate at vicinity of the plate where relatively cold radiating species are located. The minimum values of the divergence of the radiative flux are located inside the boundary layer and correspond to the region where soot is produced.

An analysis of the relative contribution of soot and gaseous radiatively participating species was performed, showing that soot contributes for approximately one half of the radiative loss. This shows that neither the contribution of soot nor the contribution of the gaseous radiatively species can be neglected.

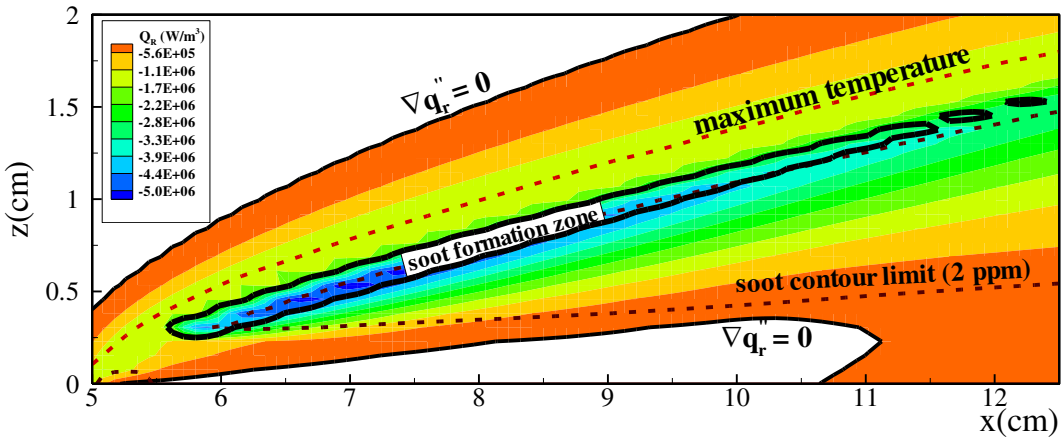

Figure 4-16: Divergence of radiative flux for V_F=3 mm/s and U_{OX}=250 mm/s

4.2.6.2. Effects of approximate radiation models

4.2.6.2.1. Radiant fractions

Table 4-2 shows the radiant fraction computed with the complete radiation model and the different approximate models. It should be pointed out that the capability of the different approximate models is assessed by considering coupled calculations in which the temperature, the molar fraction of the different species and the soot volume fraction are modified. This makes the interpretation of the results more difficult than in the case of frozen calculation where the temperature, the molar fraction of the different species and the soot volume fraction are maintained unchanged and the assessment concerns the radiative outputs only. Neglecting soot volume fraction reduces the radiant fraction by about 18%. The gray soot, the Planck mean and the OTA leads to higher radiant fractions than the complete model since these models tend to underestimate the absorption. As expected, the largest discrepancies are observed in the case of the OTA where the absorption is completely neglected and are of about 12%. Considering soot and gas as gray species improve the results leading to an overestimation of 7% of the radiant fraction. The radiant fraction computed with the gray soot approximation is close to that predicted with the Planck mean model.

Table 4-2: Fraction of the HRR radiated away from the flame χ_R with a fuel velocity of 3 mm/s and an oxidizer velocity of 250 mm/s.

Complete	No soot	Gray soot	Planck mean	OTA
0.59	0.48	0.62	0.63	0.66

4.2.6.2.2. Flame geometry

This section investigates the influence of radiation model on the flame geometry. A special attention is paid to the flame quenching at the flame trailing edge. As previously discussed, the flame contour was delimited by the temperature iso-contour of 1400 K. Figure 4-17 shows the flame contours calculated using the different radiation models investigated. In the case of the reference model the combustion efficiency, defined as the ratio between the actual heat release rate and that in the case of a complete combustion, is 85% indicating that the flame

quenches at the trailing edge before of fuel is fully burnt. In the reference solution, the flame length (L_f) is 16.55 cm and the flame stand-off distance at the trailing edge is 2.81 cm.

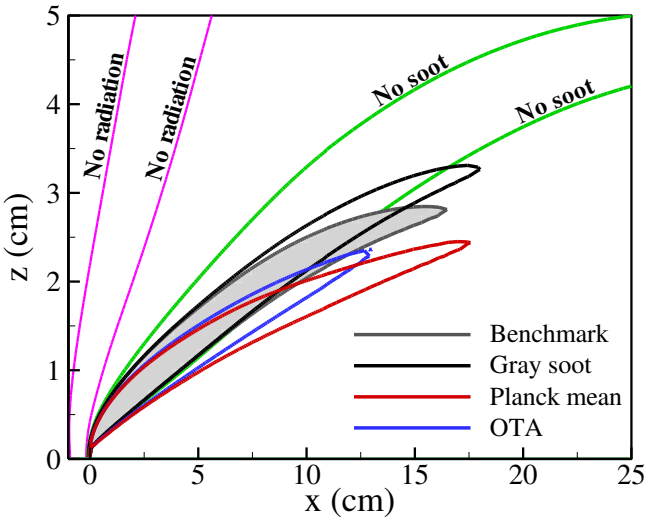

Figure 4-17: Flame shape for different radiation models.

The simulation carried out with no radiation confirms that the influence of radiation cannot be neglected in this type of flames. The flame geometry is completely modified as compared to the reference case. Firstly, it is much larger due to higher temperature and then thermal expansion. Secondly, the flame is much taller since no quenching occurs at the trailing edge. In the present case the flame tip occurs outside of the computational domain. Ignoring the participation of soot in radiation computation also results in higher temperature which leads to a much larger and longer flame than that found in the reference case. The flame tip occurs also outside of the computational domain and no conclusion can be then drawn about the completeness of the combustion process. This confirms the importance of the continuous radiation of soot. Computation with gray soot (black solid line) and Planck mean (red solid line) models result in longer flame lengths than for the reference case. Flame length is increased from 16.55 cm for complete case to 18.06 cm and 17.62 cm for gray soot and Planck mean cases, respectively. The influence of these approximate radiative models is also pronounced on the stand-off distance at the flame tip which is increased from 2.81 cm (reference case) to 3.27 cm for gray soot model and decreased to 2.45 cm for Planck model. In addition, the combustion efficiency is reduced to 76% as compared to 85% for the reference radiation model. The OTA enhances the radiative

losses as compared to the reference case and, as a consequence, favors flame quenching at the trailing edge. This results in a significantly shorter flame of about 12.85 cm, showing that this approximation leads to significant errors.

The phenomenon of flame quenching at the trailing edge laminar boundary layer flames in microgravity is a typical case of radiative extinction. The previous comparison revealed that the significant contribution of soot radiation on this phenomenon. As a consequence only the influences of the approximate models iii) to v) on flame temperature and soot formation will be discussed in the following.

4.2.6.2.3. Temperature

Let us first consider the flame temperature. Figure 4-18b), c) and d) displays the distribution of errors in the predicted flame temperature by considering the gray soot, Planck mean and OTA models, respectively. The error was defined as the difference between the temperature computed with the approximate model and that calculated with the reference model ($\Delta T = T_{\text{model}} - T_{\text{ref}}$), this latter being displayed in Figure 4-18a. Figure 4-19b shows that the error for the gray soot model presents four clear quadrants along the flame. Between the flame leading edge and the flame tip the gray soot model overpredicts the temperature in the region above the flame reaction zone with a maximum discrepancy of 135 K. On the other hand, the gray soot model underestimates the temperature below the flame reaction zone with a maximum discrepancy of 138 K.

Beyond the flame tip, the trend observed previously is inverted with an overpediction in the region between the plate and the stand-off distance. These results show clearly that the spectral dependence of soot has to be taken into account.

The second approximate model, namely the Planck mean, presents qualitatively the same trends as the gray soot model. However, larger discrepancies are observed with maximum over- and under-predictions of 183 K and 283 K, respectively. Comparison with the discrepancies observed in the case of gray soot allows to quantifying the influence of the spectral dependence of gaseous participating species. Eventually, the OTA underpredicts temperature essentially everywhere in the computational domain. This is expected since the absorption of radiation is neglected. In the region between the plate and the flame contour, the discrepancies are found to increase as the distance along the plate increases. The maximum discrepancies occur upstream the flame tip and

are of about 637 K, indicating that the effect of radiation absorption of this part of boundary laminar diffusion flame is very important.

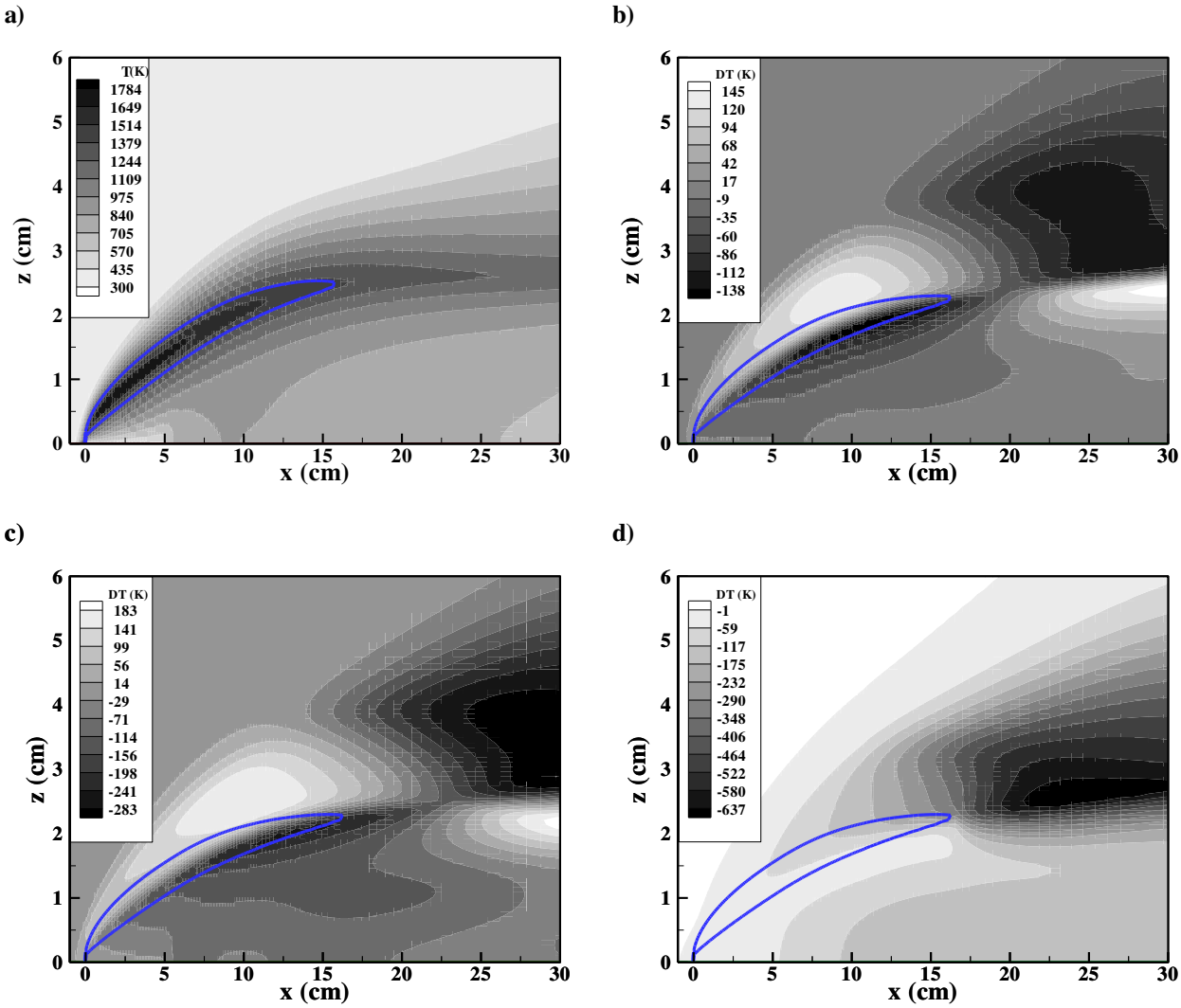

Figure 4-18: Distributions of the reference temperature distribution and temperature error predicted using approximate radiation models, (a) temperature distribution of the reference model, (b) error of the Gray soot, (c) error of the Planck mean, and (d) error of OTA.

Figure 4-19 display the distributions of the relative error for the soot volume fraction. The same definition of the relative error as Liu and coworkers (Liu, Guo, and Smallwood 2004) is adopted:

$$E_{r,f_S} = \left(f_{S,\mathrm{model}} - f_{S,ref} \right) / f_{S,\max} \tag{4.24}$$

Where $f_{s,\max}$ is the maximum value of the soot volume fraction over the entire computational domain. An analysis of the mechanism leading to soot formation in laminar boundary layer flame has revealed that soot was produced in a region following the stand-of distance. The soot particles were then transported along streamlines inside the boundary layer by convection and thermophoresis Figure 4-14a (Legros et al. 2009). As a consequence, the distribution of soot inside the boundary layer depends on both the soot formation processes and the flow dynamic. Previous results have shown that the use of approximate radiative models affects, on one hand, the temperature field which has a direct influence on the soot production processes and, on the other hand, the flame geometry which influences the flow dynamic. As a consequence, the relative error on soot volume fraction results from these two effects.

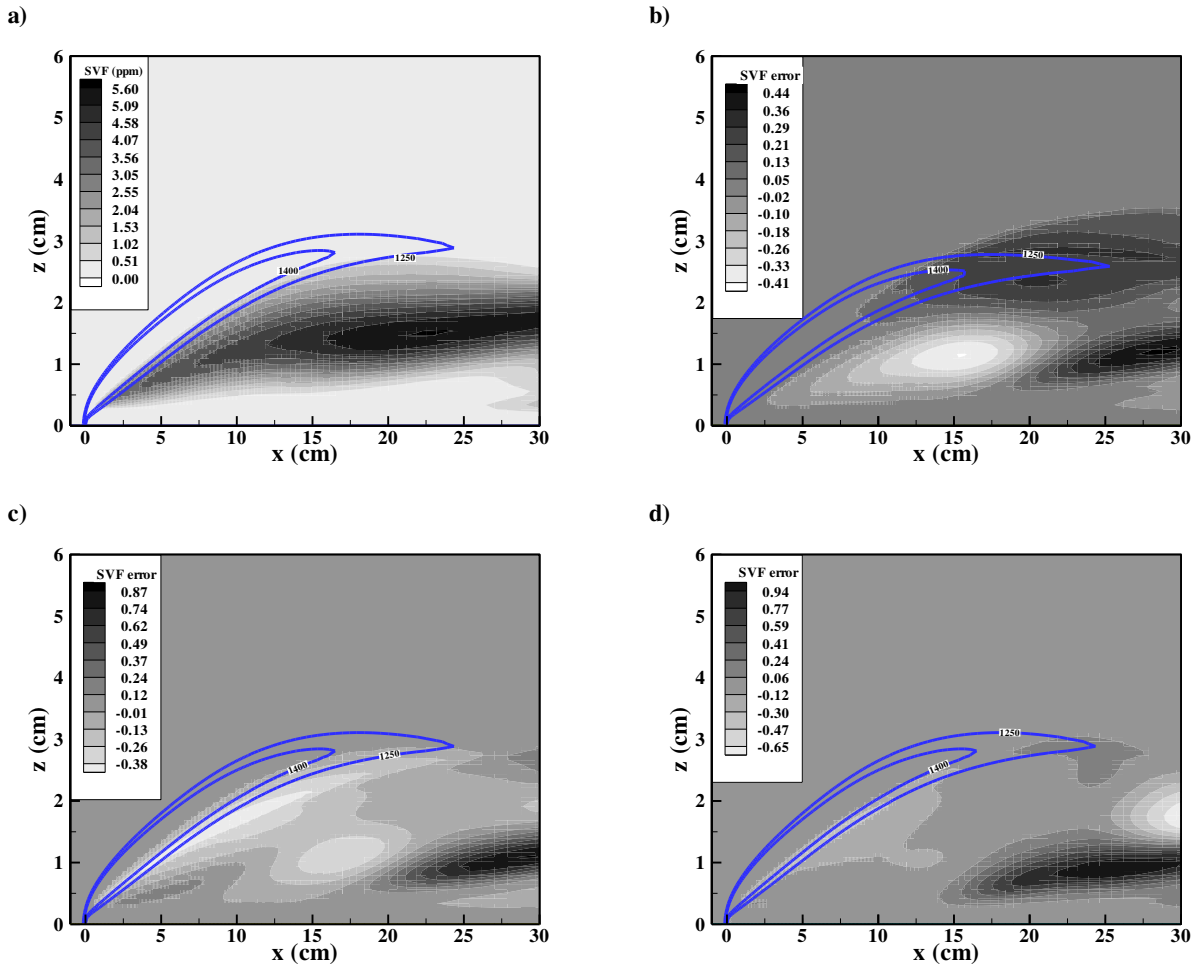

Figure 4-19: Distributions of the reference soot volume fraction the relative error of soot volume fraction, (a) soot volume fraction distribution of reference model, (b) Gray soot, (c) Planck mean and, (d) OTA.

Figure 4-19 b) to d), show the relative error in soot volume fraction predicted by the gray soot model, the Planck mean model, and the OTA, respectively. These figures indicate that the distributions of the relative error are similar. These simplified radiation models significantly overpredict the soot volume fraction in most of the region where soot is located, with the maximum relative error being 44%, 87%, and 94% for the gray soot, Planck mean and OTA models, respectively. However, beyond the flame tip (temperature contour of 1400K) and just below the stand-off distance, these approximate models lead to a substantial underprediction of the soot volume fraction, with the maximum relative error being 53%, 84%, and 89% for the gray soot, Planck mean, and OTA models, respectively.

4.3. Concluding remarks

Laminar boundary layer diffusion flames (LBLDFs) generated by a burner of ethylene and characterized by fuel velocities of 3, 4 and 5 mm/s and oxidizer velocities of 250 and 300 mm/s have been numerically investigated. The following conclusions can be drawn:

- Model results are in line with the experimental data in terms of stand-off distance and soot volume fraction. Soot volume fraction and integrated soot volume fraction are predicted within a factor of 3 of measurements, which is consistent with the recognized accuracy of current advanced soot production models (Mehta, Haworth, and Modest 2009). It should be pointed out that the simulations have been run by maintaining unchanged the constant of the soot model used in axi-symmetric laminar co-flow diffusion flames at normal gravity (Dworkin et al. 2011). In addition, the influence of fuel and oxidizer velocities on both flame structure and soot production is correctly reproduced by the model.
- A qualitative understanding of the manner in which the soot is produced has been provided: soot is formed in a region following the stand-off distance where OH, H and pyrene are located and is transported inside the boundary layer by convection and thermophoresis. This description complements that provided in (Fuentes, Legros, Claverie, et al. 2007) and (Fuentes 2006) based only on experimental results.
- The open tip nature of these flames has been evidenced numerically with combustion efficiency significantly lower than unity. It has been also evidenced that the flame

quenching at the trailing edge results from enhanced radiative loss owing to low residence times.

- The radiant fractions are substantially higher than those observed in normal gravity flames as a result of significantly higher residence times. In addition, the radiant fraction decreases as the fuel flow rate increases which is contrary to what is usually observed in closed-tip flames. This may be a characteristic of open-tip flames.
- Neither the radiative contribution of soot nor the radiative contribution of gaseous species can be neglected. In addition, the use of approximate radiative models based on the OTA or gray approximations for soot and/or radiatively participating gas species leads to inaccurate predictions for soot production, flame structure and flame quenching at the trailing edge.

5. Conclusions and perspectives

The first aim of the work was to develop an advanced numerical tool in order to simulate soot production, radiative heat transfer and the flame quenching process at the flame tip in laminar diffusion flames. Comprehensive chemical mechanisms able to predict the production of PAH up to pyrene (A_4) have been used. An exhaustive soot production model based on PAH and including inception through the collision of two pyrene molecules, surface growth through the HACA process, growth of soot particles through PAH condensation, oxidation by OH and O_2 and particle coagulation has been implemented. Flame quenching at the trailing edge depicts a situation where the chemical reactions cool and unreactive mixing occurs. A description of this situation requires a direct coupling between the flow and the chemistry and conservation equations for all the gaseous species have to be considered. These equations are closely coupled and have then to be solved in a fully coupled fashion at each control volume using a direct solver to ensure the convergence process. This requires significant computational resources, especially when large chemical mechanisms containing a significant amount a species and reactions have to be considered, nowadays limiting the use of the model to 2D configurations. The radiative model is based on the statistical narrow-band-correlated K (SNBCK)-based wide-band model to compute the radiative properties of CO, CO_2, and H_2O, on the Rayleigh theory to compute the radiative property of the soot and on the Discrete Ordinates Method to solve the radiative transfer equation.

The model was first applied to simulate axi-symmetric ethylene laminar co-flow diffusion flames burning under different oxygen index. The experimental data were taken from works developed in the University Federico Santa Maria at Valparaiso (Chile). Model predictions in term of soot production were found in line with the experiments and the main effects of oxygen index on soot production were captured.

Once model was tested, laminar boundary layer diffusion flames in microgravity were considered. A first part of this section was devoted to the analysis of the experimental data obtained during the PhD thesis of Andrés Fuentes at the ENSMA at Poitiers (France). This analysis focused of stand-off distance, flame length and soot production and the influence of fuel velocity, oxidizer velocity, and oxygen index. The analysis of stand-off distance revealed that the flame can be divided into three part: a region dominated by inertia where the stand-off distance

increase with x, a region dominated by diffusion where the stand-of distance increases with $x^{1/2}$ as expected from the laminar boundary layer theory and a region located after the burner where three dimensional effects appear. It was found that these flames behave differently than "closed-tip" diffusion flames for which the fuel is completely burnt at the flame tip. In particular, the flame length increases with the oxidizer velocity, the inverse trend being expected in the case of "closed-tip" flame. This behavior occurs because the flame length is controlled by radiant extinction at the flame trailing edge. The radiative extinction exists only in the presence of radiative heat loss, and occurs at long residence times (large *Da*). While the increase of *Da* enhances reaction, the energy loss through radiation causes a decrease in flame temperature and renders a reduction of the reaction rate. Extinction takes
place when excess heat loss significantly lowers the reaction rate such that the flame can no longer sustain itself. In such situation the flame length was found to be no longer a relevant quantity to define the soot formation residence time. The soot formation residence time was redefined by using the distance between the burner leading edge and the location of the peak of soot volume fraction, to allow interpreting the effects of the oxygen index on the characteristic time scale for soot production. Numerical simulations were performed in the case of an oxygen index of 21% and for three fuel velocities and two oxidizer velocities. Numerical results were found in reasonable agreement with the experimental data in terms of stand-off distance and soot volume fraction. The numerical results were firstly used to complete the experimental data. In particular a better understanding of the structure of the flame was provided: H and OH radicals, responsible of the de-hydrogenation of sites in the HACA process, and Pyrene, at the origin of inception and PAH condensation processes, were found to be located in a thin region that follows the stand of distance in the fuel rich part of the flame. Soot is produced in this region and then it is transported inside the boundary layer by convection and thermophoresis. In addition, numerical results confirmed that these flames belong to the category of "open-tip" flames and that radiative loss is responsible of the flame quenching process observed at the trailing edge. They are characterized by radiant fractions significantly higher than those observed in axi-symmetric laminar diffusion flames at normal gravity owing to longer residence time. Finally, the capability of approximate radiative property models such as the optically-thin approximation or models based on the gray approximation were assessed, showing that none of these approximations are

sufficient to predict accurately flame structure, soot production and flame quenching at the trailing edge.

The perspectives of this work are numerous:

- The first perspective is to simulate the laminar boundary layer diffusion flames in microgravity reported in the experimental section and that have not been investigated numerically. This will allow in particular evaluating the effects on the oxygen index on soot formation and radiative quenching.
- The numerical model developed in the present study is promising. It can be applied to heavier fuels of interest in practical applications such as, for example, the blends of iso-octane/n-heptane/toluene used as surrogate for gasoline or biofuel.
- However, it is very time consuming on the computational point of view and calculations in three dimensional configurations are today unfeasible. Several improvements can be made to improve this point. The first solution is to develop a parallel version of the code. In addition, the resolution of the transport equations of species mass fraction represent today the most important part of the computational time. The development of reduced chemical reaction mechanism have been undertaken in the case of large chemical mechanism involving soot and seem to be reliable (Shaddix et al. 2011). Nevertheless, despite these efforts, the simulation of three dimensional configurations with such detailed models is likely out of reach in the near future. It is then desirable to imagine experimental configurations that exhibit a two-dimensional behavior.
- The size distribution of soot particles is treated in a simplified manner in the present simulations. Only the two first moment of the particle size distribution are computed, i.e. number density and soot volume fraction. As a consequence, the primary soot particles are assumed to be locally mono-disperse and the model provides no information about the soot aggregates of primary particles. Several methods can be used to improve this point: the sectional method developed by Wang and co-workers give (Q. Zhang et al. 2009), the hybrid method of moments proposed by Muller and co-workers (Mueller, Blanquart, and Pitsch 2009), and the stochastic approach as proposed by Balthasar and Kraft (Balthasar and Kraft 2003). A first analysis of these models suggests that the hybrid method of

moments seems to be the most suitable in terms of accuracy and computational efficiency. However, additional works are required before choosing one of these three methods

Appendix A

Discretization and solution of Radiative Heat Transfer Equation

The radiative heat transfer equation shown in Section 2.1.3.1 has been solved using the discrete ordinate method together with a control volume strategy.

The physical situation to be considered is that of a 2D rectangular domain containing an absorbing-emitting, non-scattering radiatively gray medium whose absorption coefficient is computed taking account radiative gases species (CO_2, CO and H_2O) and soot. Values of black-body emissive power are assumed to be available at all points within the medium and the bounding walls are described by mean a constant temperature and an emission coefficient. The temperatures of the medium are prescribed by the conservation of energy equation presented in Section 2.1.2). Hence the temperature is treated as a known dependent variable in the radiation problem. Figure A-1 shows a schematic diagram of the assumed geometry and coordinates employed.

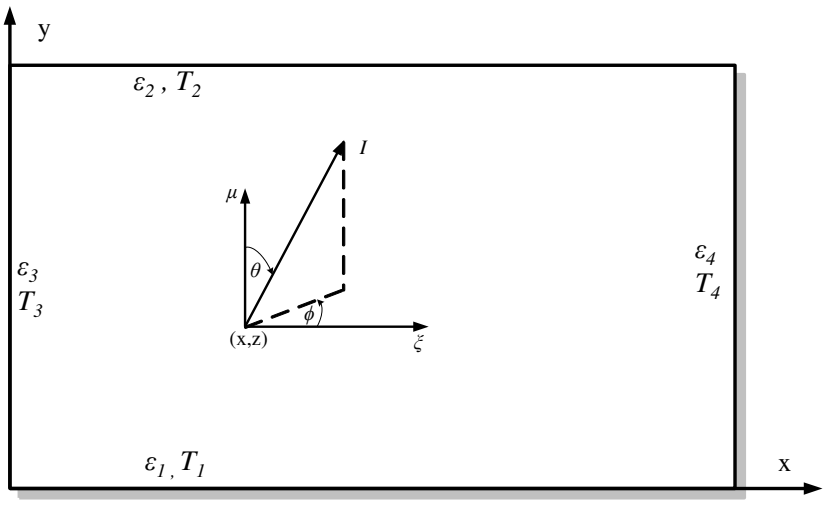

Figure A-1: Schematic of rectangular geometry a) coordinates and boundary properties, and b) definition of the control volume for discretization of the RTE.

The procedure to solve the spectral RTE in present is presented here. First, RTE is solved in a spectral way neglecting scattering.

Thus only emission and absorption have been considered.

$$\frac{dI_\eta}{ds} = \kappa_\eta\left(\underline{\varphi}\right)\left[I_{b\eta}\left(T\right) - I_\eta\right] \tag{A.1}$$

The left hand side of RTE (equation A.1) is to be understood as the variation of intensity in direction *s* along the propagation path for a given wavelength. In rectangular geometries, well described by Cartesian coordinates, this derivative along the path is simply

$$\mu\frac{dI_\eta}{dx} + \xi\frac{dI_\eta}{dy} = \kappa_\eta\left(\underline{\varphi}\right)\left[I_{b\eta}\left(T\right) - I_\eta\right] \tag{A.2}$$

where ε and ξ are cosines directions taken from a T_N quadrature set (Thurgood, Pollard, and Becker 1995). In this study a T_3 quadrature set was used for the angular discretization. The direction cosines and weight functions of the T_3 quadrature in Cartesian coordinates are given in Table A-1.

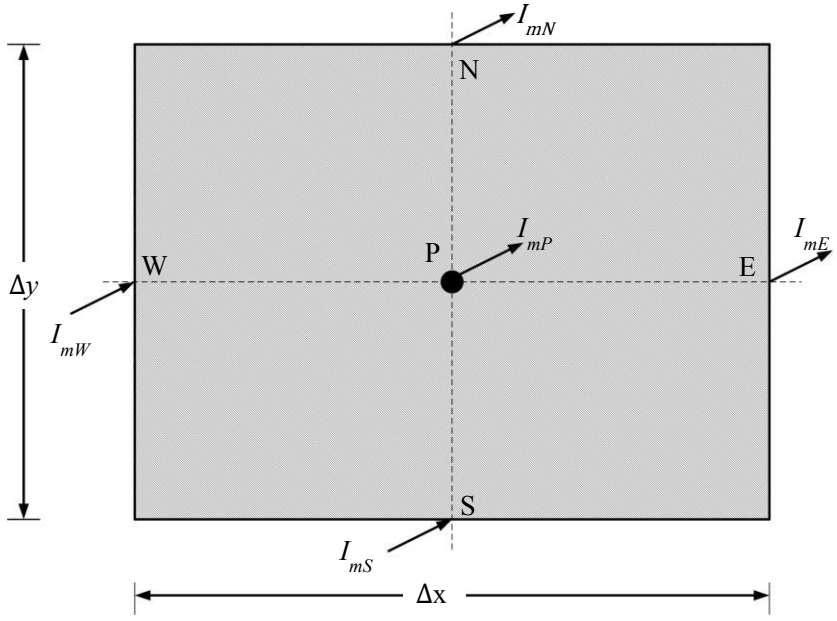

Figure A-2: A general two-dimensional control volume.

In **Erreur ! Source du renvoi introuvable.** the scheme shows a ray with a direction $m(\mu,\xi)$ ormed by a pair of cosine directions and a control volume. The control volume has four areas at four faces, W, E, N and S. In a simple two dimensional rectangular enclosure one would have that the value of every area surface is equal to the distance difference, Δy for west and east sides, and Δx for north and south sides. The finite volume formulation of equation (A.1) is obtaining by integrating it over the volume element of **Erreur ! Source du renvoi introuvable.**. For example, the first term of right side of equation (A.2), $\mu\left(dI_\eta/dx\right)$ transforms to

$$\int_N^S\int_E^W \mu\frac{\partial I_\eta}{\partial x}dxdy=\mu\left(\int_{A_E} I_\eta A_E-\int_{A_W} I_\eta A_W\right)=\mu\Delta y\left[I_{\eta W}-I_{\eta E}\right] \tag{A.3}$$

where $I_{\eta E}$ and $I_{\eta W}$ are average values of I_η over the faces at east and west faces, respectively. Operating similarly on the other terms of equation (A.2) we have:

$$\int_E^W\int_N^S \xi\frac{\partial I_\eta}{\partial y}dydx=\xi\Delta x\left[I_{\eta S}-I_{\eta N}\right] \tag{A.4}$$

$$\int_E^W\int_N^S \kappa_\eta\left(\underline{\phi}\right)\left[I_{b\eta}\left(T\right)-I_\eta\right]dydx=\kappa_\eta\left(\underline{\phi}\right)\Delta x\Delta y\left[I_{b\eta}\left(T\right)-I_{P\eta}\right] \tag{A.5}$$

Finally, the discrete form the radiative heat transfer equation for an absorbing-emitting non-scattering medium along an angular direction (*m,l*) can be written as :

$$\varepsilon\Delta y\left[I_{m,W}-I_{m,E}\right]+\xi\Delta x\left[I_{m,S}-I_{m,N}\right]=\kappa_\eta\left(\underline{\phi}\right)\Delta x\Delta y\left[I_b\left(T\right)-I_P\right] \tag{A.6}$$

where I_P is the cell-center intensity and $I_{m,W}$, $I_{m,E}$, $I_{m,S}$ and $I_{m,N}$ are the intensities at each face of the control volume. In last equation, for the sake of clarity, subscript η, associated with wavelength is omitted. The number of unknowns in equation (A.6) may be reduced by relating cell-edge intensities to the volume-average intensity. A common practice in DOM is to assume that intensity at the nodal point is a simple weighed average of the upstream and downstream (along the discretized direction considered) surface values (Fiveland 1984):

$$I_P = fI_{down} + (1-f)I_{up} \tag{A.7}$$

where f is a finite-difference weighting factor taking a value of 0.5 or 1, referring to central and upwind differences schemes, respectively. To take in account all directions of radiation, the procedure need to be performed in four quadrants. Here only first quadrant, both cosine directions are positive, is developed. Thus, from equation (A.7) we have.

$$I_{m,p} = fI_{m,E} - \left(1-f\right) I_{m,W} \tag{A.8}$$

$$I_{m,p} = fI_{m,N} - \left(1-f\right) I_{m,S} \tag{A.9}$$

Rearranging last two equations results in

$$I_{m,E} = \frac{1}{f} I_{m,P} - \frac{\left(1-f\right)}{f} I_{m,W} \tag{A.10}$$

$$I_{m,N} = \frac{1}{f} I_{m,P} - \frac{\left(1-f\right)}{f} I_{m,S} \tag{A.11}$$

Substitution of equation of equations (A.10) and (A.11) into equation (A.6) and rearranging for $I_{m,P}$ we obtain:

$$I_P = \frac{\Delta y \Delta x \kappa I_b + \mu \Delta y I_e \left[1 + \left(1-f\right)/f\right] + \xi \Delta x I_s \left[1 + \left(1-f\right)/f\right]}{\Delta y \Delta x \kappa + \mu \frac{\Delta y}{f} + \xi \frac{\Delta x}{f}} \tag{A.12}$$

This equation is solved for all control volumes, in every angular direction and for all wavelengths.

Table A-1: The T_3 quadrature set in the Cartesian geometry.

m	l	μ	η	ξ	w/2π
1	1	-0.98020	-0.14003	0.14003	0.11134
1	2	-0.98020	0.14003	0.14003	0.11134
2	1	-0.87039	-0.34816	0.34816	0.20613
2	2	-0.87039	0.34816	0.34816	0.20613
3	1	-0.69631	-0.17408	0.69631	0.20613
3	2	-0.69631	-0.69631	0.17408	0.20613
3	3	-0.69631	0.17408	0.69631	0.20613
3	4	-0.69631	0.69631	0.17408	0.20613
4	1	-0.34816	-0.34816	0.87039	0.20613
4	2	-0.34816	-0.87039	0.34816	0.20613
4	3	-0.34816	0.34816	0.87039	0.20613
4	4	-0.34816	0.87039	0.34816	0.20613
5	1	-0.17408	-0.69631	0.69631	0.20613
5	2	-0.17408	0.69631	0.69631	0.20613
6	1	-0.14003	-0.14003	0.98020	0.11134
6	2	-0.14003	-0.98020	0.14003	0.11134
6	3	-0.14003	0.14003	0.98020	0.11134
6	4	-0.14003	0.98020	0.14003	0.11134
7	1	0.14003	-0.14003	0.98020	0.11134
7	2	0.14003	-0.98020	0.14003	0.11134
7	3	0.14003	0.14003	0.98020	0.11134
7	4	0.14003	0.98020	0.14003	0.11134
8	1	0.17408	-0.69631	0.69631	0.20613
8	2	0.17408	0.69631	0.69631	0.20613
9	1	0.34816	-0.34816	0.87039	0.20613
9	2	0.34816	-0.87039	0.34816	0.20613
9	3	0.34816	0.34816	0.87039	0.20613
9	4	0.34816	0.87039	0.34816	0.20613
10	1	0.69631	-0.17408	0.69631	0.20613
10	2	0.69631	-0.69631	0.17408	0.20613
10	3	0.69631	0.17408	0.69631	0.20613
10	4	0.69631	0.69631	0.17408	0.20613
11	1	0.87039	-0.34816	0.34816	0.20613
11	2	0.87039	0.34816	0.34816	0.20613
12	1	0.98020	-0.14003	0.14003	0.11134
12	2	0.98020	0.14003	0.14003	0.11134

Discrete-ordinates method in axisymmetric cylindrical geometry

The spectral RTE in axisymmetric cylindrical coordinates is written as :

$$\frac{\mu}{r}\frac{\partial r I_\nu}{\partial r} - \frac{1}{r}\frac{\partial \eta I_\nu}{\partial \varphi} + \xi\frac{\partial I_\nu}{\partial z} = -\kappa_\nu I_\nu + \kappa_\nu I_{b\nu} \qquad \text{(A.13)}$$

where μ, η and ξ are direction consines and are related to the polar angle (θ) and azimuthal angle (φ) through $\mu = \sin\theta\cos\varphi$, $\eta = \sin\theta\sin\varphi$, and $\xi = \cos\theta$. The symbols I_v, I_{bv} and κ_v denote spectral intensity, spectral blackbody intensity, and the spectral absorption coefficient, respectively. For the sake of clarity, subscript v, associated with wavenumber-dependent quantities, is omitted in the following description of DOM. The discrete ordinate form of Eq. (1) along an angular direction defined by the subscript (m,l) can be written as

$$\frac{\mu_{m,l}}{r}\frac{\partial r I_{m,l}}{\partial r} - \frac{1}{r}\left(\frac{\alpha_{m,l+1/2} I_{\mathrm{m},l+1/2} - \alpha_{m,l-1/2} I_{\mathrm{m},l-1/2}}{\omega_{m,l}}\right) + \xi_{m,l}\frac{\partial I_{m,l}}{\partial z} = -\kappa I_{m,l} + \kappa I_b \tag{A.14}$$

where m is the polar angle from 1 to M and l is the azimuthal angle index from 1 to L(m). Note that the upper limit of l is a function of m. The quantity ωm,l is the weigth function associated with the direction defined by (m,l). The coefficients αm,l+1/2 are determined from the following recurrence relation:

$$\alpha_{m,l+1/2} = \alpha_{m,l-1/2} + \omega_{m,l}\mu_{m,l} \quad l = 1,\ 2,..., L(m), \text{ and } \alpha_{\mathrm{m},1/2}=0. \tag{A.15}$$

The following linear relation was used to link $I_{m,l+1/2}$ to $I_{m,l}$ and $I_{m,l-1/2}$

$$I_{m,l+1/2} = 2I_{m,l} - I_{m,l-1/2}, \quad l = 1,..., L(m) \tag{A.16}$$

where the initials values of $I_{m,1/2}$ are calculated from the transfer equation in the special directions $\eta_{m,1/2}$=0. The transfer equation in these special directions is given as

$$\frac{\mu_{m,1/2}}{r}\frac{\partial r I_{m,1/2}}{\partial r} - \frac{1}{r}\mu_{m,1/2}\,\mathrm{I}_{m,1/2} + \xi_{m,1/2}\frac{\partial I_{m,1/2}}{\partial z} = -\kappa I_{m,1/2} + \kappa I_b \tag{A.17}$$

where

$$\mu_{m,1/2} = -\sqrt{1-\xi_{m,1}^2}, \quad \xi_{m,1/2} = \xi_{m,1} \tag{A.18}$$

In deriving Eq (5) from Eq (1), the relation

$$\frac{\partial \eta I}{\partial \varphi} = I\frac{\partial \eta}{\partial \varphi} + \eta\frac{\partial I}{\partial \varphi} = \mu I + \eta\frac{\partial I}{\partial \varphi} \tag{A.19}$$

was used. In this study, the T3 quadrature ser was used for the angular discretization. The direction cosines and weight functions of the T_3 quadrature in axisymmetric cylindrical coordinates are given in Table 1.

Table A-2: The T_3 quadrature set in the axisymmetric cylindrical geometry (M = 12)

m	l	μ	η	ξ	$w/2\pi$
1	1	−0.14002801	0.14002801	−0.98019606	0.03544095
1	2	0.14002801	0.14002801	−0.98019606	0.03544095
2	1	−0.34815531	0.34815531	−0.87038828	0.06561286
2	2	0.34815531	0.34815531	−0.87038828	0.06561286
3	1	−0.69631062	0.17407766	−0.69631062	0.06561286
3	2	−0.17407766	0.69631062	−0.69631062	0.06561286
3	3	0.17407766	0.69631062	−0.69631062	0.06561286
3	4	0.69631062	0.17407766	−0.69631062	0.06561286
4	1	−0.87038828	0.34815531	−0.34815531	0.06561286
4	2	−0.34815531	0.87038828	−0.34815531	0.06561286
4	3	0.34815531	0.87038828	−0.34815531	0.06561286
4	4	0.87038828	0.34815531	−0.34815531	0.06561286
5	1	−0.69631062	0.69631062	−0.17407766	0.06561286
5	2	0.69631062	0.69631062	−0.17407766	0.06561286
6	1	−0.98019606	0.14002801	−0.14002801	0.03544095
6	2	−0.14002801	0.98019606	−0.14002801	0.03544095
6	3	0.14002801	0.98019606	−0.14002801	0.03544095
6	4	0.98019606	0.14002801	−0.14002801	0.03544095
7	1	−0.98019606	0.14002801	0.14002801	0.03544095
7	2	−0.14002801	0.98019606	0.14002801	0.03544095
7	3	0.14002801	0.98019606	0.14002801	0.03544095
7	4	0.98019606	0.14002801	0.14002801	0.03544095
8	1	−0.69631062	0.69631062	0.17407766	0.06561286
8	2	0.69631062	0.69631062	0.17407766	0.06561286
9	1	−0.87038828	0.34815531	0.34815531	0.06561286
9	2	−0.34815531	0.87038828	0.34815531	0.06561286
9	3	0.34815531	0.87038828	0.34815531	0.06561286
9	4	0.87038828	0.34815531	0.34815531	0.06561286
10	1	−0.69631062	0.17407766	0.69631062	0.06561286
10	2	−0.17407766	0.69631062	0.69631062	0.06561286
10	3	0.17407766	0.69631062	0.69631062	0.06561286
10	4	0.69631062	0.17407766	0.69631062	0.06561286
11	1	−0.34815531	0.34815531	0.87038828	0.06561286
11	2	0.34815531	0.34815531	0.87038828	0.06561286
12	1	−0.14002801	0.14002801	0.98019606	0.03544095
12	2	0.14002801	0.14002801	0.98019606	0.03544095

The spatial discretization of Eqs. (2) and (5) was achieved using the finite-volume method, which was also used in the flame code for the discretization of mass, momentum, species, and energy

conservation equations. Multiplying Eq. (5) by $2\pi drdz$ and performing integration over the control volume illustrated in Fig. 1 result in

$$\mu_m\left(A_nI_{m,n}-A_sI_{m,s}\right)-\left(A_n-A_s\right)\mu_mI_{m,p}+\xi_m\left(A_eI_{m,e}-A_wI_{m,w}\right)=V\left(-\kappa I_{m,p}+\kappa I_{b,p}\right), \tag{A.20}$$

where

$$A_n=2\pi\left(z_{i+1}-z_i\right)r_{j+1},$$

$$A_s=2\pi\left(z_{i+1}-z_i\right)r_j,$$

$$A_s=2\pi\left(r_{j+1}-r_j\right)\left(r_{j+1}+r_j\right)/2,$$

$$A_w=A_e$$

$$V=2\pi\left(z_{i+1}-z_i\right)\left(r_{j+1}-r_j\right)\left(r_{j+1}+r_j\right)/2$$

are the surface areas of the control volume and the volume under consideration. Subscripts *p, w, e, n,* and *s* denote values at the nodal point p and the west, east, north, and south surfaces, respectively. Note that the subscript 1/2 has been dropped from the above expressions for simplicity. An auxiliary relation between the intensities at the nodal point and at the control volume surfaces must be provided to close the equation system. The intensity at the nodal point was assumed to be a simple weighted average of the upstream and downstream (along the discretized direction considered) surface values, a common practice used in DOM; i.e.,

$$I_{m,p}=f\ I_{m,\text{downstream}}+(1-f)I_{m,\text{upstream}}, \tag{A.21}$$

where $f = 0.5$ and 1 correspond to the central and upwind difference schemes, respectively. Since by definition $\mu_{m,1/2} < 0$, Eq. (6), two situations need to be considered in the calculation of $I_{m,1/2}$: (1) $\mu_{m,1/2} < 0$, $\xi_{m,1/2} < 0$, and (2) $\mu_{m,1/2} < 0$, $\xi_{m,1/2} > 0$. The following formulation is applicable to the first situation. For the second one, the formulation can be similarly derived. For $\mu_{m,1/2} < 0$ and $\xi_{m,1/2} < 0$, calculation starts from the upper right corner of the solution domain and proceeds toward the lower left corner in the coordinates defined in Fig. 1. The intensities at the north and east surfaces are treated as known (from the boundary conditions) and Eq. (9) in this case reads as

$$I_{m,p} = f\ I_{m,s} + (1-f) I_{m,n},$$
$$I_{m,p} = f\ I_{m,w} + (1-f) I_{m,e},$$
(A.22)

rearranging Eq. 10 results in

$$I_{m,s} = \frac{1}{f}\ I_{m,p} + \frac{1-f}{f} I_{m,n},$$
$$I_{m,w} = \frac{1}{f}\ I_{m,p} + \frac{1-f}{f} I_{m,e},$$
(A.23)

substitution of Eq. (11) into Eq. (8) leads to

$$I_{m,p} = \frac{\left(\kappa V I_{b,p} - \mu_m \left(A_n + \frac{A_s (1-f)}{f} \right) I_{m,n} - \xi_m \left(A_e + \frac{A_w (1-f)}{f} \right) I_{m,e} \right)}{\left(\kappa V - \frac{\mu_m A_s}{f} - \mu_m (A_n - A_s) - \frac{\xi_m A_w}{f} \right)}$$
(A.24)

For the second case of $\mu_{m,1/2} < 0$ and $\eta_{m,1/2} > 0$, the calculation starts from the upper left corner and proceeds toward the lower right corner and the values at the west and north surfaces are known. Expressions similar to Eqs. (11) and (12) can be derived for the calculation of the nodal and downstream surface intensities.

The spatial discretization of Eq. (2) using the control volume method discussed above for Eq. (5) is performed similarly. Again, the expressions used to calculate the intensities at the nodal point and downstream surfaces are dependent on the signs of the direction cosines. The following expressions are applicable to the situation of $\mu_{m,l} > 0$, $\zeta_{m,l} > 0$

$$I_{m,l,p} = \frac{\left(\kappa V I_{b,p} - \mu_{m,l} \left(A_s + \frac{A_n (1-f)}{f} \right) I_{m,l,s} + \xi_{m,l} \left(A_w + \frac{A_e (1-f)}{f} \right) I_{m,l,w} - \frac{(A_n - A_s)(\alpha_{m,l+1/2} + \alpha_{m,l-1/2})}{w_{m,l} I_{m,l-1/2,p}} \right)}{\left(\kappa V - \frac{\mu_{m,l} A_n}{f} + \frac{\xi_{m,l} A_e}{f} - \frac{2(A_n - A_s)\alpha_{m,l+1/2}}{w_{m,l}} \right)}$$

(A.25)

$$I_{m,l,n} = \frac{1}{f}\ I_{m,l,p} - \frac{1-f}{f} I_{m,l,s},$$
$$I_{m,l,e} = \frac{1}{f}\ I_{m,l,p} - \frac{1-f}{f} I_{m,l,w},$$
$$I_{m,l+1/2,p} = 2I_{m,l,p} - I_{m,l-1/2,p} \qquad \text{(A.26)}$$

Assuming the surfaces are diffusely emitting and reflecting, the boundary conditions at the $z = 0$, $z = L$, and $r = R$ surfaces are given as

$$I_{m,l} = \varepsilon_w I_{bw}(T_w) + (1-\varepsilon_w) q_{in} / \pi \qquad \text{(A.27)}$$

where qin is the incident heat flux and ε_w and T_w are the wall emissivity and wall temperature, respectively. The boundary condition at the centerline is given as

$$I_{m,l} = I_{m,l'} \quad \text{where } \mu_{m,l} = -\mu_{m,l'} \text{ and } \mu_{m,l} > 0 \qquad \text{(A.28)}$$

Appendix B

Soot model development

The soot model used in present thesis was developed initially by (M. Frenklach and Wang 1991) and consists of three logical parts: (I) initial PAH formation, which includes a detailed chemical kinetic description of acetylene pyrolysis and oxidation, formation of the first aromatic ring, and its subsequent growth to a prescribed size; (II) *planar PAH growth,* comprised of replicating-type growth of PAHs beyond the prescribed size; and (III) spherical particle formation and growth, consisting of coagulation of PAHs formed in part (II) followed by the growth of resulting particles by coagulation and surface reactions.

B.1 Initial PAH formation.

The chemical reaction mechanism for the initial PAH formation is the 94 species and 723 reactions based on mechanism developed by Slavinskaya (Slavinskaya and Frank 2009). It mechanism was developed to predict the formation of PAH and their growth of up to five aromatic rings in methane and ethane-fueled flames. The formation of the first ring is a critical part of PAH and soot formation. All now reasonably well-established routes from small aliphatic molecules to first aromatic rings were included in consideration:

H2CCCH + H2CCCH = A1 (benzene, C_6H_6)

H2CCCH + H2CCCH = A1- + H

H2CCCCH + C_2H_3 = (n-C_6H_6) → A1

H2CCCCH + C_2H_3 = A1- + H

H2CCCH + C_3H_4 = A1 + H

C_4H_4 + C_2H_3 = (n-C_6H_7 → c-C_6H_7) → A1 + H

H2CCCH + C_2H_2 = A1- + H

C_4H_5 + C_2H_2 = (n-C6H7) → A1 + H

C_4H_5 + C_2H_3 = A1 + H_2

C_4H_5 + C_2H = A1

C_4H_5 + C_2H = A1- + H

B.2 Planar growth and coagulation

Once formed, aromatic rings grow by a sequential two-step process: H-abstraction which activates the aromatic molecules, and C_2H_2-addition which propagates molecular growth and cyclization of PAH as shown in scheme of Figure B-1.

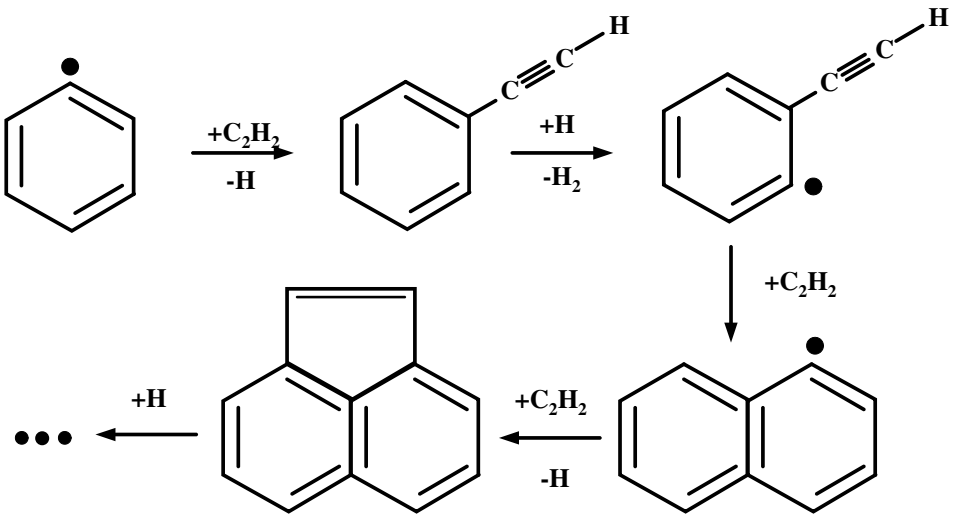

Figure B-1: H-abstraction-C2H2-addition reaction pathway of PAH growth (M Frenklach and Wang 1994)

This process is called HACA and works like this: during the high-temperature, high-pressure environment of combustion, a simple ring of six carbon and six hydrogen atoms, called benzene (A_1), would lose one of its hydrogen atoms, allowing another two-carbon molecule called acetylene (C_2H_2), to attach to the ring, giving it a kind of tail. Then the acetylene tail would lose one of its hydrogen atoms so another acetylene could link up in, doubling the carbon atoms in the tail to four.

Next, the tail would curl around and attach to the original ring, creating a double-ring structure called naphthalene. Link by link, ring by ring, these molecules would continue to grow in an unwieldy, crumpled way until they became the macromolecules that we recognize as soot.

B.3 Spherical particle formation

Particle inception is the least understood process of soot formation in hydrocarbon combustion. It is widely accepted that gaseous precursors to solid soot particles are polycyclic aromatic hydrocarbons (PAH) (Michael Frenklach 2002; McEnally et al. 2006; Miller, Pilling, and Troe 2005; Richter and Howard 2000; Schuetz and Frenklach 2002). However, the understanding of this transformation in mechanistic terms is far from complete. The state of the art of nucleation modeling is to assume soot nucleates through the collision and sticking of PAH species to form a "dimmer", and in present work, Pyrene (A_4) is assumed to be the only nucleation PAH species. Thus, mass nucleation rate (R_1), in (gr/cm3/s) is defined as:

$$R_1 = 2 N_{c,A_4} m_c R_0 \tag{B.1}$$

where N_{c,A_4} is the number of carbon atoms in the nucleation PAH species (16 for Pyrene), m_c is the mass of carbon atom; in present work it was considered as 12 x AMU (where AMU is equal to 1.6710^{-24} g). R_0 corresponds to soot particle nucleation rate (particles/cm3/s) who is developed using the collision theory. First we state the Maxwell-Boltzmann distribution of molecular speed as (Kee, Coltrin, and Glarborg 2003):

$$P\left(v_{rel}\right) = 4\pi \left(\frac{m}{2\pi k_B T} \right)^{3/2} v_{rel}^2 e^{-m_{12} v_{rel}^2 / (2 k_B T)} \tag{B.2}$$

from this equation, the average molecular speed is calculated as $v = \int_0^\infty v P(v)\, dv$ and after integration, we obtain

$$\left\langle v_{rel} \right\rangle = \left(\frac{8 k_B T}{m_{12} \pi} \right)^{1/2} \tag{B.3}$$

The rate at which chemical reactions occur depends (among other things) on the rate at which molecules collides with one another. If well our case is a collision between like molecules, the derivation of collision rate between gas-phase unlike molecules must to be addressed. Before deriving the expressions for gas-phase collision frequency, we need to discuss the relative

velocity that is important in collisions. The reduced mass m_{12} is also obtained from this analysis, and will be the appropriate mass to use in the Maxwell-Boltzmann expression for collision velocities.

In the laboratory frame of reference, the kinetic energy of two molecules, 1 and 2, translating through the gas is:

$$E_k = \frac{1}{2} m_1 \mathbf{v_1} \bullet \mathbf{v_1} + \frac{1}{2} m_2 \mathbf{v_2} \bullet \mathbf{v_2} \tag{B.4}$$

$$E_k = \frac{1}{2} m_1 \dot{\mathbf{x}}_\mathbf{1} \bullet \dot{\mathbf{x}}_\mathbf{1} + \frac{1}{2} m_2 \dot{\mathbf{x}}_\mathbf{2} \bullet \dot{\mathbf{x}}_\mathbf{2} \tag{B.5}$$

The position of the center of mass of the pair of molecules is

$$\vec{\mathbf{X}} = \frac{1}{M}\left(m_1 \mathbf{x_1} + m_2 \mathbf{x_2}\right) \tag{B.6}$$

where M is the total mass, $M=m_1+m_2$. A vector giving the position of atom 2 relative to atom 1 is defined as $\xi = \mathbf{x_2} - \mathbf{x_1}$. The the reduced mass, of the collision pair is defined as

$$m_{12} = \frac{m_1 m_2}{m_1 + m_2} \tag{B.7}$$

Using the definitions of $\mathbf{X}, \xi, M$ and m_{12} we can verify that

$$E_k = \frac{1}{2} M \dot{\mathbf{X}} \bullet \dot{\mathbf{X}} + \frac{1}{2} m_{12} \dot{\xi} \bullet \dot{\xi} \tag{B.8}$$

$$E_k = \frac{1}{2} M v_{cm}^2 + \frac{1}{2} m_{12} v_{rel}^2 \tag{B.9}$$

Finally, the distribution of relative velocities obeys the Maxwell-Boltzmann distribution of Eq. XX, with the mass replaced by the reduced mass m_{12}:

$$P\left(v_{rel}\right) = 4\pi \left(\frac{m_{12}}{2\pi k_B T} \right)^{3/2} v_{rel}^2 e^{-m_{12} v_{rel}^2 / \left(2 k_B T\right)} \tag{B.10}$$

And finally, as was done before, the average relative speed is:

$$v_{rel} = \left(\frac{8k_B T}{\pi m_{12}} \right)^{1/2} \tag{B.11}$$

Collision between molecules

The frequency of molecular collisions is an important factor governing gas-phase reaction rates. Consider two "rigid" molecules of radius r_1 and r_2. If we follow the motion of a particular molecule of type 1 traversing through a great number of type 2 molecules, whenever the distance between 1 and 2 is less than $r_1 + r_2$ a collision occurs. If the relative velocity is v_{rel}, then in a time Δt molecule 1 sweeps out a cylinder of volume:

$$\forall = \pi \left(r_1 + r_2 \right)^2 v_{rel} \Delta t \tag{B.12}$$

introducing the "1-2 collision cross section" $\sigma_{1,2}$, we write

$$\sigma_{1,2} = \pi \left(r_1 + r_2 \right)^2 \tag{B.13}$$

Finally the volume swept out is

$$\forall = \sigma_{1,2} v_{rel} \Delta t \tag{B.14}$$

The number of type 2 molecules within the volume $\forall$ is proportional to concentration $\left[c_2 \right]$, the number of 2 molecules per unit volume. Thus the number of 1-2 collision within the time Δt is $\left[c_2 \right] \sigma_{1,2} v_{rel} \Delta t$ so the number of collisions per unit time (i.e. the collision rate or collision frequency) for this relative velocity is

$$z_{1,2} \left(v_{rel} \right) = \left[c_2 \right] \sigma_{1,2} v_{rel} \Delta t \tag{B.15}$$

There is a Maxwell-Boltzmann distribution of collision velocities, given by Eq. 18, so to obtain the average collision frequency integrate eq. 31 over all possible collision velocities

$$z_{1,2} = [c_2] 4\pi \left(\frac{m}{2\pi k_B T} \right)^{3/2} \int_0^\infty \sigma_{1,2} v_{rel}^3 e^{-m v_{rel}^2/(2k_B T)} dv_{rel} \tag{B.16}$$

$$z_{1,2} = [c_2] \sigma_{1,2} \left(\frac{8k_B T}{\pi m_{1,2}} \right)^{1/2} \tag{B.17}$$

$$z_{2,1} = [c_1] \sigma_{1,2} \langle v_{rel} \rangle \tag{B.18}$$

with $\langle v_{rel} \rangle$ given by Eq. 27. This is the average frequency of collisions that a type 1 molecule undergoes. Since $\sigma_{1,2} = \sigma_{2,1}$ the average collision frequency of a type 2 molecule with type 1 molecules is

$$z_{1,2} = [c_2] \sigma_{1,2} v_{rel} \tag{B.16}$$

The total number of 1-2 collisions per unit volume per unit time is then $z_{1,2}$ times the concentration of type 1 molecules

$$Z_{1,2} = [c_1][c_2] 4\pi \left(\frac{m_{12}}{2\pi k_B T} \right)^{3/2} \int_0^\infty \sigma_{1,2} v_{rel}^3 e^{-m_{12} v_{rel}^2/(2k_B T)} dv_{rel} \tag{B.17}$$

$$Z_{1,2} = [c_1][c_2] \sigma_{1,2} \langle v_{rel} \rangle \tag{B.18}$$

The derivation of collision frequency for two unlike molecules ($Z_{1,2}$) done up here must be extrapolated to the collision of between identical molecules (i.e. $Z_{1,1}$). The frequency of collision between a molecule and others of the same chemical species (i.e., 1-1 or 2-2 collisions) is similar to Eq. 35, with a few correction terms. Starting with Eq. 35, we have:

$$z_{1,1} = [c_1] \sigma_{1,1} v_{rel} \tag{B.19}$$

where collision cross section and reduced mass are computed as:

$$\sigma_{1,1} = \pi\left(2r_1\right)^2 \tag{B.20}$$

$$m_{11} = \frac{m_1 m_1}{m_1 + m_1} = \frac{1}{2} m_1 \tag{B.21}$$

The average relative velocity of Eq. XX becomes

$$\left\langle v_{rel} \right\rangle = \left(\frac{8k_B T}{\pi m_{11}} \right)^{1/2} \tag{B.22}$$

$$\left\langle v_{rel} \right\rangle = \sqrt{2} \left(\frac{8k_B T}{\pi m_1} \right)^{1/2} \tag{B.23}$$

$$\left\langle v_{rel} \right\rangle = \sqrt{2} \left\langle v \right\rangle \tag{B.24}$$

where $\left\langle v \right\rangle$ is the average velocity computed in Eq. XX. Thus, the 1-1 collision frecuency for any given molecule is:

$$z_{1,1} = \left[c_1\right] \sigma_{1,1} \sqrt{2} \left\langle v \right\rangle \tag{B.25}$$

The total number of 1-1 collisions per unit volume per unit time is not quite the product of $z_{1,1}$ and $\left[c_1\right]$; this product would overcount the collisions by a factor of 2, so

$$Z_{1,1} = \frac{1}{2} \left[c_1\right]^2 \sigma_{1,1} \sqrt{2} \left\langle v \right\rangle \tag{B.26}$$

or

$$Z_{1,1} = \left[c_1\right]^2 \sigma_{1,1} \frac{\left\langle v \right\rangle}{\sqrt{2}} \tag{B.27}$$

$$Z_{1,1} = \left[c_1\right]^2 \sigma_{1,1} \left(\frac{4k_B T}{\pi m_1} \right)^{1/2} \tag{B.28}$$

For the case where two pyrene molecules collision, the particles formed per unit volume and per unit time can be written as:

$$R_{in} = \frac{1}{2} N_{A_4}^2 \left(\frac{8k_B T}{\pi m_{A_4}} \right)^{1/2} \pi \left(2r_{A_4} \right)^2 \tag{B.29}$$

$$R_{in} = N_{av}^2 \left[A_4\right]^2 \left(\frac{4k_B T}{\pi m_{A_4}} \right)^{1/2} \pi \left(d_{A_4} \right)^2 \tag{B.30}$$

Finally, to compute the soot particle formation rate, the addition of an enhancement coefficient must to be done to take in account the Vander Wall Forces as was suggested by (Harris and Kennedy 1988)

$$R_0 = 2.2 N_{av}^2 \left[A_4\right]^2 \left(\frac{4\pi k_B T}{m_{A_4}} \right)^{1/2} \left(d_{A_4} \right)^2 \tag{B.31}$$

It was assumed that the diameter of A_4 is related to content of carbon atom according to (Lindstedt 1994) :

$$d_{A_4} = 1.395 \sqrt{2N_{c,A_4}} \tag{B.31}$$

B.4 Surface growth and oxidation

While the nucleation kinetics control the number of nascent particles and coagulation controls the evolution of the particle number density, the carbon mass accumulated in soot is determined primarily by surface reactions, growth and oxidation (Haynes and Wagner 1982).

The surface growth was assumed to occur due to reactions of C_2H_2 with surface radicals and condensation of PAH on the particle surface, and the surface oxidation due to reactions of O_2 with surface radicals and reactions of OH with the particle surface (M Frenklach and Wang 1994). The surface reactions of H, C_2H_2 and O_2 were assumed to be analogous, on the per-site

basis, to the corresponding gaseous reactions of PAH species. Table B-1 presents the mechanism of surface reactions and oxidation by OH. The explanation for these changes follows.

Table B-1: HACA-based soot surface growth and oxidation reactions and reactions parameters *for* $k = AT^n \exp(-E/RT)$. $(C_{soot} - H)$ represents an active site on the soot particle surface and $C^{\bullet}_{soot}$ the corresponding radical.

N°	Reaction	A (cm^3/mol/s)	n	E (kcal/mol)
S1	$(C_{soot}\text{-}H) + H \Leftrightarrow C^{\bullet}_{soot} + H_2$	4.2×10^{13}	--	13.0
S2	$(C_{soot} - H) + OH \Leftrightarrow C^{\bullet}_{soot} + H_2O$	1.2×10^{10}	0.734	1.43
S3	$C^{\bullet}_{soot} + H \Rightarrow C_{soot} - H$	2.0×10^{13}	--	
S4	$C^{\bullet}_{soot} + C_2H_2 \Rightarrow C_{soot} - H + H$	8.0×10^{7}	1.56	3.8
S5	$C^{\bullet}_{soot} + O_2 \Rightarrow 2CO + Products$	2.2×10^{12}	--	7.5
S6	$C_{soot} - H + OH \Rightarrow CO + Products$		$\gamma_{OH} = 0.06$	

Reaction of soot oxidation with OH (S6) is modeled based on the formulation of (Fenimore and Jones 1967) and a collision factor $\gamma_{OH} = 0.06$ is considered (Guo et al. 2006). The kinetics of other surface reactions are described using the concept of surface sites (an armchair site on the particle surface), which are carbon atoms either saturated $(C_{soot}\text{-}H)$ or radical/dehydrogenated $(C^{\bullet}_{soot})$. An important parameter to be considered is the number density of radical $(C^{\bullet}_{soot})$ sites, $\chi_{C^{\bullet}_{soot}}$ representing the possible available sites to proceed with acetylene addition. The active sites are created and destroyed faster than the typical velocities of fluid flow, so these reactions can be considered in a quasi-steady state regime leading to the following expression for the number density of radical sites:

$$\frac{d\left[C_{soot}^{\bullet}\right]}{dt}=0=k_{f1}\left[C_{soot}-H\right]\left[H\right]-k_{r1}\left[C_{soot}^{\bullet}\right]\left[H_2\right]$$
$$+k_{f2}\left[C_{soot}-H\right]\left[OH\right]-k_{r2}\left[C_{soot}^{\bullet}\right]\left[H_2O\right]$$
$$-k_{f3}\left[C_{soot}^{\bullet}\right]\left[H\right]-k_{f4}\left[C_{soot}^{\bullet}\right]\left[C_2H_2\right] \quad (B.32)$$
$$-k_{f5}\left[C_{soot}^{\bullet}\right]\left[O_2\right]$$

after a simple algebraic manipulation

$$\left[C_{soot}^{\bullet}\right]\times\left\{k_{r1}\left[H_2\right]+k_{r2}\left[H_2O\right]+k_{f3}\left[H\right]+k_{f4}\left[C_2H_2\right]+k_{f5}\left[O_2\right]\right\}$$
$$=\left[C_{soot}-H\right]\times\left\{k_{f1}\left[H\right]+k_{f2}\left[OH\right]\right\} \quad (B.33)$$

resolving por $\left[C_{soot}^{\bullet}\right]$

$$\left[C_{soot}^{\bullet}\right]=\frac{\left\{k_{f1}\left[H\right]+k_{f2}\left[OH\right]\right\}}{\left\{k_{r1}\left[H_2\right]+k_{r2}\left[H_2O\right]+k_{f3}\left[H\right]+k_{f4}\left[C_2H_2\right]+k_{f5}\left[O_2\right]\right\}}\times\left[C_{soot}-H\right] \quad (B.34)$$

so by analogy, we replace concentration of saturated and dehydrogenated carbon atoms by number density site for satured $\chi_{C_{soot}-H}$ and radical $\chi_{C_{soot}^{\bullet}}$, respectively. Changing, we have

$$\chi_{\left[C_{soot}^{\bullet}\right]}=\frac{\left\{k_{f1}\left[H\right]+k_{f2}\left[OH\right]\right\}}{\left\{k_{r1}\left[H_2\right]+k_{r2}\left[H_2O\right]+k_{f3}\left[H\right]+k_{f4}\left[C_2H_2\right]+k_{f5}\left[O_2\right]\right\}}\times\chi_{\left[C_{soot}-H\right]} \quad (B.35)$$

The number density of sites per particle surface $\left(\chi_{\left[C_{soot}-H\right]}\right)$ is considered constant and the value adopted has been taken from Appel et al (Appel, Bockhorn, and Frenklach 2000) and corresponds to 2.3×10^{15} (sites/cm^2). The concentration of saturated sites, $\left[C_{soot}-H\right]$(mole/cm^3), is calculated by

$$\left[\mathrm{C_{soot}-H}\right]=\frac{\chi_{C_{soot}-H}\times A_s}{A_v} \quad (B.36)$$

Where $\chi_{C_{soot}-H}$ is the number of sites per unit of soot surface area and is set to a constant value of $2.3\text{x}10^{15}$ sites/cm^2 (Appel, Bockhorn, and Frenklach 2000); A_s (cm^2/cm^3) is the surface density of soot particles. The HACA reaction scheme also uses an empirical (steric) parameter (α) to account for the fraction of surface sites available for a given reaction. Physically, it takes into account the probability of a gaseous species colliding with the prismatic (edge) planes instead of unreactive basal planes of particles and the fact that not all of the edge carbons are available for a given reaction. The rate of individual reactions (S4 for example) for a soot particle *i* can be calculated by the following equation:

$$R_{i,4} = 2C_{mass} \times k_4 \times [C_2H_2] \times \frac{\alpha \times \chi_{C_{soot}} \times A_{s,i} \times N_i}{A_v} \tag{B.37}$$

where k_4 is the pre-site rate coefficient, which is calculated based on Table B-1; $[C_2H_2]$ is the concentration of C_2H_2; $\chi_{C_{soot}}$ is the number of dehydrogenated sites $\left(C^{\cdot}_{soot}\right)$ per unit surface area; $A_{s,i}$ is the surface area of particle *i*; N_i is the number density of particle *i*. Assuming a steady state for $\left(C^{\cdot}_{soot}\right)$, $\chi_{C_{soot}}$ can be calculated using equation (B.35).

B.5 PAH-surface condensation

The PAH condensation model utilized in this study is based on transition and continuum regime collision theory between soot aggregates and pyrene (A_4), with a prescribed collision efficiency, $\gamma_{cond} = 0.5$ (Q. Zhang 2009). The condensation rate in (g/cm^3/s) is computed as:

$$R_{cond} = 2.2\gamma_{cond} M_c N_{c,A_4} \left[\frac{\pi k_B T}{2M_C N_{c,A4}}\right]^{1/2} N_S N_A \left(d_{soot} + d_{A_4}\right)^2 \tag{B.38}$$

B.6 Particle coagulation

Once soot particles are formed they collide with each other forming larger particles. Experimental studies observed that initially the particles look spherical and later acquire a fractal shape. Hence, particle coagulation is usually classified as coalescent growth and agglomeration into fractal aggregates.

The soot nucleation step also gives rise to the source term in the number density equation as outlined above. The decrease in particle number density is simply assumed to occur according to particle agglomeration which is modelled using the normal square dependence used by many other investigators e.g. Kent et al. (Kent and Wagner 1982). It is well known that this expression does not accurately represent the evolution of the soot number density throughout the flame (Leung, Lindstedt, and Jones 1991). However, it does provide a reasonable approximation of particle related properties.

Soot agglomeration is a process affecting the soot number density due to the collision of two soot particles (Lindstedt 1994).

$$R_{agg} = 2C_A \times \left(\rho N_s\right)^2 \times \sqrt{\frac{6k_B T}{\rho_s}} \times \left(\frac{6M_c}{\pi\rho_s}\right)^{1/6} \times \left(\rho Y_s\right)^{11/6} \left[C_S\right]^{1/6} \tag{B.39}$$

Where $\left[C_S\right]$ is the mole concentration of soot particle (mole/cm^3) and C_A is the agglomeration rate constant taken as equal to 1, meaning that every collision of two soot particles become agglomerated.

Bibliographie

Annmalai, K, and M Sibulkin. 1979. “Flame Spread over Combustible Surfaces for Laminar Flow Systems Part I: Excess Fuel and Heat Flux.” *Combustion Science and Technology* 19(5-6): 167–83.

Appel, J., H. Bockhorn, and M. Frenklach. 2000. “Kinetic Modeling of Soot Formation with Detailed Chemistry and Physics: Laminar Premixed Flames of C2 Hydrocarbons.” *Combustion and Flame* 121(1-2): 122–36.

Bai, X.S., M. Balthasar, F. Mauss, and L. Fuchs. 1998. “Detailed Soot Modeling in Turbulent Jet Diffusion Flames.” *Symposium (International) on Combustion* 27(1): 1623–30.

Balthasar, M. et al. 1996. “Flamelet Modeling of Soot Formation in Laminar Ethyne/air-Diffusion Flames.” *Symposium (International) on Combustion* 26(2): 2369–77.

Balthasar, M., and M. Kraft. 2003. “A Stochastic Approach to Calculate the Particle Size Distribution Function of Soot Particles in Laminar Premixed Flames.” *Combustion and Flame* 133(3): 289–98.

Baukal Jr., C.E. 1998. *Oxygen-Enhanced Combustion*. Boca Raton, FL: CRC Press.

Beltrame, A et al. 2001. “Soot and NO Formation in Methane–oxygen Enriched Diffusion Flames.” *Combustion and Flame* 124(1-2): 295–310.

Bennett, B.A.V., Z. Cheng, R.W. Pitz, and M.D. Smooke. 2008. “Computational and Experimental Study of Oxygen-Enhanced Axisymmetric Laminar Methane Flames.” *Combustion Theory and Modelling* 12(3): 497–527.

Bento, D., K. Thomson, and O. Gülder. 2006. “Soot Formation and Temperature Field Structure in Laminar Propane–air Diffusion Flames at Elevated Pressures.” *Combustion and Flame* 145(4): 765–78.

Bhattacharjee, S., and R. A. Altenkirch. 1991. “Radiation-Controlled, Opposed-Flow Flame Spread in a Microgravity Environment.” *Symposium (International) on Combustion* 23(1): 1627–33.

Brahmi, L. et al. 2005. “Microgravity Laminar Diffusion Flame in a Perpendicular Fuel and Oxidizer Stream Configuration.” *AIAA journal* 43(8): 1725–33.

Centeno, Felipe Roman, Rogério Brittes, Francis. H.R. França, and Ofodike A. Ezekoye. 2015. “Evaluation of Gas Radiation Heat Transfer in a 2D Axisymmetric Geometry Using the Line-by-Line Integration and WSGG Models.” *Journal of Quantitative Spectroscopy and Radiative Transfer* 156: 1–11.

Chao, B.H., C.K. Law, and J.S. T’ien. 1991. “Structure and Extinction of Diffusion Flames with Flame Radiation.” *Symposium (International) on Combustion* 23(1): 523–31.

Chernov, V., Q. Zhang, M.J. Thomson, and S.B. Dworkin. 2012. “Numerical Investigation of Soot Formation Mechanisms in Partially-Premixed Ethylene–air Co-Flow Flames.” *Combustion and Flame* 159(9): 2789–98.

Chu, Huaqiang, Fengshan Liu, and Huaichun Zhou. 2011. “Calculations of Gas Thermal Radiation Transfer in One-Dimensional Planar Enclosure Using LBL and SNB Models.”

International Journal of Heat and Mass Transfer 54(21-22): 4736–45.

Chung, S.H., and C.K. Law. 1983. "Structure and Extinction of Convective Diffusion Flames with General Lewis Numbers." *Combustion and Flame* 52: 59–79.

Chung, Suk Ho, and Chung King Law. 1986. "An Experimental Study of Droplet Extinction in the Absence of External Convection." *Combustion and Flame* 64(2): 237–41.

Coelho, P J, P Perez, and M El Hafi. 2003. "Benchmark Numerical Solutions for Radiative Heat Transfer in Two-Dimensional Axisymmetric Enclosures with Nongray Sooting Media." *Numerical Heat Transfer, Part B: Fundamentals* 43(5): 425–44.

Consalvi, J.L., and F. Liu. 2014a. "Radiative Heat Transfer in the Core of Axisymmetric Pool Fires – I: Evaluation of Approximate Radiative Property Models." *International Journal of Thermal Sciences* 84(0): 104–17.

———. 2014b. "Radiative Heat Transfer Through the Fuel-Rich Core of Laboratory-Scale Pool Fires." *Combustion Science and Technology* 186(4-5): 475–89.

Dalzell, W.H., and A.F. Sarofim. 1969. "Optical Constants of Soot and Their Application to Heat-Flux Calculations." *Journal of Heat Transfer* 91(1): 100–104.

Dasch, C.J. 1992. "One-Dimensional Tomography: A Comparison of Abel, Onion-Peeling, and Filtered Backprojection Methods." *Applied Optics* 31(8): 1146–52.

Daun, K.J., K.A. Thomson, F. Liu, and G.J. Smallwood. 2006. "Deconvolution of Axisymmetric Flame Properties Using Tikhonov Regularization." *Applied Optics* 45(19): 4638–46.

Demarco, R., J.L. Consalvi, A. Fuentes, and S. Melis. 2011. "Assessment of Radiative Property Models in Non-Gray Sooting Media." *International Journal of Thermal Sciences* 50(9): 1672–84.

Demarco, R., F. Nmira, and J.L. Consalvi. 2013. "Influence of Thermal Radiation on Soot Production in Laminar Axisymmetric Diffusion Flames." *Journal of Quantitative Spectroscopy and Radiative Transfer* 120: 52–69.

Denison, M. K., and B. W. Webb. 1993a. "A Spectral Line-Based Weighted-Sum-of-Gray-Gases Model for Arbitrary RTE Solvers." *Journal of Heat Transfer* 115(4): 1004–12.

———. 1993b. "An Absorption-Line Blackbody Distribution Function for Efficient Calculation of Total Gas Radiative Transfer." *Journal of Quantitative Spectroscopy and Radiative Transfer* 50(5): 499–510.

———. 1995a. "Development and Application of an Absorptionline Blackbody Distribution Function for CO2." *International Journal of Heat and Mass Transfer* 38(10): 1813–21.

———. 1995b. "The Absorption-Line Blackbody Distribution Function at Elevated Pressure." *ICHMT DIGITAL LIBRARY ONLINE* 7.

———. 1995c. "The Spectral Line-Based Weighted-Sum-of-Gray-Gases Model in Nonisothermal Nonhomogeneous Media." *Journal of Heat Transfer* 117(2): 359–65.

———. 1995d. "The Spectral-Line Weighted-Sum-of-Gray-Gases Model for H2O/CO2 Mixtures." *Journal of Heat Transfer* 117(3): 788–92.

Domoto, G.A. 1974. “Frequency Integration for Radiative Transfer Problems Involving Homogeneous Non-Gray Gases: The Inverse Transmission Function.” *Journal of Quantitative Spectroscopy and Radiative Transfer* 14(9): 935–42.

Du, D.X., R.L. Axelbaum, and C.K. Law. 1991. “The Influence of Carbon Dioxide and Oxygen as Additives on Soot Formation in Diffusion Flames.” *Symposium (International) on Combustion* 23(1): 1501–7.

Du, J. 1995. “The Effect of Flame Structure on Soot-Particle Inception in Diffusion Flames,.” *Combustion and Flame* 100(3): 367–75.

Dworkin, S.B. et al. 2011. “Application of an Enhanced PAH Growth Model to Soot Formation in a Laminar Coflow Ethylene/air Diffusion Flame.” *Combustion and Flame* 158(9): 1682–95.

Emmons, H.W. 1956. “The Film Combustion of Liquid Fuel.” *ZAMM Journal of Applied Mathematics and Mechanics/Zeitschrift für Angewandte Mathematik und Mechanik* 36(12): 60–71.

Faeth, G.M. 2001. “Laminar and Turbulent Gaseous Diffiusion Flames.” In *Microgravity Combustion: Fire in Free Fall*, ed. H. Ross. Academic Press, 83–182.

Fenimore, Charles P, and George Wallace Jones. 1967. “Oxidation of Soot by Hydroxyl Radicals.” *The Journal of Physical Chemistry* 71(3): 593–97.

Fiveland, W.A. 1984. “Discrete-Ordinates Solutions of the Radiative Transport Equation for Rectangular Enclosures.” *Journal of Heat Transfer* 106(4): 699–706.

Frenklach, M, and H Wang. 1994. “Detailed Mechanism and Modeling of Soot Particle Formation.” In *Soot Formation in Combustion SE - 10*, Springer Series in Chemical Physics, ed. Henning Bockhorn. Springer Berlin Heidelberg, 165–92.

Frenklach, M., D. W. Clary, W. C. Gardiner, and S. E. Stein. 1988. “Effect of Fuel Structure on Pathways to Soot.” *Symposium (International) on Combustion* 21(1): 1067–76.

Frenklach, M., and H. Wang. 1991. “Detailed Modeling of Soot Particle Nucleation and Growth.” *Symposium (International) on Combustion* 23(1): 1559–66.

Frenklach, Michael. 2002. “Reaction Mechanism of Soot Formation in Flames.” *Physical Chemistry Chemical Physics* 4(11): 2028–37.

Frenklach, Michael, and Stephen J. Harris. 1987. “Aerosol Dynamics Modeling Using the Method of Moments.” *Journal of Colloid and Interface Science* 118(1): 252–61.

Fuentes, A. et al. 2005. “Evaluation of the Extinction Factor in a Laminar Flame Established over a PMMA Plate in Microgravity.” *Microgravity - Science and Technology* 17(3): 10–14.

———. 2006. “Interaction Entre La Zone Réactionnelle et Le Champ de Concentration Des Suies (cas de La Flamme de Diffusion Laminaire Ausein D’une Couche Limite).” Université de Poitiers.

Fuentes, A., G. Legros, A. Claverie, et al. 2007. “Interactions between Soot and CH Radicals in a Laminar Boundary Layer Type Diffusion Flame in Microgravity.” *Proceedings of the Combustion Institute* 31(2): 2685–92.

Fuentes, A., G. Legros, H. El-Rabii, et al. 2007. “Laser-Induced Incandescence Calibration in a Three-Dimensional Laminar Diffusion Flame.” *Experiments in Fluids* 43(6): 939–48.

Fuentes, A., S. Rouvreau, et al. 2007. “Sooting Behavior Dynamics of a Non-Buoyant Laminar Diffusion Flame.” *Combustion Science and Technology* 179(1-2): 3–19.

Fuentes, A. et al. 2013. “Experimental and Numerical Study of the Effects of the Oxygen Index on the Radiation Characteristics of Laminar Coflow Diffusion Flames.” *Combustion and Flame* 160(4): 786–95.

Glassman, I., and P. Yaccarino. 1980. “The Effect of Oxygen Concentration on Sooting Diffusion Flames.” *Combustion Science and Technology* 24(3-4): 107–14.

Goutiere, V., F. Liu, and A. Charette. 2000. “An Assessment of Real-Gas Modelling in 2D Enclosures.” *Journal of Quantitative Spectroscopy and Radiative Transfer* 64(3): 299–326.

Greenberg, P. S., and J. C. Ku. 1997. “Soot Volume Fraction Maps for Normal and Reduced Gravity Laminar Acetylene Jet Diffusion Flames.” *Combustion and Flame* 108(1-2): 227–30.

Guo, H., F. Liu, and G. J. Smallwood. 2004. “Soot and NO Formation in Counterflow Ethylene/oxygen/nitrogen Diffusion Flames.” *Combustion Theory and Modelling* 8(3): 475–89.

Guo, H., F. Liu, G. J. Smallwood, and Ö. L. Gülder. 2006. “Numerical Study on the Influence of Hydrogen Addition on Soot Formation in a Laminar Ethylene–air Diffusion Flame.” *Combustion and Flame* 145(1-2): 324–38.

Harris, S.J., and I.M. Kennedy. 1988. “The Coagulation of Soot Particles with Van Der Waals Forces.” *Combustion Science and Technology* 59(4-6): 443–54.

Haynes, B. S., and H. Gg. Wagner. 1982. “The Surface Growth Phenomenon in Soot Formation.” *Zeitschrift für Physikalische Chemie* 133: 201–13.

Hottel, H. C., and A. F. Sarofim. 1967. *Radiative Transfer*. New York: McGraw-Hill Book Company.

Hwang, J.Y ., and S. H. Chung. 2001. “Growth of Soot Particles in Counterflow Diffusion Flames of Ethylene.” *Combustion and Flame* 125(1-2): 752–62.

Ju, Y., H. Guo, K. Maruta, and F. Liu. 1997. “On the Extinction Limit and Flammability Limit of Non-Adiabatic Stretched Methane–air Premixed Flames.” *Journal of fluid mechanics* 342: 315–34.

Kee, R. J. et al. 1986. “A FORTRAN Computer Code Package for the Evaluation of Gas-Phase Multicomponent Transport Properties.” *Sandia report* SAND86-824(December): 3–39.

Kee, R. J., M. E. Coltrin, and P. Glarborg. 2003. *Chemically Reacting Flow: Theory and Practice*. Hoboken, New Jersey: John Wiley & Sons, Inc.

Kee, R. J., F. M. Rupley, E. Meeks, and J. A. Miller. 1996. Work *Chemkin-III: A Fortran Chemical Kinetics Package for the Analysis of Gas- Phase Chemical and Plasma Kinetics*.

Kennedy, I. M. 1987. “The Evolution of a Soot Aerosol in a Counterflow Diffusion Flame.” *Combustion and Flame* 68(1): 1–16.

Kent, J. H. 1986. “A Quantitative Relationship between Soot Yield and Smoke Point Measurements.” *Combustion and Flame* 63(3): 349–58.

Kent, J. H., and H. Gg. Wagner. 1982. “Soot Measurements in Laminar Ethylene Diffusion Flames.” *Combustion and Flame* 47: 53–65.

Kim, C. H., A. M. El-Leathy, F. Xu, and G. M. Faeth. 2004. “Soot Surface Growth and Oxidation in Laminar Diffusion Flames at Pressures of 0.1–1.0 Atm.” *Combustion and Flame* 136(1-2): 191–207.

Konsur, B., C. M. Megaridis, and D. W. Griffin. 1999a. “Fuel Preheat Effects on Soot-Field Structure in Laminar Gas Jet Diffusion Flames Burning in 0-G and 1-G.” *Combustion and Flame* 116(3): 334–47.

———. 1999b. “Soot Aerosol Properties in Laminar Soot-Emitting Microgravity Nonpremixed Flames.” *Combustion and Flame* 118(4): 509–20. http://www.sciencedirect.com/science/article/pii/S0010218099000218 (May 20, 2015).

Kosdon, F. J., F. A. Williams, and C. Buman. 1969. “Combustion of Vertical Cellulosic Cylinders in Air.” *Symposium (International) on Combustion* 12(1): 253–64.

Kounalakis, M. E., J. P. Gore, and G. M. Faeth. 1989a. “Mean and Fluctuating Radiation Properties of Nonpremixed Turbulent Carbon Monoxide/air Flames.” *Journal of Heat Transfer* 111(4): 1021–30.

———. 1989b. “Turbulence/radiation Interactions in Nonpremixed Hydrogen/air Flames.” *Symposium (International) on Combustion* 22(1): 1281–90.

Krishnamurthy, L., F. A. Williams, and K. Seshadri. 1976. “Asymptotic Theory of Diffusion-Flame Extinction in the Stagnation-Point Boundary Layer.” *Combustion and Flame* 26: 363–77.

Kuo, K. K. 1986. *Principles of Combustion*. Wiley.

Lahaye, J., and G. Prado. 1981. “Morphology and Internal Structure of Soot and Carbon Blacks.” In *Particulate Carbon SE - 2*, eds. DonaldC. Siegla and GeorgeW. Smith. Springer US, 33–55.

Lautenberger, C. W. et al. 2005. “A Simplified Model for Soot Formation and Oxidation in CFD Simulation of Non-Premixed Hydrocarbon Flames.” *Fire Safety Journal* 40(2): 141–76.

Law, C. K. 1975. “Asymptotic Theory for Ignition and Extinction in Droplet Burning.” *Combustion and Flame* 24: 89–98.

Lee, K. -O. et al. 2000. “Soot Formation Effects of Oxygen Concentration in the Oxidizer Stream of Laminar Coannular Nonpremixed Methane/air Flames.” *Combustion and Flame* 121(1-2): 323–33.

Legros, G. et al. 2005. “Three-Dimensional Recomposition of the Absorption Field inside a Nonbuoyant Sooting Flame.” *Optics letters* 30(24): 3311–13.

———. 2006. “Soot Volume Fraction Measurements in a Three-Dimensional Laminar

Diffusion Flame Established in Microgravity." *Combustion Science and Technology* 178(5): 813–35.

———. 2009. "Transport Mechanisms Controlling Soot Production inside a Non-Buoyant Laminar Diffusion Flame." *Proceedings of the Combustion Institute* 32(2): 2461–70.

Legros, G., and J. L. Torero. 2015. "Phenomenological Model of Soot Production inside a Non-Buoyant Laminar Diffusion Flame." *Proceedings of the Combustion Institute* 35(3): 2545–53.

Leung, K. M., R. P. Lindstedt, and W. P. Jones. 1991. "A Simplified Reaction Mechanism for Soot Formation in Nonpremixed Flames." *Combustion and Flame* 87(3-4): 289–305.

Leusden, C. Pels, and N. Peters. 2000. "Experimental and Numerical Analysis of the Influence of Oxygen on Soot Formation in Laminar Counterflow Flames of Acetylene." *Proceedings of the Combustion Institute* 28(2): 2619–25.

Liñán, A. 1974. "The Asymptotic Structure of Counterflow Diffusion Flames for Large Activation Energies." *Acta Astronautica* 1(7-8): 1007–39.

Lindstedt, P. R. 1994. "Simplified Soot Nucleation and Surface Growth Steps for Non-Premixed Flames." In *Soot Formation in Combustion SE - 27*, Springer Series in Chemical Physics, ed. Henning Bockhorn. Springer Berlin Heidelberg, 417–41.

Liu, F., Ö. L. Gülder, G. J. Smallwood, and Y. Ju. 1998. "Non-Grey Gas Radiative Transfer Analyses Using the Statistical Narrow-Band Model." *International Journal of Heat and Mass Transfer* 41(14): 2227–36.

Liu, F., H. Guo, and G. J. Smallwood. 2004. "Effects of Radiation Model on the Modeling of a Laminar Coflow Methane/air Diffusion Flame." *Combustion and Flame* 138(1-2): 136–54.

Liu, F., H. Guo, G. J. Smallwood, and Ö. L. Gülder. 2003. "Numerical Modelling of Soot Formation and Oxidation in Laminar Coflow Non-Smoking and Smoking Ethylene Diffusion Flames." *Combustion Theory and Modelling* 7(2): 301–15.

Liu, F., H. Guo, G. J. Smallwood, and M. El Hafi. 2004. "Effects of Gas and Soot Radiation on Soot Formation in Counterflow Ethylene Diffusion Flames." *Journal of Quantitative Spectroscopy and Radiative Transfer* 84(4): 501–11.

Liu, F., G. J. Smallwood, and Ö. L. Gulder. 2000. "Band Lumping Strategy for Radiation Heat Transfer Calculations Using a Narrowband Model." *Journal of Thermophysics and Heat Transfer* 14(2): 278–81.

Liu, F., G. J. Smallwood, and Ö. L. Gülder. 2000. "Application of the Statistical Narrow-Band Correlated-K Method to Low-Resolution Spectral Intensity and Radiative Heat Transfer Calculations — Effects of the Quadrature Scheme." *International Journal of Heat and Mass Transfer* 43(17): 3119–35.

Liu, F., G. J. Smallwood, and W. Kong. 2011. "The Importance of Thermal Radiation Transfer in Laminar Diffusion Flames at Normal and Microgravity." *Journal of Quantitative Spectroscopy and Radiative Transfer* 112(7): 1241–49.

Liu, F., K. A. Thomson, H. Guo, and G. J. Smallwood. 2006. "Numerical and Experimental

Study of an Axisymmetric Coflow Laminar Methane–air Diffusion Flame at Pressures between 5 and 40 Atmospheres." *Combustion and Flame* 146(3): 456–71.

Maas, U., and S. B. Pope. 1992. "Simplifying Chemical Kinetics: Intrinsic Low-Dimensional Manifolds in Composition Space." *Combustion and Flame* 88(3-4): 239–64.

Markstein, G. H., and J. De Ris. 1985. "Radiant Emission and Absorption by Laminar Ethylene and Propylene Diffusion Flames." *Symposium (International) on Combustion* 20(1): 1637–46.

Mcenally, C. S. et al. 2000. "Characterization of a Coflowing Methane/air Non-Premixed Flame with Computer Modeling, Rayleigh-Raman Imaging, and on-Line Mass Spectrometry." *Proceedings of the Combustion Institute* 28(2): 2063–70.

McEnally, C. S., L. D. Pfefferle, B. Atakan, and K. Kohse-Höinghaus. 2006. "Studies of Aromatic Hydrocarbon Formation Mechanisms in Flames: Progress towards Closing the Fuel Gap." *Progress in Energy and Combustion Science* 32(3): 247–94.

Megaridis, C. M., and R. Dobbins. 1989a. "Comparison of Soot Growth and Oxidation in Smoking and Non–smoking Ethylene Diffusion Flames." *Combustion Science and Technology* 66(1-3): 1–16.

———. 1989b. "Soot Aerosol Dynamics in a Laminar Ethylene Diffusion Flame." *Symposium (International) on Combustion* 22(1): 353–62.

Megaridis, C. M., D. W. Griffin, and B. Konsur. 1996. "Soot-Field Structure in Laminar Soot-Emitting Microgravity Nonpremixed Flames." *Symposium (International) on Combustion* 26(1): 1291–99.

Mehta, R. S., D. C. Haworth, and M. F. Modest. 2009. "An Assessment of Gas-Phase Reaction Mechanisms and Soot Models for Laminar Atmospheric-Pressure Ethylene–air Flames." *Proceedings of the Combustion Institute* 32(1): 1327–34.

Miller, J. A., M. J. Pilling, and J. Troe. 2005. "Unravelling Combustion Mechanisms through a Quantitative Understanding of Elementary Reactions." *Proceedings of the Combustion Institute* 30(1): 43–88. http://www.sciencedirect.com/science/article/pii/S0082078404003315 (June 19, 2015).

Modest, M. F. 2013. Radiative Heat Transfer *Radiative Heat Transfer*. San Diego: Academic press.

Modest, M. F., and R. J. Riazzi. 2005. "Assembly of Full-Spectrum K-Distributions from a Narrow-Band Database; Effects of Mixing Gases, Gases and Nongray Absorbing Particles, and Mixtures with Nongray Scatterers in Nongray Enclosures." *Journal of Quantitative Spectroscopy and Radiative Transfer* 90(2): 169–89.

Modest, M. F., and H. Zhang. 2001. "The Full-Spectrum Correlated-K Distribution for Thermal Radiation From Molecular Gas-Particulate Mixtures." *Journal of Heat Transfer* 124(1): 30–38.

Moss, J. B. 1995. "Laminar Flames." In *Combustion Fundamentals of Fire*, ed. Cox. G. San Diego: Academic Press, 221.

Mueller, M. E., G. Blanquart, and H. Pitsch. 2009. "Hybrid Method of Moments for Modeling Soot Formation and Growth." *Combustion and Flame* 156(6): 1143–55.

Pagni, P.J., and T.M. Shih. 1977. “Excess Pyrolyzate.” *Symposium (International) on Combustion* 16(1): 1329–43.

Park, S.H. et al. 2005. “An Aerosol Model to Predict Size and Structure of Soot Particles.” *Combustion Theory and Modelling* 9(3): 499–513.

Patankar, S. 1980. *Numerical Heat Transfer and Fluid Flow*. Taylor & Francis.

Raithby, G D, and E H Chui. 1990. “A Finite-Volume Method for Predicting a Radiant Heat Transfer in Enclosures With Participating Media.” *Journal of Heat Transfer* 112(2): 415–23.

Richter, H, and J.B Howard. 2000. “Formation of Polycyclic Aromatic Hydrocarbons and Their Growth to Soot—a Review of Chemical Reaction Pathways.” *Progress in Energy and Combustion Science* 26(4-6): 565–608.

De Ris, John L., Peter K. Wu, and G. Heskestad. 2000. “Radiation Fire Modeling.” *Proceedings of the Combustion Institute* 28(2): 2751–59.

Rivière, Philippe, and Anouar Soufiani. 2012. “Updated Band Model Parameters for H2O, CO2, CH4 and CO Radiation at High Temperature.” *International Journal of Heat and Mass Transfer* 55(13-14): 3349–58.

Roper, F.G. 1977. “The Prediction of Laminar Jet Diffusion Flame Sizes: Part I. Theoretical Model.” *Combustion and Flame* 29: 219–26.

Rothman, L.S. et al. 2010. “HITEMP, the High-Temperature Molecular Spectroscopic Database.” *Journal of Quantitative Spectroscopy and Radiative Transfer* 111(15): 2139–50.

Rouvreau, S. et al. 2002. “Numerical Evaluation of Boundary-Layer Assumptions Used for the Prediction of the Standoff Distance of a Laminar Diffusion Flame.” *Proceedings of the Combustion Institute* 29(2): 2527–34.

Rouvreau, S., P. Cordeiro, J. L. Torero, and P. Joulain. 2005. “Influence of G-Jitter on a Laminar Boundary Layer Type Diffusion Flame.” *Proceedings of the Combustion Institute* 30(1): 519–26.

Santa, K et al. 2007. “Radiative Extinction of Gaseous Spherical Diffusion Flames in Microgravity.” *Combustion and Flame* 151(4): 665–75.

Santoro, R. J., and C. R. Shaddix. 2002. “Laser-Induced Incandescence.” *Applied combustion diagnostics*: 252–86.

Santoro, R. J., T. T. Yeh, J. J. Horvath, and H. G. Semerjian. 1987. “The Transport and Growth of Soot Particles in Laminar Diffusion Flames.” *Combustion Science and Technology* 53(2-3): 89–115.

Sazhin, S. S., E. M. Sazhina, O. Faltsi-Saravelou, and P. Wild. 1996. “The P-1 Model for Thermal Radiation Transfer: Advantages and Limitations.” *Fuel* 75(3): 289–94.

Schuetz, C.A., and M. Frenklach. 2002. “Nucleation of Soot: Molecular Dynamics Simulations of Pyrene Dimerization.” *Proceedings of the Combustion Institute* 29(2): 2307–14.

Shaddix, Christopher R. et al. 2011. *Predicting the Effects of Fuel Composition and Flame Structure on Soot Generation in Turbulent Non-Premixed Flames*.

Shaddix, Christopher R., and Kermit C. Smyth. 1996. "Laser-Induced Incandescence Measurements of Soot Production in Steady and Flickering Methane, Propane, and Ethylene Diffusion Flames." *Combustion and Flame* 107(4): 418–52.

Sivathanu, Y R, J P Gore, and J Dolinar. 1991. "Transient Scalar Properties of Strongly Radiating Jet Flames." *Combustion Science and Technology* 76(1-3): 45–66.

Slavinskaya, N.A., and P. Frank. 2009. "A Modelling Study of Aromatic Soot Precursors Formation in Laminar Methane and Ethene Flames." *Combustion and Flame* 156(9): 1705–22.

Smooke, M.D., R.E. Mitchell, and D.E. Keyes. 1986. "Numerical Solution of Two-Dimensional Axisymmetric Laminar Diffusion Flames." *Combustion Science and Technology* 67(4-6): 85–122.

Sohrab, S. H., A. Liñán, and F. A. Williams. 1982. "Asymptotic Theory of Diffusion-Flame Extinction with Radiant Loss from the Flame Zone." *Combustion Science and Technology* 27(3-4): 143–54.

Sohrab, S. H., and F. A. Williams. 1981. "Extinction of Diffusion Flames Adjacent to Flat Surfaces of Burning Polymers." *Journal of Polymer Science: Polymer Chemistry Edition* 19(11): 2955–76.

Solovjov, V. P., and B. W. Webb. 2000a. "An Efficient Method for Modeling Radiative Transfer in Multicomponent Gas Mixtures with Soot." *Journal of Heat Transfer* 123(3): 450–57.

———. 2000b. "SLW Modeling of Radiative Transfer in Multicomponent Gas Mixtures." *Journal of Quantitative Spectroscopy and Radiative Transfer* 65(4): 655–72.

Soufiani, A., and J. Taine. 1997. "High Temperature Gas Radiative Property Parameters of Statistical Narrow-Band Model for H2O, CO2 and CO, and Correlated-K Model for H2O and CO2." *International Journal of Heat and Mass Transfer* 40(4): 987–91.

T'ien, James S., and David W. Foutch. 1987. "Extinction of a Stagnation-Point Diffusion Flame at Reduced Gravity." *AIAA Journal* 25(7): 972–76.

Taine, Jean, and Anouar Soufiani. 1999. 33 Advances in Heat Transfer *Advances in Heat Transfer Volume 33*. Elsevier.

Talbot, L, R K Cheng, R W Schefer, and D R Willis. 1980. "Thermophoresis of Particles in a Heated Boundary Layer." *Journal of Fluid Mechanics* 101(04): 737–58.

Tashkun, S.A. et al. 2003. "CDSD-1000, the High-Temperature Carbon Dioxide Spectroscopic Databank." *Journal of Quantitative Spectroscopy and Radiative Transfer* 82(1-4): 165–96.

Thurgood, C P, A Pollard, and H A Becker. 1995. "The TN Quadrature Set for the Discrete Ordinates Method." *Journal of Heat Transfer* 117(4): 1068–70.

Torero, J. L. 2000. *Material Properties That Control Ignition and Spread of a Fire in Micro-Gravity Environments. ASME Heat Transfer Conference*. ASME-NHTC-2000-12314.

Torero, J. L., T. Vietoris, G. Legros, and P. Joulain. 2002. "Estimation of a Total Mass Transfer Number from the Standoff Distance of a Spreading Flame." *Combustion Science and Technology* 174(11-12): 187–203.

Urban, D. L. et al. 2000. "Smoke-Point Properties of Non-Buoyant Round Laminar Jet Diffusion Flames." *Proceedings of the Combustion Institute* 28(2): 1965–72. http://www.sciencedirect.com/science/article/pii/S0082078400806025 (May 20, 2015).

Vandsburger, U., I. Kennedy, and I. Glassman. 1984. "Sooting Counterflow Diffusion Flames with Varying Oxygen Index." *Combustion Science and Technology* 39(1-6): 263–85.

Vietoris, T. et al. 2000. "Laminar Diffusion Flame in Microgravity: The Results of the Minitexus 6 Sounding Rocket Experiment." *Proceedings of the Combustion Institute* 28(2): 2883–89.

Vander Wal, R. L., K. A. Jensen, and M. Y. Choi. 1997. "Simultaneous Laser-Induced Emission of Soot and Polycyclic Aromatic Hydrocarbons within a Gas-Jet Diffusion Flame." *Combustion and Flame* 109(3): 399–414. http://www.sciencedirect.com/science/article/pii/S0010218096001897 (June 19, 2015).

Walsh, K.T., M.B. Long, M.A. Tanoff, and M.D. Smooke. 1998. "Experimental and Computational Study of CH, CH*, and OH* in an Axisymmetric Laminar Diffusion Flame." *Symposium (International) on Combustion* 27(1): 615–23.

Wang, H., and M. Frenklach. 1997. "A Detailed Kinetic Modeling Study of Aromatics Formation in Laminar Premixed Acetylene and Ethylene Flames." *Combustion and Flame* 110(1-2): 173–221.

Wang, L. et al. 2002. "A Study of the Influence of Oxygen Index on Soot, Radiation, and Emission Characteristics of Turbulent Jet Flames." *Combustion Science and Technology* 174(8): 45–72. http://dx.doi.org/10.1080/00102200290021245.

Wang, L., and M. F. Modest. 2005. "Narrow-Band Based Multiscale Full-Spectrum K-Distribution Method for Radiative Transfer in Inhomogeneous Gas Mixtures." *Journal of heat transfer* 127(7): 740–48.

Wang, Q., and B. H. Chao. 2011. "Kinetic and Radiative Extinctions of Spherical Burner-Stabilized Diffusion Flames." *Combustion and Flame* 158(8): 1532–41.

Williams, F. A. 1981. "A Review of Flame Extinction." *Fire Safety Journal* 3(3): 163–75.

Xu, F., Z. Dai, and G. M. Faeth. 2002. "Flame and Soot Boundaries of Laminar Jet Diffusion Flames." *AIAA Journal* 40(12): 2439–46.

Zelepouga, S. A., A. V. Saveliev, L. A. Kennedy, and A. A. Fridman. 2000. "Relative Effect of Acetylene and PAHs Addition on Soot Formation in Laminar Diffusion Flames of Methane with Oxygen and Oxygen-Enriched Air." *Combustion and Flame* 122(1-2): 76–89.

Zhang, L., A. Soufiani, and J. Taine. 1988. "Spectral Correlated and Non-Correlated Radiative Transfer in a Finite Axisymmetric System Containing an Absorbing and Emitting Real Gasparticle Mixture." *International Journal of Heat and Mass Transfer* 31(11): 2261–72.

Zhang, Q. et al. 2009. "A Numerical Study of Soot Aggregate Formation in a Laminar Coflow

Diffusion Flame." *Combustion and Flame* 156(3): 697–705.

———. 2009. "Detailed Modeling of Soot Formation/oxidation in Laminar Co-Flow Diffusion Flames." University of Toronto.